Spring 4-12-2018

Development of a Positron-Emitting Surrogate Microsphere for Image-Based Dosimetry in Yttrium-90 Radioembolization Therapy

Gregory D. Chambers

Gregory D. Chambers
Candidate

Nuclear Engineering
Department

This dissertation is approved, and it is acceptable in quality and form for publication:

Approved by the Dissertation Committee:

Reed Selwyn, Chairperson

Joanna Fair

Adam Hecht

Gary Cooper

DEVELOPMENT OF A POSITRON-EMITTING SURROGATE MICROSPHERE FOR IMAGE-BASED DOSIMETRY IN YTTRIUM-90 RADIOEMBOLIZATION THERAPY

by

GREGORY D. CHAMBERS

B.S., Nuclear Engineering, University of New Mexico, 1994
M.S., Nuclear Engineering, University of New Mexico, 2002

DISSERTATION

Submitted in Partial Fulfillment of the
Requirements for the Degree of

Doctor of Philosophy
Engineering

The University of New Mexico
Albuquerque, New Mexico

May 2018

DEDICATION

I would like to dedicate this work to Jennifer, Everett and Eleanor.

I could not have done this without them.

ACKNOWLEGEMENTS

I would like to thank my dissertation committee. Reed Selwyn, Joanna Fair, Adam Hecht and Gary Cooper. I appreciate the time and effort they have spent.

I would also like to send out a prayer for Philip Heintz. I wish he were here to see the completion of this project. I was very lucky to have known him and I am going to miss seeing him around.

I would also like to acknowledge the hard work put forth by my advisor Reed Selwyn. This project would not have gotten off the ground if he had not found a way to send time and resources to the project. He has been an excellent mentor. I know it has not been easy and I am grateful.

I would like to acknowledge Gary Cooper and Betty Jo Switz. They helped me out is so many ways, I don't even know where to start. Thank you Gary and Betty Jo.

I would like to thank my colleagues. Daniel Sandoval helped remind me that I was not the only one losing my mind. I would like to thank Rebecca Lamoureux and Trey Slauter for easing my workload to help me complete this project. I also really appreciate Colin Wilson for his assistance with the rat images. Kim and Mike Paffet were very helpful with the microscopy. Vicki White helped write the animal protocol and navigate Topaz.

I would like to thank Jeff Norenberg for letting me use his lab facilities. I would also like to thank the folks at the lab, Chelsea, Q, Monique and Tamara. Monique managed to keep the PET scanner going long enough to get rat images. I would especially like to thank Tamara Anderson Daniels. She is always looking on the bright side.

I would like to acknowledge my Mom and Dad, Sherry and Ron Kruzie Sr. They are the best parents a person could wish for.

I count myself very fortunate to have had so many friends and family that have been supportive through the years.

DEVELOPMENT OF A POSITRON-EMITTING SURROGATE MICROSPHERE FOR IMAGE-BASED DOSIMETRY IN YTTRIUM-90 RADIOEMBOLIZATION THERAPY

Gregory D. Chambers

B.S., Nuclear Engineering, University of New Mexico, 1994

M.S., Nuclear Engineering, University of New Mexico, 2002

Ph.D., Engineering, University of New Mexico, 2018

ABSTRACT

Radioembolization of liver tumors using yttrium-90 (Y-90) labeled microspheres is a proven method of treatment. The primary decay mode of Y-90 is beta-minus decay. The electrons produced during decay deliver a cytotoxic radiation dose in a localized volume. The radiation dose is sufficient to kill tumor cells yet spare the normal liver. The Y-90 microspheres are delivered via a catheter that has been placed in an artery that supplies blood to the tumor. Microspheres are injected and the blood distributes the microspheres. The current practice involves two separate procedures. The first procedure is an assessment of the vasculature of the liver and tumor. This assessment is performed with radiolabeled macro-aggregated albumin particles (Tc-99m MAA). The Tc-99m MAA is injected via a catheter placed in the same location that will be used for the delivery of Y-90 microspheres. The distribution of the Tc-99m MAA particles is imaged using a gamma camera. This data is used to predict the microsphere distribution and subsequent dose to the tumor, normal liver, lungs and other organs. The data may be used to adjust the Y-90 activity and to perform crude pre-treatment dosimetry. Accurate pre-treatment dosimetry is largely absent.

This study was performed to create a positron-emitting surrogate microsphere that was close in size and shape to the Y-90 microspheres. Positron emission tomography (PET) is superior to SPECT for activity quantification. Fluorine-18 (F-18) was chosen for initial experiments. There were two aims of the research:

Aim 1: To develop surrogate PET microsphere. This included radiolabeling, stability testing in vitro and stability testing in an animal.

Aim 2: To develop a computational technique to perform dosimetry with the surrogate microsphere. PET images of the surrogate radionuclide were imported into a Monte Carlo program. PET images were used to simulate the distribution of the Y-90 microspheres. The output of the simulation was a tomographic map of absorbed dose from the Y-90. Validation of the image-based dosimetry was performed by measuring known amounts of F-18 and Y-90 in a phantom. The measured dose within the phantom was compared to the dose predicted with the Monte Carlo simulation.

Table of Contents

List of Figures

I. Introduction

A. Liver Anatomy and Function

The liver is one of the largest organs in the body and is the largest organ in the abdomen. It occupies the right upper quadrant of the abdomen. The liver is unique in that it has two major supplies of blood. In a normal liver, approximately three-quarters of the blood supply to the liver arrives through the portal vein. This blood is from the gastrointestinal tract and contains products resulting from digestion. A function of the liver is the processing of the material within this nutrient-rich blood. The remaining one-quarter of the blood supply to the liver arrives via the hepatic artery. This blood supply is more oxygenated that the blood within the portal vein [1]. The two blood streams mix within the liver and blood flows out of the liver via the hepatic veins.

Based on surface anatomy, the liver can be divided into four lobes. The largest lobe is the right lobe while the second largest is the left lobe. Two smaller lobes are the caudate and quadrate lobes located on the posterior liver. In the Couinaud classification, the liver can also be divided into eight functional segments. Each segment has a blood supply, blood outflow and biliary drainage independent from the other segments [2].

B. Liver Cancer

In the global human population, liver cancer is a major cause of death. In 2012, liver cancer caused an estimated 745,000 deaths. In the same year, approximately 780,000 new cases of liver cancer were diagnosed. [3].

Cancerous tumors can be classified as primary or secondary. A primary cancer of the liver is a cancer that arises from cells normally found in the liver. Metastasis is the process in which a primary tumor sheds cells. These cells travel to a different location within the body. A tumor then begins to grow at the new location. This tumor is known as a secondary tumor or metastasis. The characteristics of the secondary tumors are governed by the tissue type of the original tumor. The most common type of primary liver cancer is hepatocellular carcinoma (HCC). It accounts for 70% to 90% of all primary cancers of the liver [3].

Colorectal cancer (CRC) is a major source of metastases to the liver. In 2012, colorectal cancer was responsible for approximately 690,000 deaths worldwide [3]. Approximately 35% to 60% of patients with CRC will develop liver metastases [4] [5].

Different types of cancers often have different characteristics relevant to imaging and therapy. For instance, HCC tends to produce solitary tumors that are well vascularized while colorectal metastases within the liver often present as multiple, diffuse tumors.

C. Methods of Treatment

Often cancer cells are rapidly dividing and thus spend a higher fraction of time in mitosis than cells comprising normal tissue. Chemotherapy is a method of cancer treatment that is characterized by the use of drugs that primarily inhibit cell division. Usually these drugs are injected into the blood and the effects are system-wide. These drugs act on cells in mitosis. Chemotherapeutic drugs may affect other cells in the body that have a high rate of mitosis such as hair follicles and cells in the GI tract. It is

possible to infuse chemotherapy agents directly into the hepatic artery to increase the concentration of the chemotherapy drugs within the tumor [4].

Resection is the surgical removal of a tumor. It is possible to surgically isolate segments and remove them without damage to the remaining segments. The degree of tumor involvement in the liver often determines whether resection is a possible treatment or not. Other methods of treatment include external beam radiotherapy, chemoembolization and RF ablation.

D. Radioembolization

Radioembolization is a method often used when patients have unresectable liver cancer that is not responsive to chemotherapy [6]. Radioembolization has been used in the treatment of primary and metastatic cancer in the liver [7]. This treatment takes advantage of the difference in the blood supply to liver tumors and normal liver tissue. In many instances, a tumor will have a blood supply that is different from the blood supply to the normal liver. Through the process of angiogenesis, hepatic tumors are able to elicit the growth of new blood vessels. These new vessels supply the tumor with the required oxygen and nutrients necessary for growth. The hepatic artery contains blood that has a greater oxygen content than blood within the portal vein. Many tumors within the liver receive approximately 80% to 100% of incoming blood from the hepatic artery [7]. In the normal liver only approximately 25% of the blood is supplied by the hepatic artery. Normal liver tissue obtains the majority of blood from the portal vein.

The isotope yttrium-90 (Y-90) was an early choice for radioembolization therapy. In 1965, yttrium-90 was used in an arterial infusion to treat liver cancer [4]. Y-90 is still

the most widely used radionuclide for radioembolization therapy. The number of Y-90 radioembolization therapies performed in the U.S. is difficult to determine. One device used for this therapy is approved by the FDA under the Humanitarian Device Exemption. This limited the number of patients to 4,000 per year. In 2017, approval was granted to increase this limit to 8,000 per year. It is likely that thousands of Y-90 radioembolization therapies are performed each year in the U.S.

During Y-90 radioembolization, a catheter is threaded into the hepatic artery upstream of the tumor. Radioactive microspheres labelled with Y-90 are injected into the arterial blood stream. The microspheres are carried by the blood downstream and are captured in the capillaries of the tumor. The disintegration of the Y-90 nuclei via beta-minus decay delivers energetic electrons into the surrounding tissue. By selective placement of the microspheres such that a majority are captured in tumor tissue, a large absorbed dose of radiation can be delivered to tumors. The dose to the normal liver tissue can be kept relatively low. Radioembolization therapy is often referred to as Selective Internal Radiation Therapy (SIRT). In some instances, Y-90 radioembolization has resulted in remission. In some cases, Y-90 radioembolization is used to reduce the tumor size so that other methods such as surgery can be used [7]. Regardless, it is important to deliver a sufficient dose to the tumor while sparing the liver.

E. Yttrium-90

Yttrium is a group 3 transition metal. On the periodic chart it is found between the alkaline metal strontium, Sr, and the transition metal zirconium, Zr. Yttrium-90 is a radioactive isotope of yttrium with a half-life of 2.6684 days ± 0.0013 days (64.0416

hours ± 0.0312 hours) [8]. Y-90 decays to the stable ground state of Zr-90 by beta-minus decay. In 99.983% of decays, the maximum energy of the beta electron is 2278.7 keV and the average energy of the electron is 926.7 keV ± 0.8 keV [8] . There are other, low-probability decay pathways. In 0.0000014% of decays, there is a 2186 keV gamma emitted.

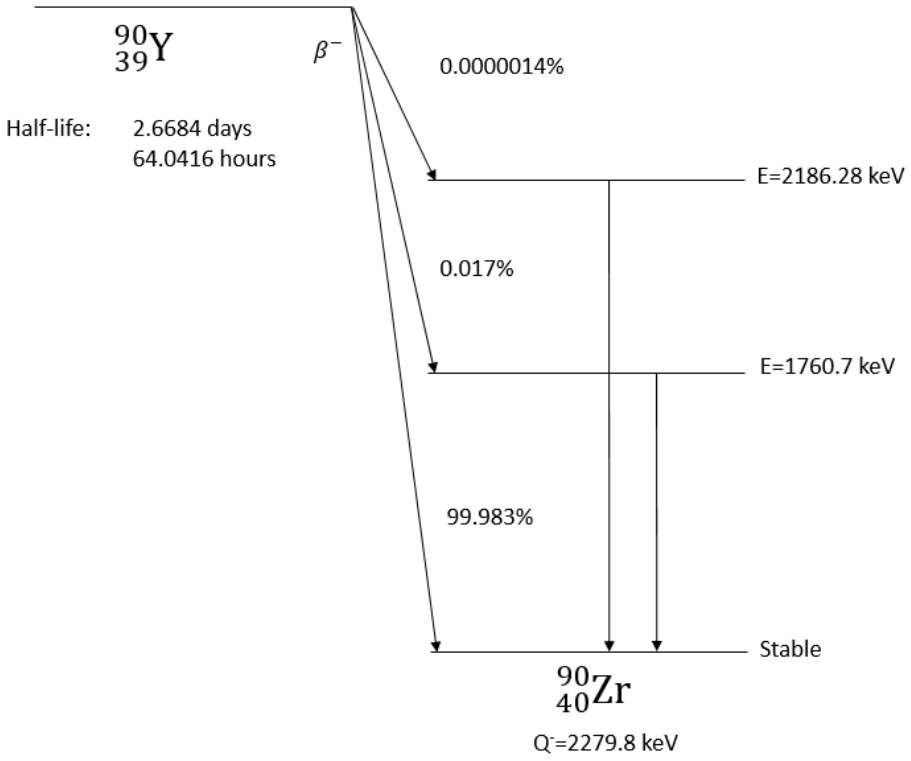

Figure 1: Decay Scheme of Yttrium-90

In 0.017% of decays, the maximum energy of the beta electron is 518.0 keV and the average energy of the electron is 163.7 keV. In this instance, the Zr-90 nucleus is left in an excited state 1760.7 keV above ground state [9]. Occasionally, the transition from this excited state results in internal pair production with a branching ratio of (31.86 ±

0.47) $\times 10^{-6}$ [10]. The positron emission from this rare pathway has been successfully used for Y-90 TOF PET imaging [11]–[13] .

For Y-90 decay, the average range of the electrons in soft tissue is 2.5 mm with a maximum range of 11 mm, with 90% of the energy deposited in 5.3 mm [6]. The most abundant cell within the liver is the hepatocyte. A typical hepatocyte is polygonal with sides measuring approximately 25 µm to 40 µm [14]. Thus, the range of a Y-90 beta-minus electron emitted with the average kinetic energy is approximately 100 cell diameters. As the electrons slow, kinetic energy is converted into excitation and ionization of the surrounding atoms and molecules. This deposition of energy constitutes the absorbed dose to the tissue.

The energetic electrons emitted during decay of Y-90 can undergo bremsstrahlung interactions within the surrounding tissue. The result is the emission of bremsstrahlung x-rays. The energy spectrum of the bremsstrahlung is broad with a maximum energy of 2.278 MeV. The radiation yield is the fraction of kinetic energy of the primary particle that is converted into electromagnetic radiation. From the ESTAR database published by NIST, for electrons with kinetic energy ranging from 2000 keV to 100 keV, the radiation yield ranges from 7.085×10^{-3} to 5.842×10^{-4} respectively [15].

F. Y-90 Microspheres

There are two FDA approved products available for Y-90 SIRT. Both of these products are in the form of microspheres. TheraSpheres™ are glass microspheres available from BTG International Ltd. The mean sphere diameter is in the range 20 µm to 30 µm [16] . The density of the microsphere is 3.2 g/mL [17]. Stable Y-89 is mixed

with the borosilicate glass that makes up the microsphere. Neutron activation of the microsphere produces Y-90. Thus, Y-90 is incorporated into the glass matrix that makes up the microsphere. These microspheres were approved 1999 by the FDA under a Humanitarian Device Exemption (HDE). TheraSpheres are indicated for "radiation treatment or as a neoadjuvant to surgery or transplantation in patients with unresectable hepatocellular carcinoma (HCC) who can have placement of appropriately positioned hepatic arterial catheters." [16].

SIR-Spheres are resin microspheres available from Sirtex Medical Inc. The diameter of the microspheres is 20 μm to 60 μm [18] The density of the resin microspheres is 1.6 g/mL [17]. The resin microspheres were approved by the FDA in 2002. In this case of the resin microspheres, the Y-90 is primarily bound to the surface of the resin microsphere. The surface chemistry and composition of SIR-spheres are proprietary [19].

The Y-90 microspheres are not detectable with clinically used x-ray modalities, MRI or sonography. Y-90 does not emit significant gamma radiation and cannot be imaged using typical nuclear medicine techniques. Therefore the choices for imaging Y-90 microspheres in vivo are limited. The options for clinical imaging of Y-90 include imaging bremsstrahlung x-rays with a gamma camera. The bremsstrahlung images tend to be of poor quality. Another method of clinical imaging utilizes Y-90 Time-of-Flight Positron Emission Tomography (Y-90 TOF PET). However, the number of positrons emitted by Y-90 emitted is low.

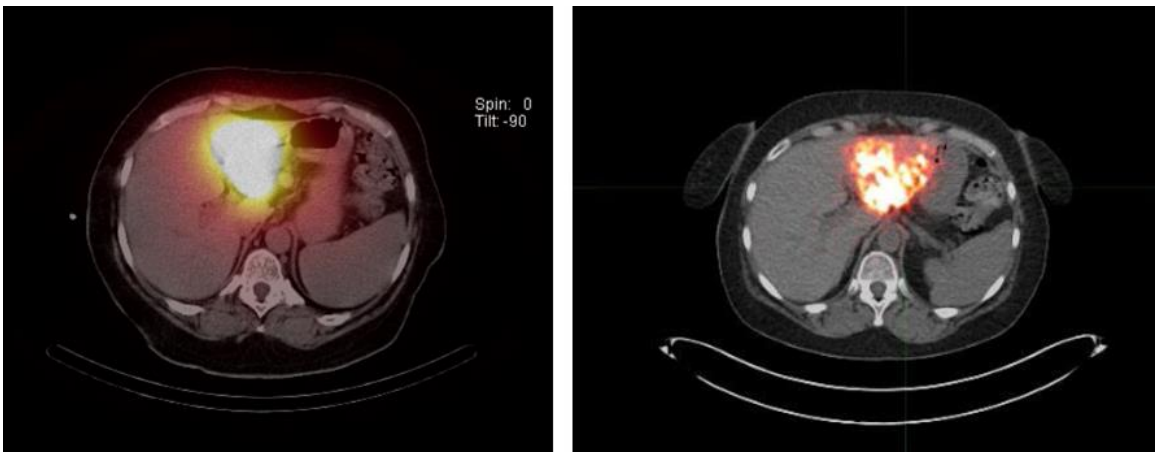

Figure 2: Post-therapy imaging of the same patient. Bremsstrahlung SPECT is on the left, Y-90 TOF PET is on right. Bremsstrahlung image has less spatial resolution and poorer contrast that TOF PET.

G. The Dosimetry of Y-90 Microspheres

The resin and glass Y-90 microspheres are permanent implants and are not expected to be removed from the body once implanted. The biological elimination of radioactivity is non-existent. The only means of elimination of radioactivity is through physical radioactive decay of the Y-90. The time-integrated activity in the source is given by the following equation.

$$\tilde{A}_h = \int_0^{\infty} A_h\,(t)dt \qquad (1.1)$$

This is the activity integrated from the calibration time, t = 0, to time equals infinity, t =∞. In the MIRD schema, $\tilde{A}_h$ is the cumulated activity in organ h. This is the total number of disintegrations that occur in organ h. The total number of disintegrations of Y-90 occurring in the implanted microspheres is given by the equation:

$$\tilde{A}_h = A_0 \cdot T_{1/2} \cdot \frac{1}{\ln(2)} \quad (1.2)$$

The term, $A_{0,}$ is the activity at the calibration time, t = 0 and $T_{1/2}$ is the half-life of Y-90. The half-life of Y-90 is 2.6684 days. For an initial activity of 1 GBq of Y-90, the cumulated activity, $\tilde{A}_h$ is:

$\tilde{A}_h$ = (1x10^9 disintegrations/sec) x [(2.6684 days)(86400 sec/day)] x [1/ln(2)]

= 3.326x10^{14} disintegrations

The total energy released as kinetic energy of the electrons during beta minus decay is given by the cumulated activity multiplied by the average kinetic energy of the electrons, 926.7 keV.

Total K.E. = 3.326x10^{14} disintegrations x 926.7 keV/disintegration

= 3.082x10^{17} keV

To calculate the absorbed dose to tissue assume that radiative energy loss due to bremsstrahlung is negligible.

(3.082x10^{20} eV) x (1.60218x10^{-19} Joule/eV)

= 49.38 Joules per GBq

A value of 49.38 ± 0.05 Joules per GBq has been published [8]. The authors state that the statistical uncertainties in the published values were taken into account.

The absorbed dose in tissue can be found using the following equation:

$$Dose(Gy) = 49.38 \frac{J}{GBq} \cdot \frac{A_0(GBq)}{Mass(kg)} \quad (1.3)$$

Where A_0 is the initial activity of the Y-90 microspheres in tissue and the mass term describes the mass of tissue into which the kinetic energy is being deposited.

H. Current Methods in Y-90 Radioembolization

Y-90 radioembolization therapy generally follows a course of action comprised of a pre-treatment mapping phase and a treatment phase. The performance of these two phases is often separated by approximately two weeks. A schematic of the actions involved in radioembolization therapy are shown in the graphic below.

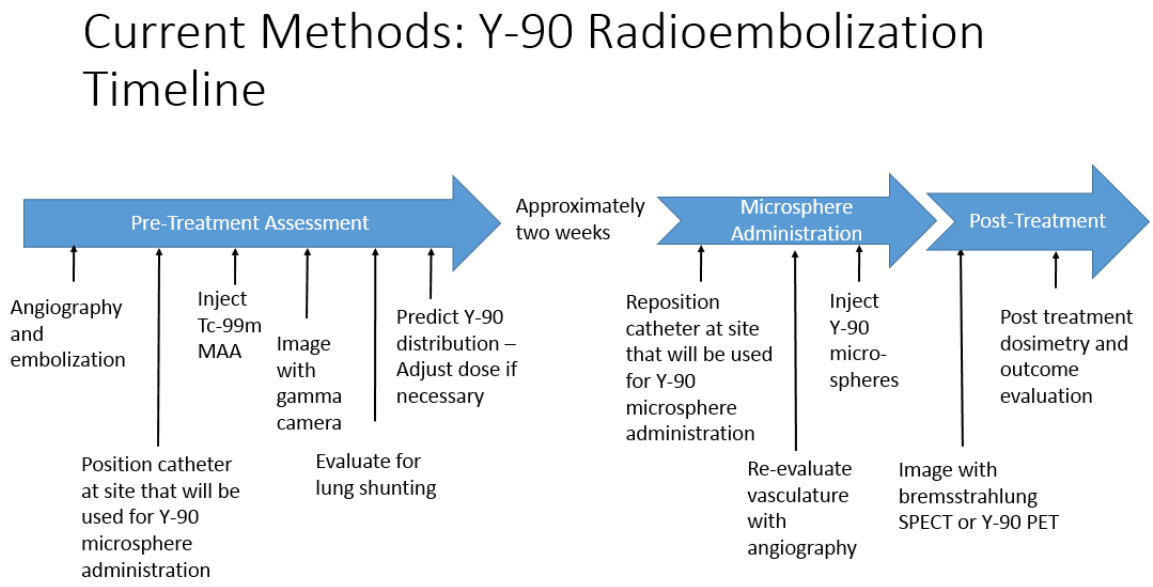

Figure 3: Schematic timeline of radioembolization therapy

I. Angiography and coil embolization

Prior to administration of the Y-90 microspheres, a careful evaluation of the hepatic vasculature is performed. Special attention is placed on the hepatic artery and associated vessels in the vicinity of the lobe or segment that is to be treated. Using fluoroscopy for guidance, a catheter is inserted into the vasculature supplying blood to the liver and tumor. Angiography with iodine contrast is then performed to investigate the patient-specific vasculature. A goal of this evaluation is to identify and isolate the arterial blood supply to the tumor. In addition, it is necessary to identify nearby vessels that supply blood to non-target areas such as the stomach, duodenum, pancreas and gall bladder. In some instances, embolization coils are used to occlude vessels to non-target areas. [2]. Serious complications can occur if Y-90 microspheres deposit in some of these areas. Abnormal vascular anatomy that has a high probability of producing reflux

of microspheres into non-target areas such as the stomach, pancreas and bowel is a contraindication for the administration of SIR-Spheres [18].

J. The Use of Tc-99m MAA

After angiography and coil embolization, a catheter is placed into the location that will be used in the future for the administration of Y-90 microspheres. At this time, the catheter is used to administer approximately 4 mCi of Tc-99m Macro Aggregated Albumin (MAA) [16], [18]. Albumin is a protein found in blood plasma. In the form of MAA, the albumin forms irregularly shaped aggregations of particles. The MAA size distribution does not match the size distribution of the microspheres. The package insert for TechneScan MAA (Malliinkrodt) states that 90% of the particles are between 10 to 40 microns and that no particle is greater than 150 microns [20]. Thus, the shape and size of typical MAA particles do not match the shape and size of the Y-90 microspheres. If shape and size are important to the particle distributions, then a difference in the MAA distribution and the Y-90 microsphere distribution may be expected.

The infusion rate of the Tc-99m MAA is dependent upon the user. The infusion of MAA may simulate the infusion of Y-90 microspheres[2]. No study has compared the infusion Tc-99m MAA and Y-90 microspheres. After the infusion, the catheter is removed. Once the patient is stabilized, they are moved to the nuclear medicine department where the Tc-99m MAA distribution is imaged using a gamma camera. Tc-99m is a commonly used radionuclide that decays by isomeric transition during which a 140 keV gamma photon is emitted. There are three purposes for imaging the distribution of Tc-99m MAA:

1. Evaluate shunting of particles to the lungs

2. Evaluate shunting to extrahepatic sites other than the lungs

3. Adjustment of administered activity

The distribution of the Tc-99m MAA is often used to adjust the amount of Y-90 that will be given during the therapeutic administered of the Y-90 microspheres [6] [18], In this instance, the Tc-99m MAA is being used as a surrogate particle for Y-90 and is being used to adjust the administered activity.

K. Evaluation for Lung Shunting

Arteriovenous shunting within the tumor may occur as a result of the modification of vessels by the tumor. Blood bypasses capillary beds through the modified vessels. This decreases the likelihood of microsphere deposition within the tumor. The result is that the blood-borne microspheres are "shunted" to the next major biological filter which is the lungs.

The fractional lung shunting is evaluated by measuring the relative amounts of Tc-99m activity in the lungs and liver. Using the images obtained with the gamma camera, a Region of Interest (ROI) is drawn around the lungs. The number of counts in the lung ROI is recorded. The amount of activity in the liver is measured by drawing a ROI around the liver and measuring the counts in the liver. The percent lung shunt is then calculated using the following formula:

$$Percent\ Lung\ Shunt = 100\% \times \frac{Lung\ Counts}{(Lung\ Counts + Liver\ Counts)} \qquad (1.4)$$

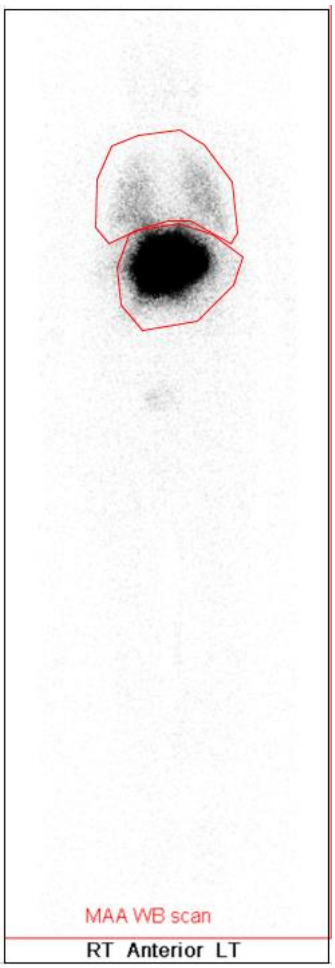

Figure 4: Lung shunt study with Tc-99m MAA. Regions of Interest (ROIs) are drawn in red around the liver and lungs. The number of events (counts) in each ROI is used to calculate the fraction of injected Tc-99m MAA that deposited within the lungs.

A "count" is a recorded event in which the gamma camera detected a gamma photon of interest. In this case, the gamma photons of interest are the 140 keV photons emitted by Tc-99m. The SIR-Sphere package insert recommends that anterior and posterior images of the thorax and abdomen are acquired with a large Field-of-View (FOV) gamma camera [18]. The recommendation also states that each image should contain between $7x10^5$ to $1x10^6$ counts.

To reduce the risk of radiation-induced pneumonitis the absorbed dose to the lungs must be kept at or below 30 Gy [18]. The percent lung shunt will be used to calculate and modify the amount of Y-90 SIR-Spheres that are administered to the patient. A significant amount of shunting may form the basis for denying the patient Y-90 therapy. SIR-Spheres are contraindicated for lung shunting in excess of 20% [18]. Likewise, for TheraSpheres it is necessary to keep the absorbed dose to the lungs at or below 30 Gy. The TheraSpheres package insert states the shunting of Y-90 microspheres to the lungs must be less than 16.5 mCi (0.61 GBq) [16].

There is evidence that Tc-99m MAA significantly degrades after injection [21] [22]. Two groups of researchers found that compared to lung shunt fractions measured early after administration, there was an increase in lung shunt fractions measured later (>4 hours) after administration. In one study, three patients had lung shunt fractions that were between 7% and 8% at the 1 hour post-administration time. At the >4 hour post-administration time, all three patients had measured lung shunt fractions in excess of 20% [22]. In these cases, the late lung shunt measurements could have resulted in misappropriate reduction in the administered activity of Y-90 microspheres or misappropriate exclusion from the treatment altogether.

Radioactive microspheres in locations such as the GI tract, pancreas or gall bladder can create problems. For instance, Y-90 microspheres in the GI tract can result in ulceration and bleeding. The deposition of microspheres in extrahepatic locations is often not due to intra-tumor shunting but is due to unplanned flow of microspheres into the arterial supply of the extrahepatic location. This is usually prevented by placing embolic coils prior to administration of the microspheres. A problem seen with the

degradation of the Tc-99m MAA is the creation of free technetium ion. The biodistribution of free technetium includes the stomach. The uptake of free Tc-99m in the stomach can mimic or mask the deposition of Tc-99m MAA particles in the stomach.

L. Adjustment of Administered Activity

Another purpose of the administration of Tc-99m MAA is to use the MAA as a surrogate particle for the prediction of the Y-90 dose deposition within the liver. The assumption is that the Tc-99m MAA will go to the same location in the normal liver and tumor as the Y-90 microspheres. However, the validity of this assumption is questionable. In some instances, the distribution of Tc-99m MAA has been shown to be a poor predictor of the Y-90 microsphere distribution [23]. Regardless, the distribution of Tc-99m MAA within the liver is used to make adjustment to the administered dose. To a certain degree this may be considered treatment planning. Compared to treatment planning methods used in external beam therapy and brachytherapy, the methods discussed below are crude and lack accuracy.

1. SIR spheres

In early versions of the package insert for SIR Spheres, there were two methods for calculating the amount of Y-90 to be administered to the patient [24]. These methods were the empirical model and the partition model. The latest version of the package insert now recommends using the Body Surface Area method for calculating the Y-90 activity to administer to the patient[18]. The empirical model is included for completeness.

a) The Empirical Method

In early clinical trials, this method was used to determine the activity of SIR-Spheres microspheres to be used. The empirical method was "abandoned after clinically observed toxicity"[6]. In the empirical method, the recommended amount of Y-90 activity to be administered was 2 to 3 GBq based on the percent involvement by the tumor in the liver. The amount of involvement by tumor was measured with CT or MRI [7]. For greater than 50% tumor involvement, the recommended activity is 3 GBq. For 25% to 50% involvement, the recommended activity is 2.5 GBq. For less than 25% involvement, the recommended activity is 2.0 GBq. The degree of lung shunting further modified the amount of administered activity.

b) Partition Method

Of the methods commonly used to modify the activity to be administered to the patient, the partition model is the most complex and most accurate. [25]. The partition model was proposed in 1996 by Ho et al.[26]. The partition model is based on the assumption that the distribution of Tc-99m MAA particles will be the same as the distribution of Y-90 microspheres. Another assumption is that the particles will be distributed among three compartments, the lungs, normal liver tissue and tumor. The three equations that follow are similar to the equations first introduced in the paper by Ho et al.

The activity that goes to the lungs, A_L, due to shunting can be expressed as:

$$A_L = A \times \left(\frac{L}{100}\right) \tag{1.5}$$

Where A is the total administered activity and L is the percent of administered activity that goes to the lungs. The measurements required to calculate the percent lung shunt were described earlier.

The activity that does not go to the lungs is divided among the tumor and normal liver. The relationship between the three compartments can be written as:

$$A_T + A_N = A \times \left(1 - \left(\frac{L}{100}\right)\right) \tag{1.6}$$

Here the activity in the tumor is A_T and the activity in the normal liver is A_N.

The tumor-to-normal tissue ratio of uptake of Tc-99m MAA in the liver, T/N, is given by:

$$\frac{T}{N} = \left(\frac{A_T}{M_T}\right) \Big/ \left(\frac{A_N}{M_N}\right) \tag{1.7}$$

This ratio is the activity per unit mass of tumor divided by the activity per unit mass of normal liver tissue. The mass of the tumor, M_T, and the mass of the liver, M_N, can be measured using CT or other tomographic modality. The tumor-to-normal tissue ratio (T/N) is measured from the distribution of Tc-99m MAA. The equations can be solved simultaneously for A_T and A_N. Once the activity in the tumor and the activity in the normal liver is determined, the absorbed dose to both regions can be calculated using:

$$Dose(Gy) = 49.38\frac{J}{GBq} \cdot \frac{A_0(GBq)}{Mass(kg)} \quad (1.3)$$

The partition model can be used to calculate the activity that needs to be administered to deliver a prescribed radiation dose to the tumor. Likewise, the partition model can be used to calculate the maximum activity that can be administered while keeping the radiation dose to the lungs or normal liver tissue below a desired value.

The estimated T/N is performed with the surrogate Tc-99m MAA particles. The true T/N ratio can only be measured after the administration of Y-90 microspheres [25]. Ho made measurements of the Y-90 distribution using a detector to measure beta activity during laparotomy [26]. A more modern, less invasive approach is to measure the post-treatment Y-90 distribution using Y-90 PET imaging [25].

For the partition model to be valid, the assumption is made that the T/N ratio is the same for the Tc-99m MAA and the Y-90 microspheres for all parts of the liver. The distribution of Tc-99m MAA within the three compartments should match the distribution of Y-90 microspheres. Any mismatch between the two distributions will result in a loss of accuracy in the estimated dose from Y-90. The greater the degree of mismatch, the greater is the inaccuracy in the calculated dose.

In 2012, a group of experts compared the various means of determining the activity to be given to the patient [7]. They concluded that for resin microspheres, the partition method was the method of choice except in the case of small tumors with

diffuse margins. In these instances the BSA method was recommended. The group stated, "Thus, relatively few metastases will qualify for partition model planning" [7].

The use of a PET labeled surrogate and the expected improvement in image quality and quantification may enable better T/N ratio determination for small tumors than what is currently possible. The ability of the new positron emitting surrogate particles to estimate the true T/N ratio is beyond the scope of this dissertation. The predictive accuracy of a new surrogate particles will have to be determined by use in clinical trials. The goal of this project is to develop the tool not to evaluate its clinical usefulness.

c) Body Surface Area (BSA) Method

The Body Surface Area (BSA) method does not take into account the tumor-to-normal liver (T/N) ratio [25]. Instead the method relies upon the body surface area of the patient and the measured volumes of the liver and tumor. This method is the only recommended method in the most recent (Feb. 2017) version of the SIR-Spheres package insert [18]. Supposedly, the liver volume correlates with the body surface area [6] [7] [18].

For SIR-Spheres, the prescribed activity for the whole liver or bilobar treatments can be calculated using the BSA method with following formula:

$$Prescribed\ Activity\ (GBq) = (BSA(m^2) - 0.2) + \left(\frac{V_{Tumor}}{V_{Liver}}\right) \qquad (1.8)$$

Where BSA is given by the formula:

$$BSA = 0.20247 \times \left(height(m)\right)^{0.725} \times \left(weight(kg)\right)^{0.425} \quad (1.9)$$

V_{Tumor} is the volume of tumor in the liver. V_{Liver} is the total volume of the liver which includes non-tumor liver and tumor [18]. In this case, the liver volume would need to be measured with CT or MRI.

If visible tumors are present in only one lobe, the recommendation is to administer the microspheres to that lobe only. This would confine the radiation dose to the lobe with the tumor.

There is a further modification to the BSA calculations for lobar treatments.

$$Prescribed\ Activity\ (GBq) = \left[(BSA(m^2) - 0.2) + \left(\frac{V_{Tumor}}{V_{Lobe}}\right)\right] \times \left(\frac{V_{Lobe}}{V_{Liver}}\right) \quad (1.10)$$

Where V_{Lobe} is the volume of the affected lobe. The other variables remain the same.

There is mention in the literature that there is "no known association correlating BSA with liver volume, tumor volume or radiation sensitivity." [27].

2. MIRD Method (glass microspheres)

For TheraSpheres, the recommended method of calculating the activity to administer the patient is based on the MIRD (Medical Internal Radiation Dose) methodology. This method is based on the assumption of a homogeneous distribution of

activity within the liver [28]. The method in the TheraSpheres package insert uses an energy deposition of 50 joules per kilogram of tissue for every GBq of Y-90 administered. The nominal target dose to the liver is between 80 Gy to 150 Gy [16]. To calculate the required amount of activity to deliver this dose, the TheraSpheres package insert has the following equation:

$$Activity\ Required(GBq) = \frac{Desired\ Dose(Gy) \times Liver\ Mass(kg)}{50} \tag{1.11}$$

The liver volume and mass can be found with CT or other modality. The package insert also has a formula for calculating the dose to the liver after administration:

$$Dose(Gy) = 50 \times \frac{Injected\ Activity(GBq) \times (1 - F)}{Liver\ Mass(kg)} \tag{1.12}$$

The term, F, is the lung shunt fraction. The recommended upper limit of activity that can be shunted to the lungs is 0.61 GBq. This activity corresponds to a dose of approximately 30 Gy using the assumption that the mass of both lungs is 1 kg [16].

0.61 GBq x 50 Gy/GBq = 30.5 Gy

Thus the upper limit of dose to the lungs from TheraSpheres is approximately the same as the upper limit recommended for SIR-Spheres, 30 Gy. This method does not

take into account difference in uptake between tumor and normal tissue. Beyond adjustment for liver mass, there is no adjustment for patient-specific parameters such as the T/N ratio.

M. Pre-Treatment Dosimetry

While, Tc-99m MAA can be used for crude treatment planning, it will be worthwhile to create a new surrogate that is better than Tc-99m MAA. An improvement in pre-treatment imaging and mapping of the likely Y-90 distribution would provide data for better treatment planning and dosimetry. Better data enables the improvement of tools such as dose volume histograms (DVH) which are currently not being used with Tc-99m MAA pre-treatment imaging. Improved pre-treatment imaging may also help identify factors that may correlate to better Y-90 delivery and patient outcomes. High quality pre-treatment data can help avoid delivery of toxic levels of radiation to the normal liver parenchyma and simultaneously help avoid under-dosing the tumor.

Advancement in image-based dosimetry can enable more advanced treatment planning techniques such as fractionation. It has been shown that the Y-90 microspheres deposit in the outer layers of some tumors [29]. The concentration of microspheres in the outer layers can be many times that found in the core. Thus, the outer shell of the tumor receives the largest radiation dose. Fractionation is the planned delivery of multiple doses or "fractions" over time and is commonly used in external beam radiation therapy. A fraction is a delivered dose which kills the cells in the outer layer of the tumor. The tumor size is then reduced and simultaneously the hypoxic core receives more oxygen. Cells that are well oxygenated tend to be more radiation sensitive. At a planned point in

time, another fraction of radiation is delivered. In this way, the tumor is reduced through a systematic application of radiation over time until the entire tumor is destroyed. The development of a new surrogate microsphere may provide pre-treatment dosimetry adequate for fractionation using Y-90 microspheres.

N. Matching Distributions of Surrogate and Therapy Particles

The accuracy of pre-treatment dosimetry depends on accurately predicting the Y-90 microsphere distribution. There have been several investigations into the predictive value of Tc-99m MAA for Y-90 microsphere distribution.

In one study by Ilhan et al., the authors compared the predictive value of Tc-99m MAA SPECT for more than 500 patients with a variety of tumor types [30]. The researchers graded tumor uptake in pre-treatment Tc-99m MAA SPECT and post-treatment Y-90 bremsstrahlung SPECT and placed them into one of four grades. The metric used for tumor uptake was the Tissue to Background Ratio (TBR).

The grade 1 tumors had uptake that was homogeneously greater than the uptake in the normal liver tissue. Grade 2 lesions had heterogeneous uptake that was greater than the uptake in the normal liver tissue. Grades 3 and 4 were uptake in tumor tissue that was equal to or less than normal liver tissue respectively. Statistical tests were used to assess the differences between the Tc-99m MAA SPECT and Y-90 bremsstrahlung SPECT. In general, most lesions that had a high Tc-99m MAA uptake also had a high Y-90 uptake. Greater than 90% of the lesions studied had a high uptake with a grade of 1 or 2. Of the 57 patients that had a low Tc-99m MAA uptake of 3 or 4, 67% of these patients had a grade 1 or 2 high uptake of Y-90 microspheres. The study recommended that patients

should not be excluded from radioembolization based on a low pre-therapy Tc-99m MAA uptake [30].

In another study by Wondergem et al., the authors did a retrospective analysis on patients who had Y-90 radioembolization therapy [23]. They measured the agreement of Tc-99m MAA SPECT and Y-90 bremsstrahlung SPECT distributions. They did this by normalizing the Tc-99m MAA distribution to the total administered activity of Y-90. They then used Bland-Altman analysis to compare the two activity distributions. The authors claim that this is the statistical method of choice when comparing the performance of two instruments measuring the same quantity. They concluded that the Tc-99m MAA distribution did not accurately predict the distribution of Y-90 microspheres. They also identified factors that may have contributed to the mismatch between the distributions. The authors also mention that using Y-90 PET instead of Y-90 bremsstrahlung SPECT could improve post-treatment quantification.

Another group, Jiang et al., investigated catheter placement and segmental perfusion differences between MAA and Y-90 distributions [2]. They looked at factors including the difference in catheter placement, the proximity to a bifurcation and proximity to a side artery. The found a high degree of correlation. They also pointed out that the particle size, shape, and density play a role in causing a difference in particle distributions.

Another study was performed by Gnesin et al. to examine the agreement between pre-therapy Tc-99m MAA SPECT/CT dosimetry with post-therapy Y-90 TOF PET/CT for resin and glass microspheres. [11]. They created voxelized dose maps from the Tc-99m MAA SPECT/CT and the Y-90 TOF PET. The dose gold standard was the

voxelized dose map produced by the Y-90 TOF PET/CT. The dose map obtained from the Tc-99m MAA SPECT was compared to the baseline dose map produced from the Y-90 TOF PET. The comparison was done for tumor volumes and non-tumor volumes. The agreement between the dose maps was measured using a statistical metric known as the Lin concordance. The conclusion was that Tc-99m MAA SPECT/CT provided good estimates of the absorbed doses from Y-90. The agreement between the MAA and Y-90 dose maps was much better for tumors larger than 150 mL [11]. A sphere with a volume of 150 cm^3 has a radius of 3.3 cm. The use of a surrogate PET microsphere and superior resolution of PET imaging would likely produce good agreement with smaller volumes.

O. Factors That May Affect the Predictive Value of Surrogate Particles

The following factors may affect the predictive value of surrogate particles and may be important in the mismatch between Tc-99m MAA distribution and Y-90 microsphere distribution:

1. Factors dependent on operator or patient:

- Distance between the Tc-99m MAA administration and subsequent Y-90 microsphere administration. Researchers have found that in some cases the distance between the two injections could be greater than 5mm [2].
- Distance from catheter to bifurcation. The distance to a bifurcation of the artery was important [2].

- The angle of the catheter in the vessel lumen. The angle of the catheter in the vessel can change the flow dynamics of the blood in the vicinity of the catheter [23].
- Differences in rates of injection and rhythm of injection between Tc-99m MAA and Y-90 microsphere injections may lead to mismatch [2].
- The length of the procedure and the number of interventions may increase the likelihood of vasospasm and vasoconstriction. This will alter blood flow pattern.

2. Factors dependent on technical parameters:

- The size of the surrogate particles should closely match the size of the therapy microspheres. Ideally, the size of the surrogate particles and the therapy microspheres will be identical.
- The density of surrogate particle may be important. It is not entirely clear how dependent the deposition is to microsphere density. The surrogate particles may perform adequately even if the density is not the same as therapy microspheres.
- The shape of the surrogate and therapy microspheres should be nearly the same. The Y-90 microspheres are spherical whereas MAA particles tend to be irregularly-shaped random aggregations.
- The surface chemistry of the surrogate is likely important. The surrogate should readily bind to the labeling radionuclide. It should not bind to vessel walls or to similar particles to form aggregations. Clusters and

aggregations of microspheres could lodge near the catheter or other locations which would lead to mismatch.

- Imaging modality affects image quality and quantification. Poor resolution and contrast recovery can lead to mismatch.
- The activity per microsphere may alter the predictive value of the surrogate particles. For resin SIR-Spheres the activity per microsphere is 50 Bq. For glass TheraSpheres the activity per microsphere is approximately 2500 Bq. It requires significantly more resin microspheres to achieve a target dose. A large number of microspheres has a greater likelihood of changing the blood flow during administration and altering the final distribution. In addition, the embolic effect may ultimately reduce oxygen and effectiveness of the radiation delivered to the tumor.
- Degradation of surrogate over time can cause a change in the distribution pattern. For instance, the degradation of MAA may alter the distribution of the activity over time. Thus, the predictive value of Tc-99m MAA as a surrogate for the Y-90 is likely changing with time. The degree of the change and the clinical impact is usually unknown.

P. Development of Surrogate Microspheres

Effort has been placed into finding a suitable surrogate microsphere for pre-therapy treatment planning. A brief survey of different investigations is presented here.

A promising F-18 resin surrogate was developed [19]. However, in vivo leaching of the F-18 was a problem. The instability of the radiolabel may have been

especially difficult to overcome since the microsphere resin material was proprietary. The details of the surface chemistry were not well known.

Microspheres made of poly(L-lactic acid), PLLA, embedded with Holmium-166 have been developed [23] [31]. Holmium-166 has a half-life of 26.8 hours and emits beta-minus electrons. The maximum energy of the electrons is 1.85 MeV. Holmium also emits gamma photons with and energy of 80.6 keV which is easily imaged with a gamma camera. Holmium-166 is also paramagnetic which enables imaging with MRI. The Ho-166 PLLA microspheres can be used for both pre-treatment imaging and therapy [31].

The strategy in which the same microsphere is used for both pre-treatment imaging and therapy has been investigated by Verger et al. In their work they use starch-based microparticles as vehicles for Tc-99m, Ga-68 and Re-188 [32]. When SPECT will be used for pre-treatment imaging, the starch-based microparticles are labeled with Tc-99m. The microparticles can be labeled with Ga-68 for PET imaging prior to treatment. The starch-based microparticles can then be labeled with Re-188 to form the therapeutic microparticles. Re-188 decays by beta-minus decay with a half-life of 16.98 hours. The beta-minus electron has a maximum energy of 2.1 MeV. Re-188 also emits a gamma with an energy of 155 keV. This can be readily imaged with a gamma camera.

An issue regarding the adoption of a surrogate replacement for Tc-99m MAA is that MAA is specified in the package insert and is the accepted method for performing the evaluation for lung shunting and extrahepatic deposition. The transition from Tc-99m MAA to a new surrogate may be easier if it demonstrated that co-injection of both particles is possible. Co-injection would enable the clinical demonstration of the microsphere in parallel to the current method of using Tc-99m MAA for evaluation of

shunting and adjustment of the administered activity. It may be worthwhile to investigate whether a small amount of positron emitter will interfere with Tc-99m MAA lung shunt measurements. If the positron-emitting isotope does interfere the Tc-99m MAA measurements, then determination of the magnitude of the interference should be determined. Ideally, the activity of the positron emitter would be such that this activity would be low enough to not affect the Tc-99m measurements yet would be large enough that PET data could be acquired to be useful for dosimetry.

Q. Post-Therapy Imaging and Dosimetry

A potential application for a positron emitting surrogate microsphere is in post-therapy dosimetry. One method of performing post-therapy dosimetry is done by imaging bremsstrahlung emission with a SPECT camera. The bremsstrahlung x-rays are emitted as the Y-90 beta minus particle slows in tissue. The energy spectrum of the emitted bremsstrahlung x-rays is broad and the image quality is poor (see Figure 2). Good quantification accuracy based on bremsstrahlung imaging is difficult to achieve due to the poor spatial resolution which is on the order of centimeters. An alternative to bremsstrahlung imaging is Y-90 Time-of-Flight (TOF) PET. Y-90 TOF PET has been shown to be superior to bremsstrahlung SPECT for post-therapy image-based dosimetry[33].

There are several issues with Y-90 TOF PET imaging. Positron-electron pair formation during the decay of Y-90 is relatively rare. Approximately 32 positron-electron pairs are formed for every million decays. Thus, the count rate from Y-90 is

low. Useful Y-90 TOF PET imaging requires large activity, relatively long counting time, or increased detector sensitivity.

The materials that are used to make the PET scanner, may be radioactive. When performing Y-90 TOF PET, there are background sources that are typically ignored when performing PET with other radionuclides. LSO and LYSO are commonly used lutetium-containing scintillation crystals used in PET scanners. Approximately 2.6% of the lutetium in LSO is Lu-176 which decays by beta-minus decay. The beta-minus decay is accompanied by coincident gamma emissions at 307, 202 and 88 keV [34]. The lutetium background can typically be ignored except when imaging with very low count rates such as in Y-90 PET. Other sources of random coincidences include coincidences with high-energy bremsstrahlung produced by slowing beta-minus electrons.

A possible method of enhancing post-therapy PET imaging is the use of surrogate microspheres that emit large amount of positrons. These could be co-injected with the Y-90 therapy microspheres and "boost" the positron signal for PET imaging.

If the specific activity is high enough then a relatively few surrogate microspheres would be needed to achieve the desired increase in positron emissions. Fewer surrogate microspheres injected translates into less likelihood of inducing an embolic effect. A microsphere labeled with a high-yield positron emitter could potentially produce on the order of 10^4 more positrons than a Y-90 labeled microsphere of the same activity. The increase in positron counts could overcome problems associated with the very low count rates found in Y-90 TOF PET.

The poor performance of current methods also limits the ability to accurately measure the radiation dose delivered to the tumor tissues and normal tissues. This affects the post-therapy assessment of delivered dose and correlation with treatment outcomes.

R. Development of Positron-Emitting Surrogate Microsphere

1. Choice of Radionuclide

The inclusion of Positron Emission Tomography (PET) imaging for pre-treatment dosimetry requires the selection of a positron emitting radionuclide to label the surrogate microspheres. Properties of the radionuclide that need to be considered include half-life, toxicity, binding properties, and availability. In addition, the characteristics of the emitted radiations is very important. A pure positron emitter is more desirable than a positron emitter that has coincident gamma emissions. Coincident gamma emissions may be mistaken for true counts during PET acquisition leading to noisy images.

Fluorine-18 is the most widely used radionuclide in PET. Thus, it has an existing distribution network and is readily available to PET imaging centers. Fluorine-18 has a half-life of 109.77 minutes[35], [36]. The half-life is long enough to allow for transport and preparation of microspheres. The half-life is short enough that activity from clinical imaging will be gone within 24 hours. F-18 emits a positron in 96.8% of decays [9]. Thus, the photon abundance for 511 keV is 2 × 96.8% or 193.6%. The mean energy of the positron is 249.5 keV while the maximum energy is 634 keV [9]. The mean range of the positron in water is 0.64 mm and maximum range is 2.3 mm [37]. The range in water is relatively small compared to other positron emitters. This is a desirable feature. A

long-range positron is likely to travel farther from the parent nucleus before undergoing positron-electron annihilation. As the positron travels from the point of origin, the uncertainty regarding the location of the point of origin increases. This manifests as a contribution to image blur in PET. As the positron range increases, the resulting image blur increases and spatial resolution decreases.

Modern PET scanners are optimized for the imaging of F-18. It is superior to most other radionuclides in spatial resolution, half-life, availability and ease of use. In addition, the chemistry of binding fluorine to potential microsphere materials is relatively easier than the organometallic chemistry involved with other potential radionuclides. Other possible candidate radionuclides for use in surrogate microspheres include Ga-68, Cu-64, Zr-89 and Y-86.

Ga-68 is available in the form of a Ge-68/Ga-68 generator [38]. Thus, Ga-68 could be available in areas that are not serviced by a cyclotron facility. The generator is expensive and the availability of Ga-68 is more limited than the availability of F-18. Gallium is a metal and the binding to microspheres often involves the use of a chelator to bind organic molecules. One group of investigators has successfully labeled hydroxyapatite nanoparticles with Ga-68[39]. Gallium also shares chemical properties with iron and can take the place of iron in some biological processes [40]. This could be problematic for a gallium-labeled surrogate microsphere in the blood stream.

Copper-64 is a radionuclide that has been tested for use in surrogate microspheres [41]. In one investigation, resin microspheres labeled with Cu-64 were injected into rats. The binding proved to be unstable. It was found that albumin had an affinity for the Cu-64 bound to the microsphere. The albumin in the blood was likely responsible for

removing Cu-64 from the microspheres. However, other properties of Cu-64 make it attractive for use as a surrogate radiolabel. It has a half-life of 12.7 hours. The maximum energy of the Cu-64 positron is 0.6 MeV. This is a relatively low-energy positron which tends to result in good spatial resolution in PET imaging. One strategy to avoid Cu-64 binding with albumin is the incorporation of naturally abundant copper into glass microspheres. The glass is irradiated in a high flux source of neutrons to produce Cu-64. The incorporation of the Cu-64 into the glass greatly reduces leaching. However, the process is time consuming and requires access to special facilities for irradiation of the microspheres.

In the investigation performed for Cu-64, testing was done with Y-86 and Zr-89 [41]. The in vivo stability of both were acceptable. The Y-86 emits a high-energy positron (3.2 MeV) which would likely result in relatively poor spatial resolution compared to other radionuclides used in PET. Y-86 also produces several prompt gammas. This "dirty" energy spectrum may confound PET data acquisition and inhibit accurate quantification. Zr-89 has a relatively low-energy positron (0.9 MeV) and no prompt gamma rays. However, the half-life is comparatively long at 78.4 hours. Ten half-lives is nearly 33 days. This isotope would likely not work well in the current therapy workflow where the surrogate is administered approximately one to two weeks prior to the administration of the Y-90 microspheres. If Zr-89 was used as a surrogate, significant activity would be present and likely show in post-therapy bremsstrahlung SPECT or TOF PET imaging.

2. Choice of Microsphere Material

Ion exchange resins were initially investigated for possible microsphere material. There are commercial suppliers of microspheres composed of ion exchange resins. Previous investigators have had success labeling these types of microspheres [41]. In addition, SIR-Spheres are resin microspheres made of a proprietary resin bound to Y-90. The investigation into ion exchange resins resulted in several concerns. One goal of this project was to create a surrogate microsphere that would be close in size to the therapeutic microspheres. The investigation into commercially available ion exchange resins found that significant swelling of the resin beads could be expected. Another potential problem was identified in regards to the ability of the resins to tightly bind fluoride. In the Bio-Rad publication, Guide to Ion Exchange, there is a table with the title "Relative Selectivity of Various Counterions" [42]. The table lists 23 negative ions and their relative selectivity. The Guide states, "In general, the lower the selectivity of the counterion the more readily it exchanges with another ion of like charge". For the resins used for negative ion, fluoride, F^-, has the lowest selectivity in the list. This leads to the conclusion that F^- ion would not be strongly bound to the resin. The 22 other negative ions on the selectivity list would likely replace the fluoride ion in the resin. For in vivo applications, this could lead to removal of the ion from the resin by blood products.

Continuation of the search for a microsphere material, resulted in finding a commercially available hydroxyapatite microsphere. These microspheres are sold by Bio-Rad as ceramic hydroxyapatite "CHT" microspheres. The microspheres are made from crystalline hydroxyapatite material that is compressed and sintered at high temperatures. There are two types available, Type I and Type II. The two types are

chemically the same. The sintering temperatures and times are different. The Bio-Rad CHT microspheres are designed to be used as a chromatography medium in the purification of biological molecules. The two types of CHT have different binding properties to proteins. Subsequent research found that significant swelling of the hydroxyapatite microspheres was unlikely.

Hydroxyapatite was identified as a promising material since it was known that [F-18] NaF is used for PET skeletal imaging and hydroxyapatite is the primary mineral component of bone. Hydroxyapatite is already widely used clinically. There are a variety of hydroxyapatite-containing materials used as bone substitutes. These materials are usually placed in the body as a treatment for a bone defect. Synthetic ceramic bone substitutes are often a mixture of hydroxyapatite and tricalcium phosphate (TCP) [43]. Hydroxyapatite is the crystalline form of TCP, The ratio of the hydroxyapatite and the TCP is adjusted based on the application. Hydroxyapatite usually provides better mechanical strength whereas TCP enhances biodegradation. Much work has been done to optimize bone substitutes for porosity and to mimic natural bone. Another variety of bone substitutes are the calcium phosphate cements (CPCs) which consist of a calcium phosphate powder. When mixed with a liquid, the resulting cement hardens into nanocrystaline hydroxyapatite. These cements are FDA approved for repair of non-load bearing bone defects [44].

Another potential application of hydroxyapatite is the removal of excessive fluoride from drinking water. In a study by Fan et al., the investigators showed that hydroxyapatite readily binds to fluorine ions in water [45]. They found that the adsorbed fluoride molecules on hydroxyapatite plateaus at approximately $5x10^{13}$ fluoride

molecules per gram. If the assumption is made that the fluoride is in the form of F-18, $5x10^{13}$ fluoride molecules per gram of hydroxyapatite is equivalent to 5.25 GBq per gram or 142 mCi per gram.

The bulk density of CHT hydroxyapatite microspheres is 0.63 g/cm^3[46] A random close packing of spheres will have a packing fraction of approximately 0.63 [47]. If a packing density of 0.63 is assumed, then the density of a CHT microsphere is 1 g/cm^3. The actual density of the individual microspheres is slightly greater than the density of water. This is based on observations that in a mixture of water and CHT microspheres, the microspheres will slowly settle to the bottom of the container. The CHT microspheres are available in three sizes, 20 ± 2 µm, 40 ± 4 µm and 80 ± 8 µm. A gram of 40 µm CHT microspheres contains $3x10^7$ microspheres. A gram of 20 µm CHT microspheres contains 2.4 x 10^8 microspheres. Based on the 5.25 GBq of F-18 per gram reported by Fan et al. it was expected that 176 Bq per microsphere for 40 µm was achievable. A similar calculation for 20 µm results in an estimate of 22 Bq per microsphere. This activity per microsphere is approximately the same order of magnitude reported for other radiolabeled microspheres investigated for use as surrogates [41].

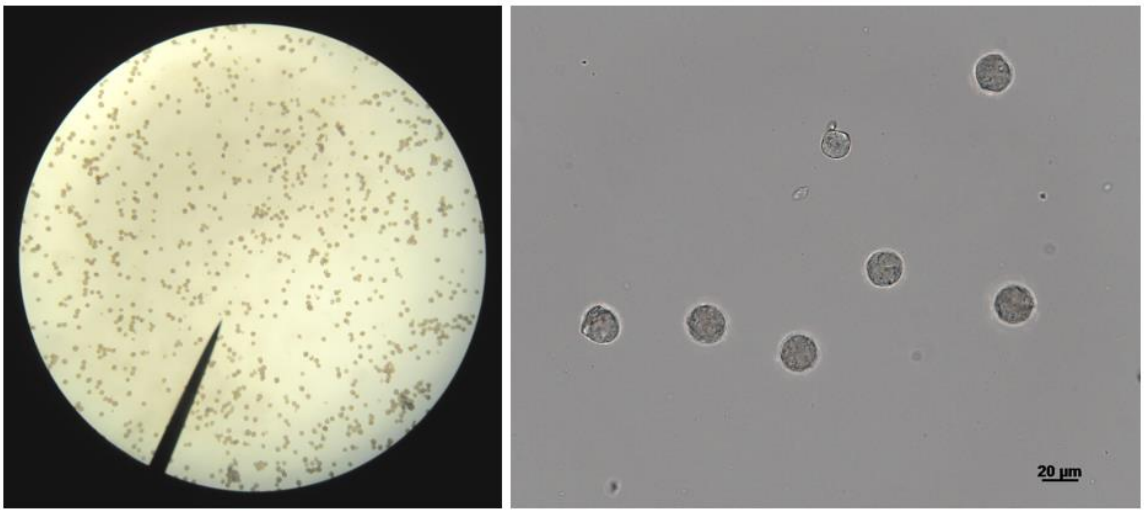

Figure 5: Micrographs of Type I CHT ceramic hydroxyapatite microspheres. Image on left was acquired with American Optical Spencer 60 using 10X objective. Image on right was acquired with a Zeiss AxioSkop MOT2 microscope at 40X magnification. Microsphere diameters consistent with manufacturer's claims.

As the activity per microsphere increases, the number of microspheres required for a desired activity decreases. Reducing the number of injected microspheres reduces the likelihood of embolic effect and the redirection of blood flow. A large amount of activity per microsphere combined with a positron emitting radionuclide with a high positron branching ratio results in a strong signal from a relatively small amount of microspheres. Based on this information, it was felt that further investigation of F-18 to CHT hydroxyapatite microspheres was worthwhile.

The unit cell of hydroxyapatite considered to have a hexagonal lattice. The unit cell is composed of two versions of the formula units $Ca_5(P0_4)_3OH$ [43]. The formula for hydroxyapatite is typically written as $Ca_{10}(PO_4)_6(OH)_2$. There are two mechanisms in which fluoride is incorporated into the apatite crystal structure [39], [48]. One mechanism is ionic exchange via surface adsorption. This occurs at the CaOH sites [48].

At these sites the F^- is exchanged for water or OH depending on the on pH. Once the fluoride has been adsorbed onto the surface, diffusion of fluoride into the crystal lattice may lead to substitution of a hydroxide ion, OH^-, with the F^-. The fluoride is smaller than the hydroxide ion. When the fluoride is substituted for OH- within the crystal lattice, the result is more thermodynamically stable. The resulting material is fluorapatite, $Ca_{10}(PO_4)_6F_2$.

There is evidence that the fluoride diffuses several nanometers into the bulk hydroxyapatite and will reach equilibrium. The resulting fluorapatite layer may form a barrier to further penetration of the F- into the hydroxyapatite [49]. It was expected that the ceramic form of hydroxyapatite would present more surface area per unit mass than the highly crystalline forms. As such the structure of the CHT would be favorable for surface adsorption.

Sandhöfer et al., have successfully bound F-18 to hydroxyapatite crystalline nanoparticles [39]. The synthetic material was similar to biologically produced apatite in regards to chemical composition and morphology. The particle size of the apatite nanoparticles was less than 30 nm. This is three orders of magnitude smaller than the ceramic hydroxyapatite microspheres that were used in this dissertation. This group noted that hydroxyapatite nanoparticles have a tendency to form clusters [39]. They treated the nanoparticles with citrate to reduce the tendency to aggregate. In the case of hydroxyapatite nanoparticles, the radiolabeling was done by mixing F-18 fluoride ions with the nanoparticles in an aqueous solution. The initial radiopharmaceutical was [F-18] NaF. The binding equilibrium was achieved in less than 10 minutes. The stability of these radiolabeled hydroxyapatite nanoparticles was tested in saline and phosphate

buffered saline. After 2 hours, the bound activity on the hydroxyapatite was greater than 95%.

The Sandhöfer group also tested the stability of the radiolabel in a rat. They found that initially the activity localized in the lungs and then migrated to the liver. This was attributed to particle migration due to the small particle size and not free fluoride ion. After 90 minutes, activity in the joints of the skeleton and kidneys was not seen. The conclusion was that the F-18 label was stable in vivo [39].

Fan et al. used highly crystalline hydroxyapatite crystals in the 200 micron range [45]. Their equilibrium time was nearly two hours. The results from Fan and Sandhöfer, indicate that the time required to reach labeling equilibrium seemed to decrease with decreasing particle size. The anticipated labeling time for the CHT microspheres was somewhere between 10 minutes and two hours.

Another investigation of F-18 binding to hydroxyapatite was published by Jauregui-Osoro et al. [50]. In this study, three different forms of hydroxyapatite crystals were synthesized and another form was commercially purchased. All types tested were nanoparticles 200 nm or less in size. This is two orders of magnitude smaller than the CHT microspheres planned for use this study. Jauregui-Osoro et al. injected F-18 radiolabeled hydroxyapatite into the tail veins of mice. The radiolabel of the nanoparticles that remained in the lungs was stable. There was evidence that nanoparticles that migrated to the liver and spleen were taken up by phagocytic cells of the reticuloendothelial system. The size of these macrophages appear to be approximately 10 μm in diameter [50]. These nanoparticles then gradually released F-18 which then collected in the skeleton. It was expected that the CHT microspheres would

not undergo uptake by phagocytic cells due to the size of the microspheres. The CHT microspheres are 20 μm or 40 μm in diameter. A study by Champion et al. found that particles with diameters 2 μm to 3 μm of had maximum particle uptake by macrophages [51].

Das et al. manufactured hydroxyapatite microspheres in the 20 to 60 μm size range [52]. They radiolabeled their microspheres with holmium-166. They were able to image the Ho-166 labeled microspheres with a gamma camera using the 81 keV photons. They mention that hydroxyapatite is biodegradable and is eliminated in 6 weeks. They examined parameters that could affect radiolabeling such as particle concentration, pH, temperature, and incubation time.

S. Research Goals

A positron-emitting surrogate particle for the Y-90 microspheres was developed such that the new surrogate particle was stable in vivo and had a size distribution closer to Y-90 microspheres than Tc-99m MAA. The new surrogate particle was designed for imaging using PET which is superior to SPECT for quantitative imaging. Pre-treatment PET data was used with a Monte Carlo simulation program to perform accurate pre-treatment dosimetry. Calculated Y-90 doses were confirmed with actual measurements using beta dosimetry. The research goal in this dissertation can be divided into two aims, the development of a positron emitting microsphere and the demonstration of dosimetry that utilizes PET imaging.

1. Aim 1: Positron Microsphere Development

A microsphere was labeled with a positron-emitting radionuclide to create a surrogate for Y-90 microspheres. The size of the surrogate was matched to the size of the Y-90 microspheres. The surrogate microsphere and radiolabel were selected such that the radiolabeling process was relatively simple. The microsphere and positron-emitting label were selected such that the materials are easy to acquire and non-toxic.

In vitro testing of the radiolabeled microspheres was performed in the presence of blood products to assess the binding of the radiolabel to the microsphere. Unlike Tc-99m MAA, the degradation of the surrogate particle did not become significant in the period that imaging occurs.

A relatively small amount of PET microspheres were needed to provide enough positrons to produce useful activity distributions with PET. Keeping the number of microspheres to a minimum help avoid embolic effects such as stasis and reflux.

In vivo testing of the surrogate microspheres involved administration into an animal. The radiolabel was sufficiently bound such that activity was not removed from the surrogate microsphere by blood flow or other physiologic processes. Whole body PET imaging of the animal was used to assess removal of the positron emitting radiolabel from the microspheres. This was a preliminary test required before human use is considered.

2. Aim 2: Dosimetry

The goal was to demonstrate that PET imaging of the surrogate microsphere distribution can be used to calculate the absorbed dose distribution due to Y-90 microspheres

A phantom containing the surrogate radionuclide was imaged with PET. The PET data was used to create a voxelized source in a Monte Carlo simulation.

The activity of Y-90 during the PET acquisition can be calculated based on the initial activities of the surrogate radionuclide and Y-90. The majority of absorbed dose to a region of interest is due to the beta electrons from Y-90. The absorbed dose in a region of interest was calculated with the Monte Carlo simulation. The actual dose to the same region of interest was measured with beta dosimetry. The beta dosimetry was performed with radiochromic film and a calibrated source of electrons

II. Surrogate Microsphere Development

A. Radiolabeling

1. Introduction

The purpose of these experiments was to investigate the process of radiolabeling hydroxyapatite microspheres with fluorine-18. A variety of labeling conditions were investigated such as initial activity concentration, activity per mass, pH, and form of hydroxyapatite. These experiments were designed as a broad parametric survey.

Other investigators have demonstrated significant adsorption of F-18 on to hydroxyapatite[39], [45], [50]. For instance, calculations indicate that Fan et al. were able to bind an estimated $5x10^{13}$ molecules of fluoride per gram of hydroxyapatite. This is equivalent to 142 mCi of F-18 per gram of hydroxyapatite. These experiments were to determine if it was possible to bind mCi amounts of F-18 to milligrams of ceramic hydroxyapatite microspheres. The binding of F-18 to the microspheres was expected to similar to follow a trend similar to that shown in Fan et al., Figure 1 [45]. In this figure, the adsorption increases rapidly and the percent adsorption reaches 80% within 50 minutes. The adsorption continues to increase and is nearly 100% at 150 minutes past the time at which the F-18 was added to the hydroxyapatite.

A method used to monitor the adsorption of the F-18 fluoride ion onto the hydroxyapatite was to sample the liquid supernatant surrounding the microspheres. As the F-18 binds to the microspheres, the amount of F-18 in the supernatant will decrease. The rate of F-18 removal from the supernatant follows the rate of adsorption on to the hydroxyapatite microspheres.

2. Methods

Radiolabeling was performed with F-18 sodium fluoride, [F-18] NaF, supplied as a unit dose by PETNET Solutions Inc., a subsidiary of Siemens Medical Solutions USA, Inc. The F-18 sodium fluoride provided by PETNET is their "injectable" form and is FDA approved for injection into humans. The PETNET F-18 sodium fluoride for injections is a clear, colorless, pyrogen-free, preservative-free, isotonic aqueous solution of 0.9% sodium chloride. The solution activity is between 10 mCi to 200 mCi per mL.

The solution pH is between 4.5 and 8 [53]. The [F-18] NaF unit dose was produced at a PETNET cyclotron facility and delivered the day of the experiment.

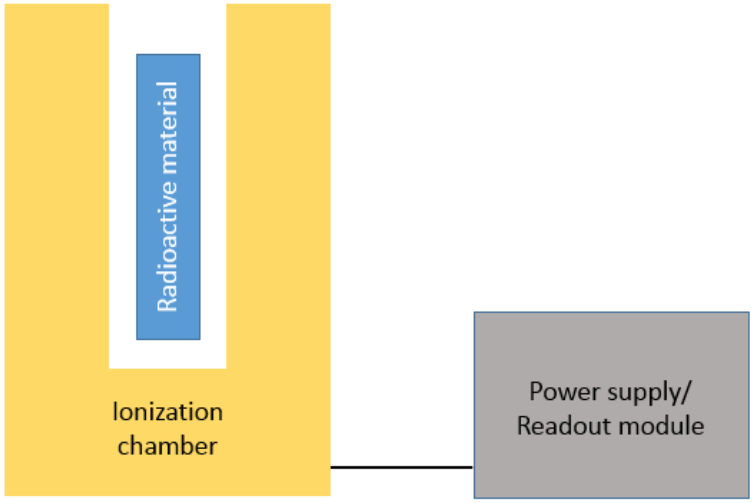

Figure 6: Schematic of dose calibrator with cut-away view of ionization chamber with well geometry.

The dose calibrator used during the radiolabeling experiments was a Capintec CRC-7R, serial number 70723. A dose calibrator is an ionization chamber with a well-type geometry. Commercial dose calibrators are able to accurately measure the activity of a radioactive sample over six or more orders of magnitude. The activity range that was measured in the dose calibrator during the radiolabeling experiments was approximately 0.01 µCi to 20 mCi.

Figure 7: Shown is the dose calibrator used in these experiments. The readout module has the LED digits, range buttons and potentiometers for adjustment. The ionization chamber is the cylinder on the right side of photo.

Figure 8: Calibration source for F-18 in a dose calibrator dipper. The dipper is partially in the well of the dose calibrator ionization chamber. The source is NIST-traceable with a known activity of Ge-68/Ga-68. Gallium-68 is a positron emitter. The Ga-68 activity is converted into NIST-traceable activity for F-18.

Prior to the labeling experiments, the dose calibrator was calibrated for F-18 using a Ge-68/Ga-68 calibration source. The calibration source is a model BM06S Positron Reference Standard manufactured by RadQual LLC. The source contains Ge-68 and Ga-68 uniformly distributed in 3 milliliters of colored epoxy. The Ge-68 decays to Ga-68. The daughter nuclide, Ga-68, is in secular equilibrium with the parent nuclide, Ge-68. The value of the Ge-68 half-life used in the source certificate was 270.8 days. A copy of the source certificate is in Appendix A. The daughter nuclide, Ga-68, is a positron emitter with a half-life of 67.7 minutes [35]. The value on the source certificate for the

Gallium-68 percent abundance for 511 keV photons is 178.2%. The source is NIST traceable with a declared uncertainty of 1.15% with a 95% confidence level. The vendor provides a "Decay Reference Calendar" in which the Ga-68 activity and F-18 activity on a given date are listed. The percent abundance of F-18 for 511 keV photons is 193.5% [35]. The Ga-68 activity is scaled by the percent abundances to produce an equivalent F-18 activity. The apparent F-18 activity is used to calibrate the dose calibrator for F-18.

The process to check a dose calibrator for accuracy of fluorine-18 measurements was relatively straightforward. The calibration source was placed into the same geometry used to measure F-18 samples and the F-18 channel was selected. The displayed activity was compared to the expected F-18 activity. The calibration potentiometer was adjusted until the displayed activity matched the expected activity for the F-18 channel and Ge-68/Ga-68 source. In this instance, the calibration number that resulted in the best agreement was 488. This calibration number was used in all subsequent radiolabeling experiments.

The expected activity was calculated by extending the Decay Reference Calendar beyond the vendor published values. This was done by decay-correcting the activity using the 270.8 day half-life of Ge-68.

Figure 9: PerkinElmer "Wizard^{2}" model 2480 automatic gamma counter.

Many of the samples measured in the dose calibrator were also measured in an automated NaI(Tl) detector system. The system was a Wizard^{2} gamma counter model 2480 manufactured by PerkinElmer, serial number DG04129132. The system was calibrated for F-18 measurements using a small amount of F-18 per instructions provided by the vendor. In the first two radiolabeling experimental runs, 25 µL aliquots were used. During the remaining radiolabeling experiments, the aliquot size was 50 µL. At the conclusion of each labeling experimental run, all of the aliquot samples were placed into a rack. The Wizard^{2} sample counter was used to perform automated reading of counts from the samples.

An effort was made to keep variations in the dose calibrator readings due to geometric effects and the effects of containers to a minimum. During any given experimental run, there were three types of containers used. The 3 mL syringe that

PETNET used for the unit dose, the 15 mL polypropylene centrifuge containers, and the PerkinElmer vials used in the PerkinElmer Wizard[2] automated sample counting system.

Figure 10: Shown is 3 mL syringe with needle used by PETNET to deliver F-18 sodium fluoride unit dose.

Figure 11: Two different models of 15 mL polypropylene centrifuge tubes used in these radiolabeling experiments.

Figure 12: PerkinElmer sample vial (left). Vials in rack ready for counting in Wizard^2 counting system.

Geometric effects with the PerkinElmer vials were not significant. The aliquots were always the same volume. In any given experiment run, the amount of liquid in the PerkinElmer Wizard^2 containers remained constant. Usually this was 50 mL. Care was taken to ensure that the PerkinElmer vials were measured in the same location in the dose calibrator.

The volume of the unit dose delivered by PETNET in the 3 mL syringe varied between 0.5 mL and 2.5 mL. The volume was adjusted by pulling liquid into the syringe. The type of liquid used to adjust depended on the particular experiment. In early experiment, de-ionized water was used. In later experiments, phosphate buffered saline (PBS) was often used. The final volume of the adjusted unit dose was between 2.5 and 3.1 mL. Once the desired volume was achieved, the activity in the syringe was measured in the dose calibrator. A single measurement was recorded for the final volume of liquid in the syringe. The variation in the dose calibrator measurements due to geometric effects of different dose volumes is plotted in Figure 13. The percent difference in the 2.5 to 3.1 mL range is approximately 0.5%.

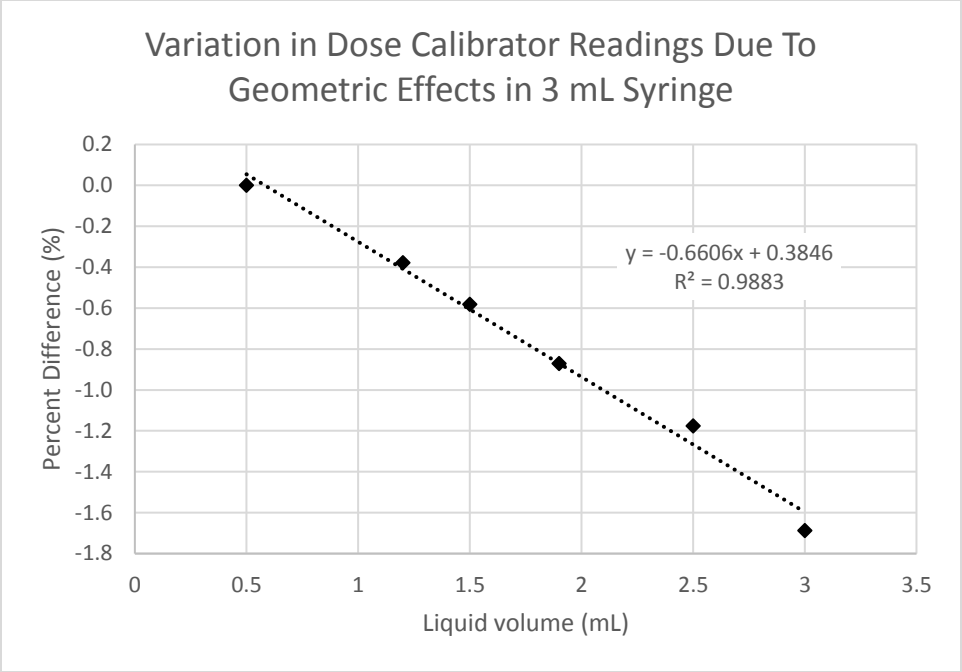

Figure 13: Variation in dose calibrator readings due to geometric variation in 3 mL syringe. Data has been normalized to a volume of 0.5 mL.

In any given experiment run, the amount of liquid in the centrifuge tubes could vary. Geometric effects in the centrifuge tube were measured. A 0.6 mL sample containing F-18 was placed in a centrifuge tube and the activity was measured and time recorded. An autopipette was used to add 1 mL of de-ionized water. The activity was measured and the time recorded. The activity was increased in 1 mL increments to a volume of 13.6 mL. With the data normalized to 0.6 mL, the maximum deviation of 1.81% occurred at 12.6 mL. The results are plotted in Figure 14. In most instances, the volume change over an entire experiment run would vary from approximately 0.5 mL to 5 mL. This would likely result in an approximate error of +/- 0.5% from geometric effects.

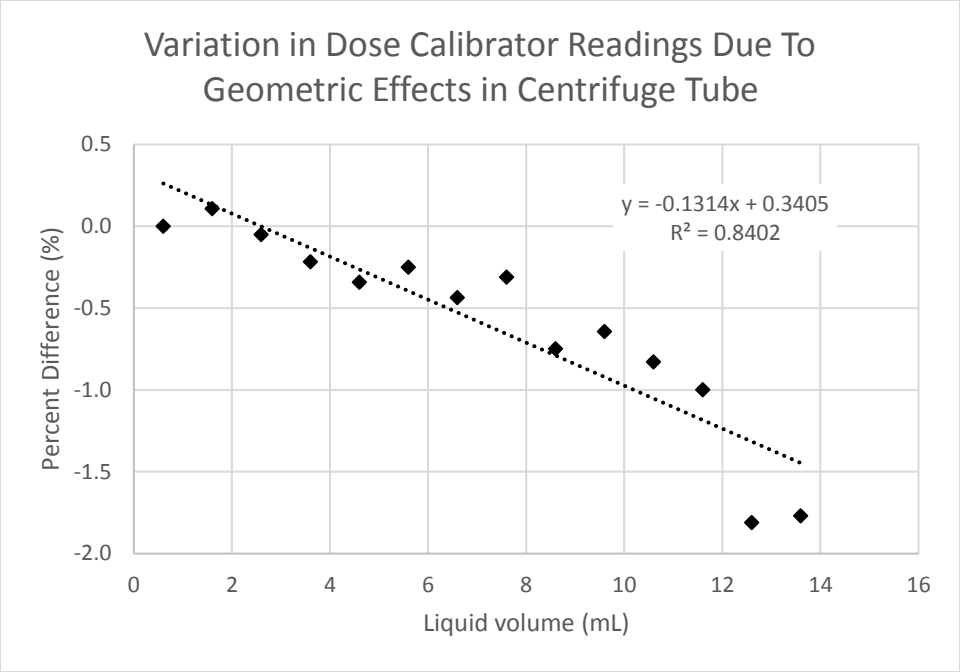

Figure 14: Variation in dose calibrator readings with different volumes of liquid in centrifuge tube. Data was normalized to 0.6 mL reading.

There may have been effects going from one container type to another. The activity variation between the 3 mL syringe and the centrifuge tube was measured. An activity of 1.618 mCi in 0.5 mL was measured in the 3 mL syringe. This was injected into a centrifuge tube. The residual activity in the syringe and the activity in the centrifuge tube were measured and corrected for decay. An activity discrepancy of 0.47% was measured between the 3 mL syringe and the centrifuge tube.

The linearity when switching between activity scales on the dose calibrator was checked. A source was measured on the 20 mCi scale and then on the 2000 µCi scale. A difference of 7.45% was measured. The round-off error on the 20 mCi scale contributes to this difference. On the 20 mCi scale, only two digits to the right of the decimal are displayed, whereas more are displayed on the 2000 µCi scale. A source was also

measured with the dose calibrator on the 2000 µCi scale and then the 200 µCi scale. A difference of 1.1 % was found for the measured activity of the same source. The test was repeated for the 200 µCi scale and 20 µCi scale. A source was measured with the dose calibrator on the 200 µCi scale and then the 20 µCi scale. A difference of 0.03 % was found for the measured activity of the same source.

In many measurements and subsequent calculations, the dose calibrator accuracy was not critical since the final calculation was a ratio of the activities measured. Thus, relative activity was important, not the absolute activity. In general, for the dose calibrator measurements, the estimated uncertainty was low. Another method to estimate the uncertainty of the dose calibrator measurements was to compare the data to the Wizard^2 data. The count data from the Wizard^2 enabled calculation of uncertainty based on counting statistics.

The hydroxyapatite was in the form of ceramic microspheres purchased from Bio-Rad Laboratories, Inc. and marketed as CHT™ ceramic hydroxyapatite particles. The microspheres are available in 20 µm, 40 µm and 80 µm diameters. The microspheres used in these radiolabeling experiments were 20 um in diameter. The volume of a single microsphere is 4.2×10^{-9} cubic cm. The volume of 1 million microspheres is 4.2×10^{-3} cubic cm. The density in a packed bed of CHT 20 µm microspheres is 0.63 g/mL. The packing density for a packed bed of spheres was assumed to be 63%. The density of the hydroxyapatite microsphere is approximately 1 g/mL. Thus, the mass of 1 million of the 20 um-diameter microspheres is 4.2 mg. The number of microspheres per unit mass is 2.4×10^{5} per mg. The CHT microspheres are available in two types, Type I and Type II. According to the vendor's literature, Type I has a smaller pore diameter (600-800

angstroms) compared to Type II (800-1000 angstroms) [54]. The lot number for Type I was S401021. The lot number for Type II was S700928. Both types of CHT microspheres were used.

Prior to labeling, the dry hydroxyapatite was measured with an analytical balance. The balance was a Mettler-Toledo AB-S/FACT, serial number 1128042661. This analytical balance has a 0.1 mg resolution. The most commonly used containers for mixing hydroxyapatite and F-18 sodium fluoride were 15 mL polypropylene centrifuge tubes. To begin weighing the microspheres, a 15 mL centrifuge tube was placed on the analytical balance. The balance reading was set to zero milligrams. A small amount of hydroxyapatite was then added to the centrifuge tube and the mass of the hydroxyapatite was measured. Material was added until the desired mass of hydroxyapatite was reached.

In the first experiment, the mass of hydroxyapatite was 102.6 mg. Subsequent experiments, the mass of hydroxyapatite was much less. The range of masses for subsequent radiolabeling experiments was 4.0 mg to 10.5 mg.

The typical volume of the unit dose delivered by PETNET was 0.5 mL to 2 mL of F-18 sodium fluoride in a 3 mL syringe. Usually the volume was adjusted by adding saline, deionized water or phosphate buffered saline (PBS). In one run, sodium citrate dehydrate (EMD Millipore, Inc.) was used to prepare 500 millimolar solution of sodium citrate buffer. The goal was to see if the citrate had any effect on adsorption or disassociation of the F-18.

Once the desired volume was achieved, the activity of the unit dose of sodium fluoride was measured in the dose calibrator. The volume of the unit dose was recorded. When the desired activity and volume was reached, a small volume of the [F-18] NaF

liquid was removed for measurement of the pH. A second sample of the liquid was removed. This sample was usually a fixed volume of 50 µL removed with an autopipette. The time that this aliquot was removed from the liquid was recorded. This sample was usually designated "aliquot 1". The activity concentration in aliquot 1 (µCi/mL) was the same as the activity concentration of the bulk [F-18] NaF liquid. The rate of radioactive decay in the [F-18] NaF liquid and in aliquot 1 was always the same. For any subsequent times, the activity concentration of aliquot 1 would always be same as the activity concentration of the [F-18] NaF unit dose prior to the addition of the unit dose to the hydroxyapatite microspheres. The activity concentration of the bulk [F-18] NaF liquid prior to the addition of hydroxyapatite was an important measurement for adsorption rate calculations.

Prior to adding the F-18 sodium fluoride to the hydroxyapatite, a small sample of the liquid was removed. This sample was used for measurement of the pH. The pH the F-18 sodium fluoride was measured using BAKER-pHIX pH test strips. The test strips are sensitive to a specific pH range. Type 4394-01 was used to measure in the pH range 3.6 to 6.1. Type 4396-01 was used to measure a pH range of 6.0 to 7.7. Type 4398-01 was used to measure pH in the 7.5 to 9.5 range. At the beginning of this study, the accuracy of the strips was checked with pH calibration solutions of known pH.

Figure 15: Test strips for pH measurement

The pH of the unit dose delivered by PETNET was usually found to be in the range of 5.6 to 6.1. In the early radiolabeling experiments, the [F-18] NaF solution used to radiolabel the hydroxyapatite was also in the acidic range of 5.6 to 6.1. The radiolabeling results produced with these solutions were very good. However, there was concern that the slightly acidic solution was increasing the rate of disassociation during the washing phase of the experiment. CHT hydroxyapatite is designed for use in protein purification. A "Golden Rule" stated by Bio-Rad in bulletin 6932 is to keep the pH> 6.5 throughout the purification process. In light of the recommendation from Bio-Rad, the pH of subsequent [F-18] NaF solutions were adjusted with PBS buffer to be greater than a pH of 6.5.

After the removal of the first aliquot and pH sample, the [F-18] NaF solution was added to the CHT hydroxyapatite microspheres. The F-18 sodium fluoride was injected

into the centrifuge tube containing the hydroxyapatite microspheres. The injection time was recorded. After injection, the residual activity in the 3mL syringe was measured and the time recorded. The material was mixed by shaking the vial until the particles were suspended in the fluid. In early trials, the mixture was placed on a rocker for one minute. It was found that the binding of F-18 to the microspheres was very rapid. After the first few experimental runs, the rocking step was skipped in order to get more aliquots of the supernatant. In these instances, the mixture was shaken by hand until the hydroxyapatite microspheres were in suspension and then the tube was placed in the centrifuge.

It was found that 2500 RPM for 1 minute was sufficient to force the microspheres into a pellet. The centrifuge was not absolutely necessary but did speed the separation of the microspheres from the supernatant. The uptake was usually so rapid that to gather multiple data points during the adsorption process, the centrifuge was needed to rapidly separate the mixture. After the hydroxyapatite was centrifuged into a pellet, a 50 µL aliquot of the supernatant was withdrawn. The time that the aliquot was removed from the supernatant was recorded. The aliquot of supernatant was measured in the dose calibrator. The time and activity of the aliquot were recorded. The aliquot was set aside for later measurement in the automated sample counter. The sodium fluoride and hydroxyapatite mixture was then shaken until the microsphere pellet was dissolved and the microspheres were resuspended in the fluid. The mixture was then centrifuged again. The cycle of shaking, centrifuging, aliquot removal, and activity measurement continued until the activity of the aliquots appeared to plateau.

To maintain the same measurement geometry, care was taken to ensure that all aliquots were measured at the same position within the dose calibrator. All aliquots were

measured in the dose calibrator, labeled and set aside. Towards the end of the experiment run, the aliquots were placed in racks and counted with the Wizard^2 automated sample counter.

When an aliquot is removed from the supernatant, the activity concentration ceases to be influenced by adsorption on the hydroxyapatite. After removal, the only factor influencing the activity concentration is radioactive decay. The time of removal was recorded for each aliquot. Thus, it was possible to correct the measured activity in an aliquot for radioactive decay. In this way, the activity concentration of the supernatant was sampled over time.

A concern was the possible binding of F-18 to the polypropylene centrifuge tubes. This was investigated during the labeling experiment performed on 9/12/2017. The hydroxyapatite and sodium fluoride had been mixed in a polypropylene centrifuge tube. After the radiolabeling phase of the experiment was complete, the centrifuge tube containing the hydroxyapatite and remaining supernatant was measured in the dose calibrator. The measured activity was 7.60 mCi. The mixture was then transferred to a glass tube. The polypropylene centrifuge tube was rinsed with 6 mL of de-ionized water. The rinse water was added to the hydroxyapatite mixture in the glass tube. After rinsing, the remaining activity of the centrifuge tube was measured with the dose calibrator. The decay-corrected activity of the centrifuge tube was 45.3 µCi. This activity is 0.6% of the mixture activity. The glass tube containing the hydroxyapatite, supernatant and rinse water was measured. The decay corrected activity was 7.53 mCi. There was a 25 µCi discrepancy in the activity accounting. This represents 0.3% of the initial activity. The slight difference in activity measurements was likely due to difference in volumes and

container materials affecting the dose calibrator measurements. The initial measurement was done with the mixture in polypropylene with a liquid volume of 0.8 mL. The second measurement was done with the mixture in glass with a volume of 6.8 mL. The conclusion was that the binding of F-18 to the polypropylene centrifuge tubes was not significant.

Another potential source of error was the possibility that during removal of the aliquots, a small amounts of microspheres were being collected by the pipet. This was especially a concern when the volume of the supernatant was low and the pipet tip was close to the hydroxyapatite pellet. The method used to check for the inadvertent pick up of microspheres was to take two aliquots of identical volume. One was taken from the top of the supernatant, far from the pellet. The other aliquot was taken from the remaining supernatant near the hydroxyapatite pellet. If microspheres were still in suspension or were being removed from the pellet due to agitation, then the microsphere concentration would likely be greater in the aliquot taken near the pellet. If this were the case, the second aliquot would likely have a greater activity than the first aliquot. This method was used in several instances. As an example, on 9-12-2017 after the radiolabeling phase of the experiment was complete, the mixture was centrifuged at 4000 rpm for 3 minutes. Afterwards, 1 mL of supernatant was removed and labeled "super 1". Another 1 mL of supernatant was removed and labeled "super 2". The second supernatant sample was drawn much closer to the hydroxyapatite pellet. If microspheres were being drawn into the pipet, the second sample was expected to have a greater activity than the first sample. The decay-corrected activities of "super 1" was 17.9 µCi and 17.6 µCi for "super 2". The second activity was actually slightly less than the first.

This method is likely to be sensitive to a difference of a few microcuries. In this instance, a 1 µCi amount of microspheres represents 0.0013% of the total activity bound to the microspheres.

Below is a summary of the uncertainties that may have contributed to measurement error during these experiments. Each uncertainty listed in the table, may or may not have been applicable, depending on the specific circumstances of the experiment.

Table 1: Sources of measurement uncertainties

Measurement	**Uncertainty**
Dose calibrator accuracy	1.15%
Dose calibrator geometric variation in centrifuge tube	0.5%
Resolution of dose calibrator	0.01 µCi
Linearity between activity range 20 mCi and 2000 µCi scale.	7.45%
Linearity between activity range 2000 µCi and 200 µCi scale	1.1%
Linearity between activity range 200 µCi and 20 µCi scale	0.03%
Resolution of analytic balance	0.1 mg

3. Results

Eight radiolabeling runs were performed. For these experiments, the fraction of initial activity in the supernatant over time is shown in Figure 16. The activities shown in Figure 16 were measured in the Capintec CRC-7 dose calibrator. All activities were corrected for radioactive decay. The units along the horizontal axis are minutes since the [F-18] NaF was added to the hydroxyapatite microspheres. In Figure 16, the time when the F-18 sodium fluoride was added to the hydroxyapatite was designated as time = 0.

As the F-18 was binding to the hydroxyapatite, the activity concentration of the supernatant was decreasing. Overall the binding was rapid. In most instances 90% of the activity was removed from the supernatant within the first 10 minutes.

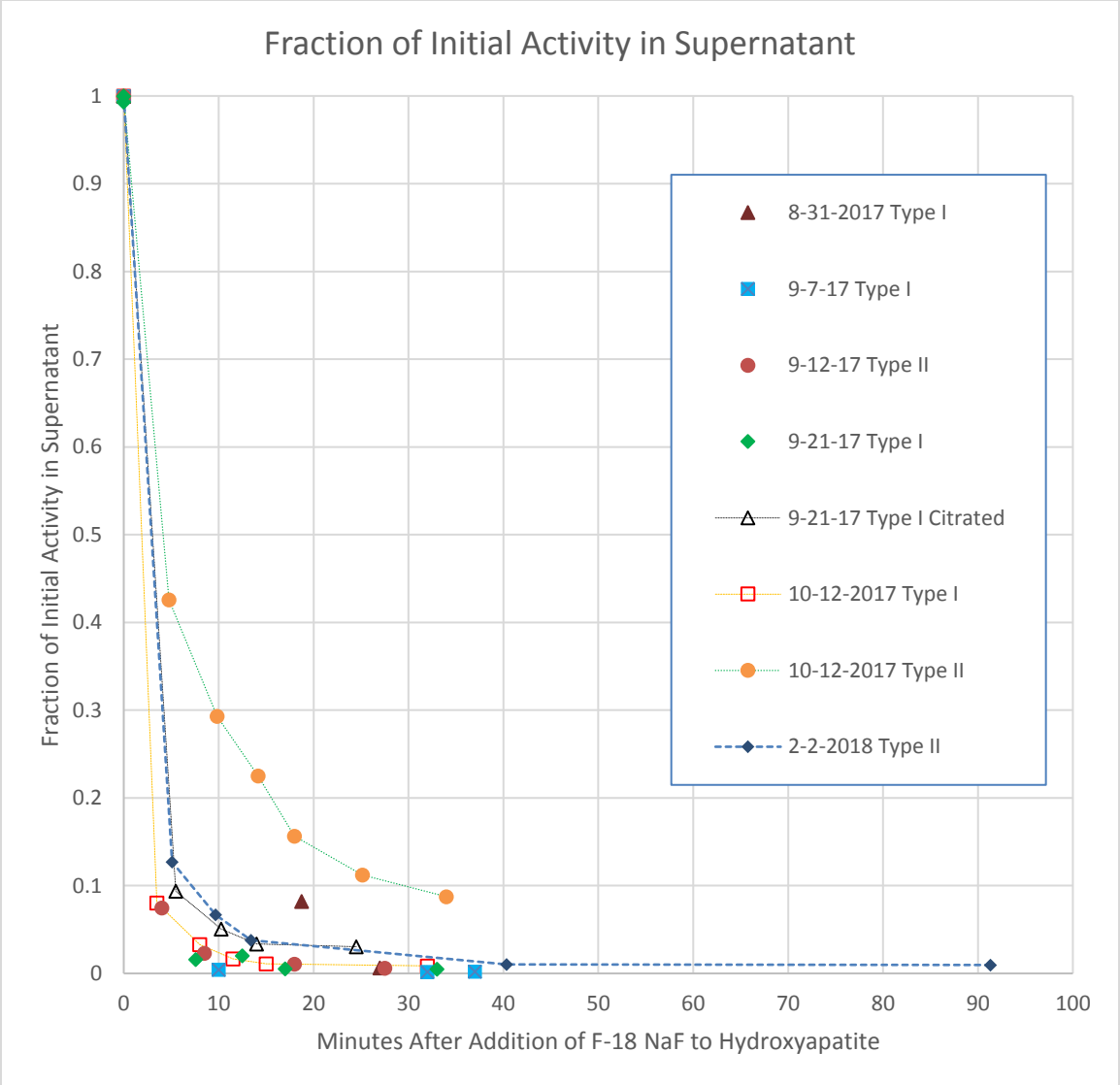

Figure 16: Fraction of initial activity in supernatant plotted at the time points when the aliquots were removed from the supernatant. All activities have been corrected for radioactive decay. The activity measurements were performed with the dose calibrator.

The results from the 10-12-2017 run with Type II microspheres show that the binding was much slower than in other experimental runs. It does appear that given enough time, the activity in the supernatant would have plateaued in the sub-five percent range. The cause of this slow binding is unknown. It is unlikely that the unit dose was contaminated. The unit dose from PETNET was split. The radiolabeling done with the first half-dose had results similar to other results. These results are plotted as "10-12-2017 Type I" in Figure 16. After examination, the current belief is that the wrong concentration of PBS was used in the 10-12-2017 Type II radiolabeling experiment. The supply of PBS used for radiolabeling and washing was occasionally resupplied from a larger bottle of PBS (Gibco 1x). There was a bottle of Gibco 10x concentrated PBS in the lab at the time. The labels look very similar. It is possible that the 10x strength was used inadvertently. Another possibility investigated was detector error. For all experiment runs, the aliquots were measured in the dose calibrator and then later measured in the Wizard^2 sample counter.

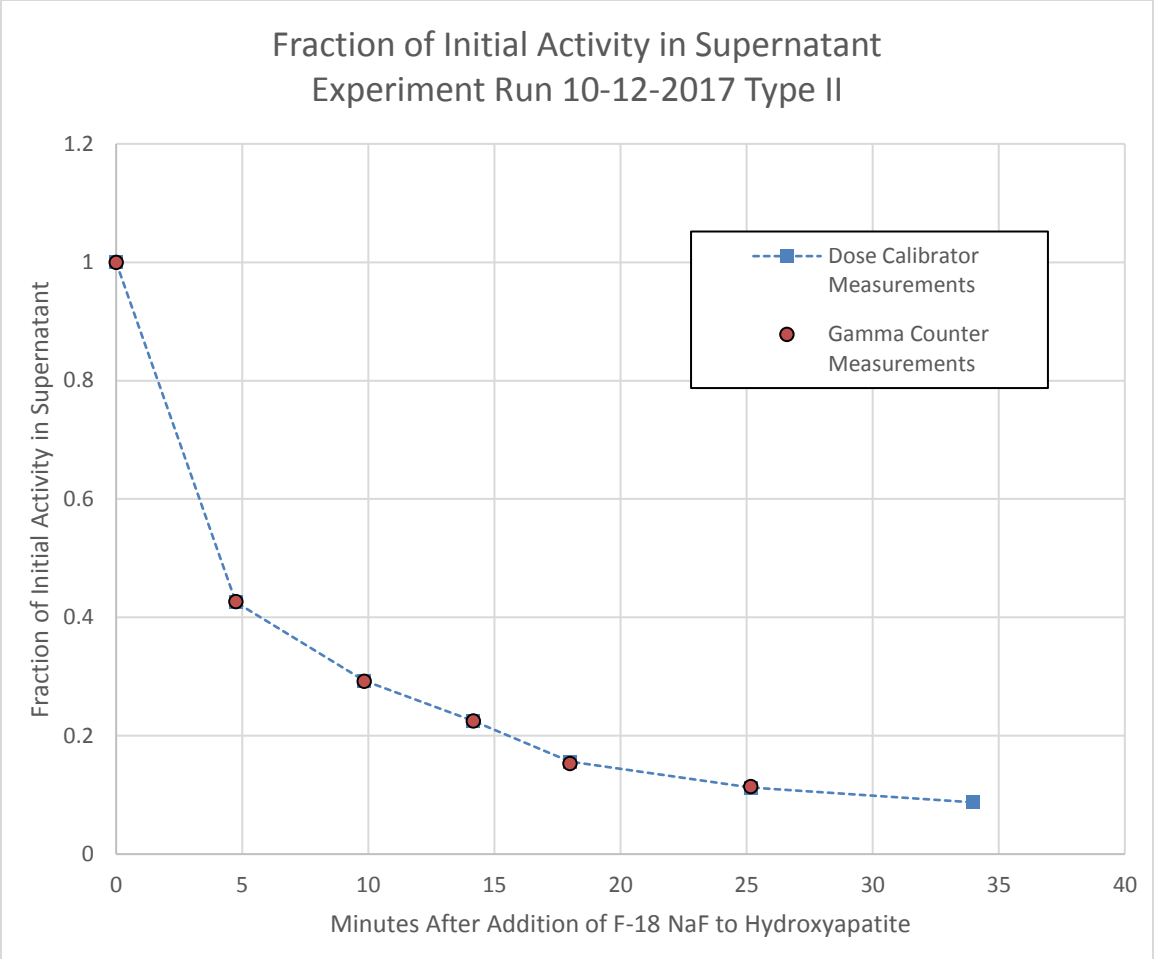

Figure 17: Fraction of initial activity in supernatant as measured by Capintec dose calibrator and Wizard[2] sample counter. The largest uncertainty due to counting statistics for the Wizard[2] data was 0.158%.

Figure 17 is a plot of the data from the 10-12-2017 run with Type II microspheres. Plotted in this figure are the results from the dose calibrator and the Wizard[2] sample counter. The data from the Wizard[2] sample counter closely matches the measurements from the dose calibrator. The sample counter results are in the form of number of counts from a sample. Counting statistics were applied to this data. For the aliquot that was initially removed, prior to the addition to hydroxyapatite, the count rate was 4,011,842 cpm. The rate was corrected for dead time and background counts were subtracted. The

next aliquot was removed from the supernatant 4.75 minutes after the addition of the [F-18 NaF liquid to the hydroxyapatite. The count rate for this aliquot measured 1,711,411 cpm. This was also corrected for dead time and background counts were subtracted. Subsequent aliquot count rates were decay-corrected to the beginning of the assay. The ratio of the two count rates is 0.4266. Based on counting statistics associated uncertainty for the ratio of the two count rates is 0.094%. The largest uncertainty due to counting statistics for the six measurements obtained with the sample counter was 0.158% for the last aliquot removed from the supernatant.

In general, statistical uncertainty for the Wizard^2 data was low and closely matched the dose calibrator measurements. The following graphs are plots of the fraction of initial activity in the supernatant as calculated using the CRC-7 dose calibrator data and the data from the Wizard^2 gamma counter. The gamma counter data was in the form of counts. Standard methods of error propagation were applied to calculate the uncertainty based on the counting statistics.

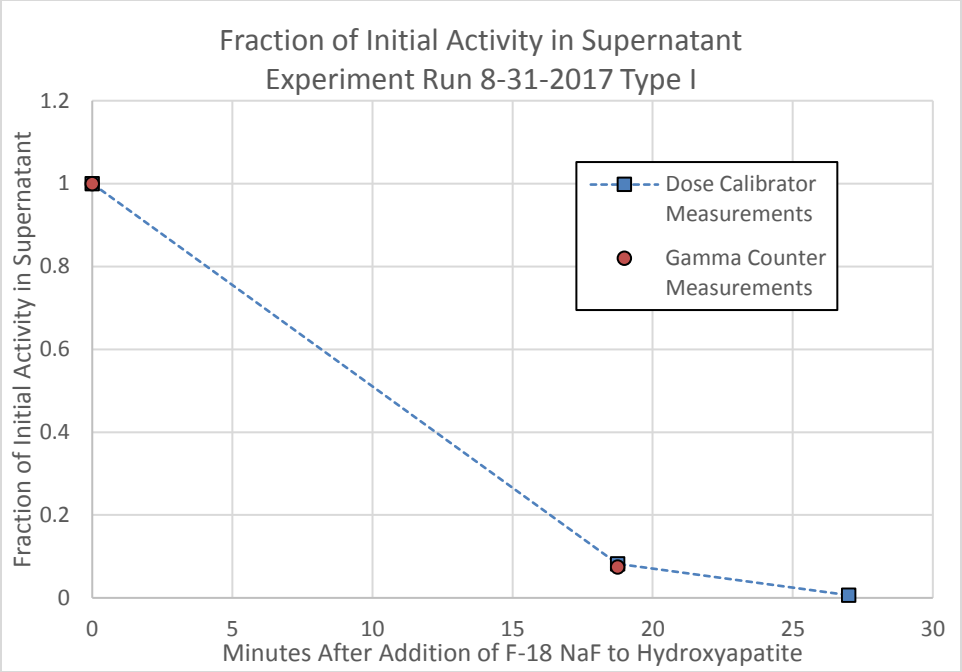

Figure 18: Fraction of initial activity based on dose calibrator measurements and gamma counter measurements. The largest uncertainty due to counting statistics was 0.534%

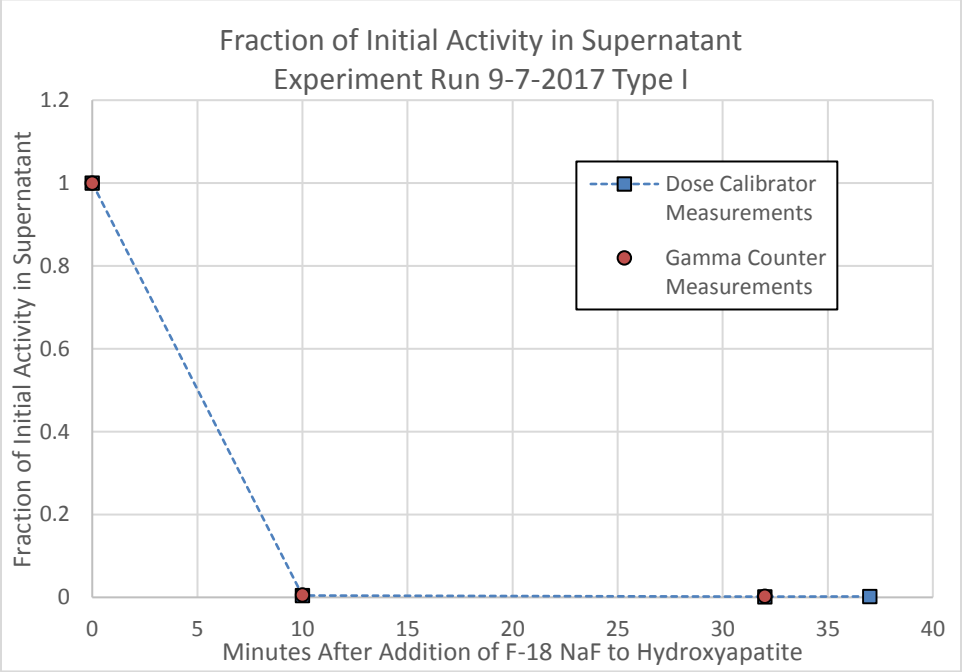

Figure 19: Fraction of initial activity based on dose calibrator measurements and gamma counter measurements. The largest uncertainty due to counting statistics was 0.561%

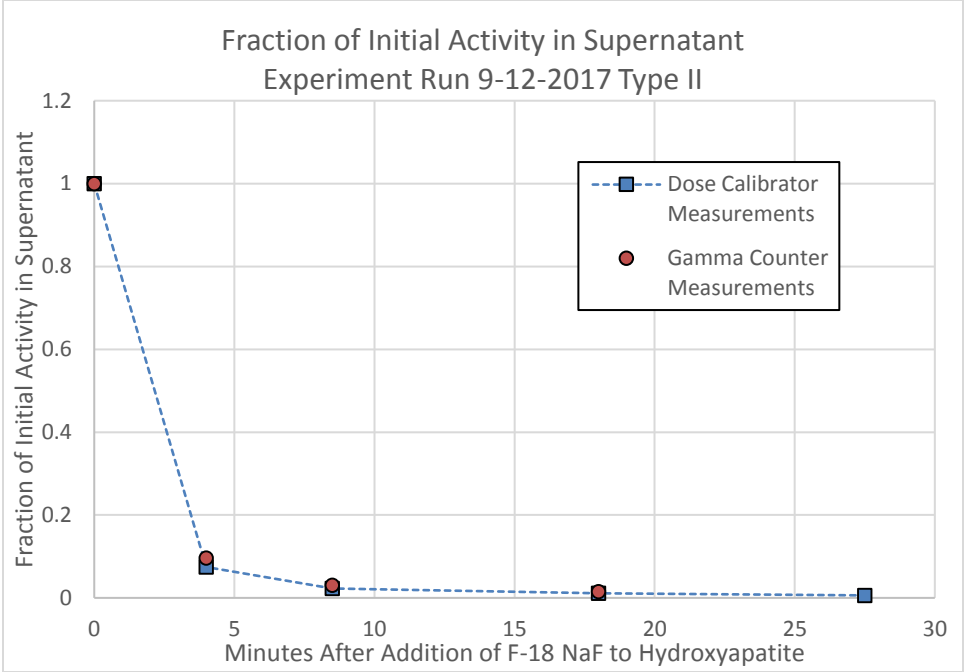

Figure 20: Run 9-12-2017. The largest uncertainty due to counting statistics was 0.242%

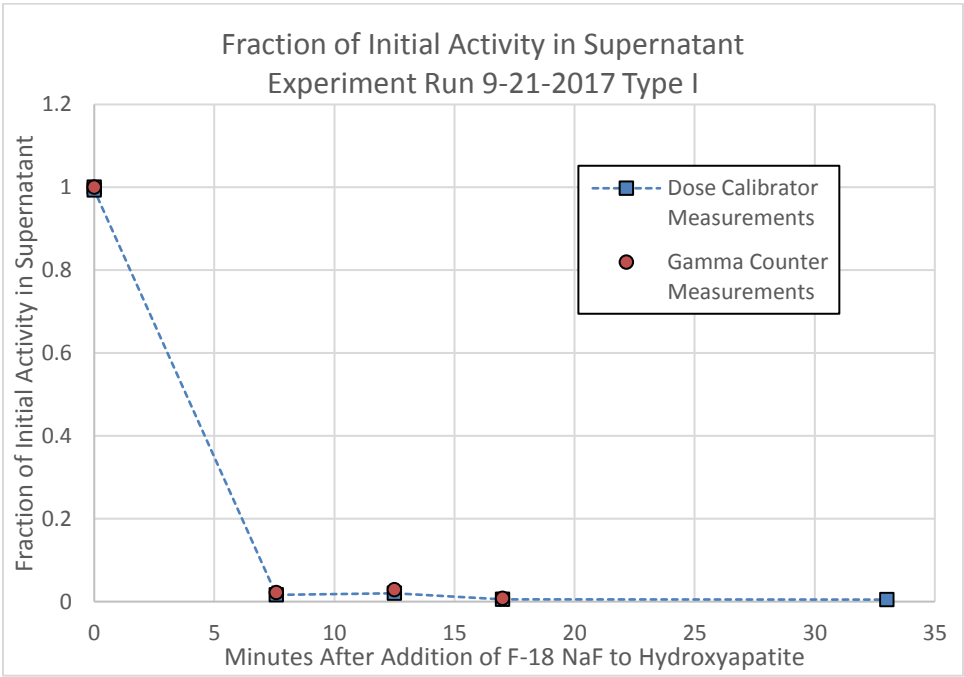

Figure 21: Run 9-21-2017. The largest uncertainty due to counting statistics was 0.552%

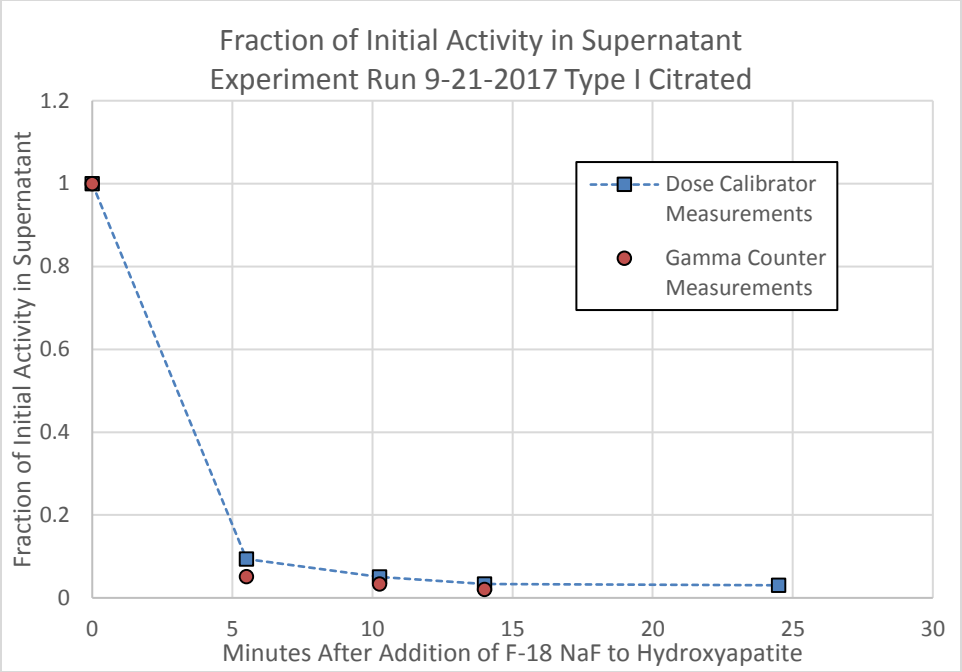

Figure 22: Run 9-21-2017 Citrated. The largest uncertainty due to counting statistics was 0.334%

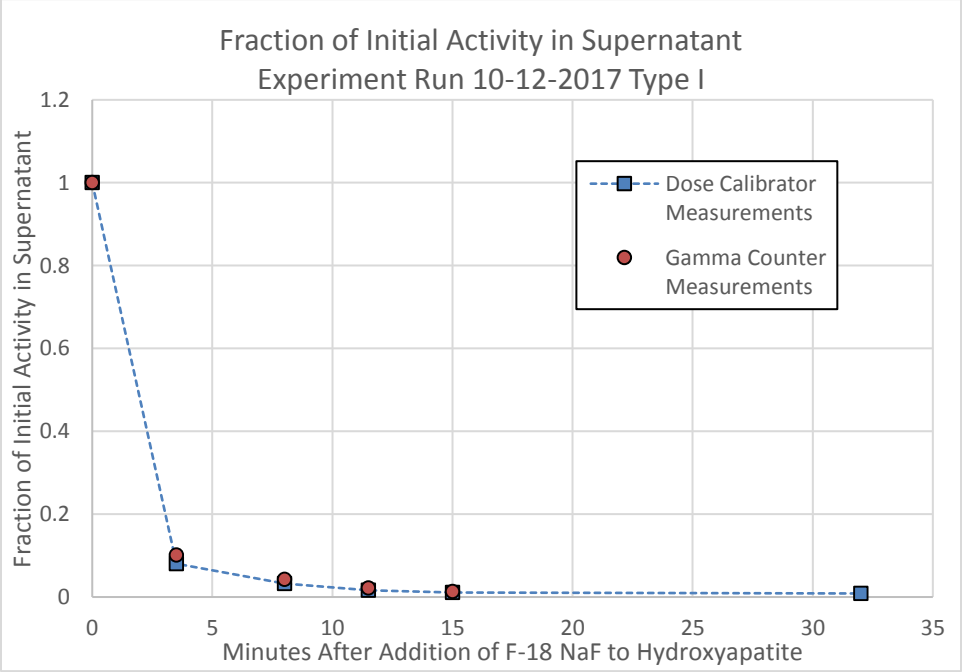

Figure 23: Run 10-12-2017 with Type I microspheres. The largest uncertainty due to counting statistics was 0.483%

The following table lists the parameters and results of each radiolabeling experimental run.

Table 2: Results of Radiolabeling Experiments

Date of Experiment Run	**8/29/17**	**8/31/17**	**9/7/17**	**9/12/17**	**9/21/17**	**9/21/17**	**10/12/17**	**10/12/17**	**2/2/18**
Microsphere Type	**I**	**I**	**I**	**II**	**I**	**I**	**I**	**II**	**II**
Initial microsphere preparation	**none**	**none**	**none**	**none**	**none**	**citrate**	**none**	**none**	**none**
Material to adjust unit dose	**D.I. H_20 or 0.9% saline**	**D.I. H_20 or 0.9% saline**	**D.I. H_20 or 0.9% saline**	**D.I. H_20 or 0.9% saline**	**PBS**	**PBS**	**PBS**	**PBS**	**PBS**
pH at time of NaF + hydroxyapatite	**5.5-6.0**	**5.6-6.1**	**5.6-6.1**	**5.6-6.1**	**7.0-7.3**	**6.7-7.0**	**6.7-7.0**	**6.7-7.0**	**7.4**
Initial mass of hydroxyapatite (mg)	**102.6**	**7.4**	**9.4**	**7.8**	**4.0**	**10.5**	**3.5**	**2.7**	**6.9**
Initial activity (mCi)	**6.54**	**12.15**	**10.65**	**9.42**	**4.38**	**2.03**	**6.15**	**2.23**	**4.71**
Initial volume of unit dose (mL)	**3.0**	**2.8**	**3.1**	**2.8**	**2.5**	**2.5**	**2.4**	**3.0**	**8.0**
Initial concentration of F-18 NaF (mCi/mL)	**2.18**	**4.34**	**3.44**	**3.36**	**1.75**	**0.50**	**2.56**	**0.74**	**0.59**
Initial activity per mass (mCi/mg)	**0.06**	**1.64**	**1.13**	**1.21**	**1.10**	**0.19**	**1.76**	**0.83**	**0.68**
Minimum radiolabeling efficiency %	**99.8**	**99.5**	**99.7**	**99.2**	**99.4**	**97.0**	**98.8**	**88.4**	**96.1**

The microspheres were either Type I or Type II. In most radiolabeling experiments Type I was used. There was little difference in radiolabeling performance.

The outlier data set from 10/12/17 occurred with Type II microspheres. Whether the microsphere type was a factor in the slow rate of adsorption is not known.

Data regarding the pH of the initial solution was acquired. In early radiolabeling experiments, the unit dose volume was adjusted with de-ionized water or 0.9% NaCl saline. This pH was measured with test strips and was in the range 5.5 to 6.1. The effect of pH on the labeling rate and labeling efficiency was a question of concern. In addition, there was suspicion that the rate of disassociation of the radiolabel was being influenced by the pH during labeling. Further investigation found that the manufacturer of the hydroxyapatite, Bio-Rad, recommended a pH greater than 6.5. For subsequent radiolabeling runs, the unit dose volume was adjusted with phosphate buffered saline (PBS) which had a pH of 7.4. Using this to adjust the [F-18] NaF liquid volume increased the pH to greater than 6.5.

Up to the experiment on 2/2/2018, previous pH measurements were done with the BAKER-pHIX pH test strips. The experiment on 2/2/2018 was an attempt to reproduce some of the conditions present during the anomalous run on 10/12/17 with Type II. To do this, the initial activity concentration of the 2/2/2018 run was purposely made low, 0.59 mCi/mL and the pH was relatively high at 7.4. The pH for the 2/2/2018 was measured with an electronic pH meter. The meter was a Beckman model 360 serial number 3016. The meter calibration was performed with calibration solutions of known pH. The advantage of using pH strips is that the amount of liquid required is small. The pH meter requires enough liquid to cover the probe active area. The volume required to cover the probe was approximately 1 mL. During the 2/2/2018 experiment run, 1 mL aliquots were withdrawn instead of the 50 µL aliquots typically used. Thus, the initial

volume of the [F-18] NaF liquid had to be much larger than in previous experimental runs. As can be seen in Figure 24, the experiment run on 2/2/18 did not reproduce the slow adsorption rate seen in the 10-12-17 experimental run with Type II.

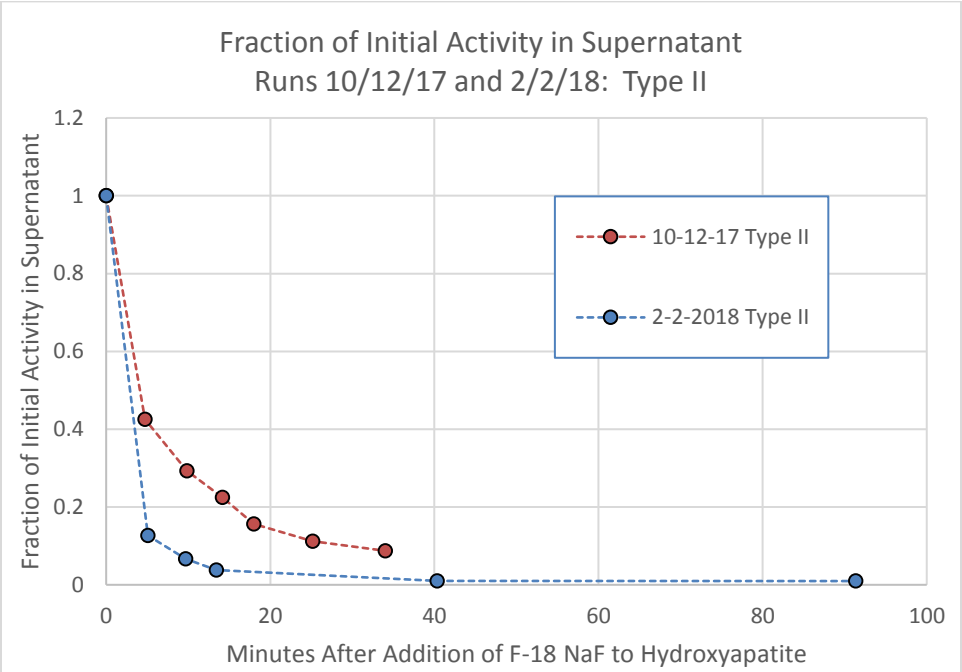

Figure 24: Fraction of initial activity in supernatant. Both experimental runs were performed with Type II CHT hydroxyapatite microspheres.

The pH of the 2/2/2018 as measured with the electronic pH meter is plotted in Figure 25. The pH of the 2/2/2018 run appears to remain fairly constant during the reaction time and does not vary from the initial pH. This is likely due to the large amount of PBS buffer used in the initial solution.

For the 10/12/17 Type II run, the pH of the initial solution was measured. The initial solution consisted of 0.7 mL of the original unit dose from PETNET. The volume was adjusted to 3 mL with PBS. The pH of this solution measured 6.7 to 7.0 with the pH

strips. This pH was within the typical pH range seen during other experimental runs. These results indicate that pH was not the factor in producing the anomalous results seen on the 10-12-2017 Type II run.

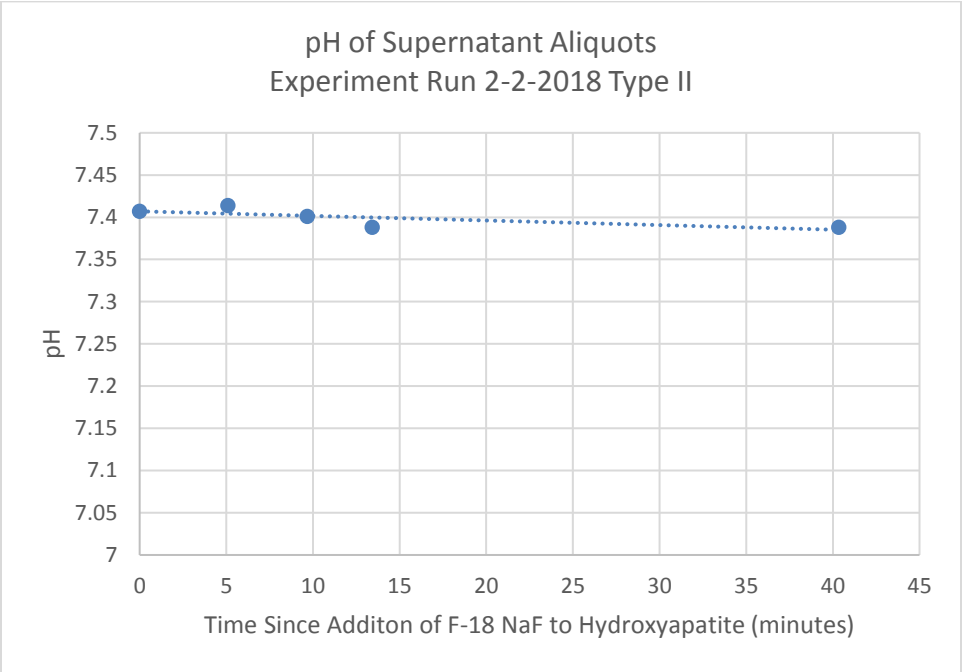

Figure 25: pH of aliquots removed from supernatant during experiment run 2/2/2018.

In these radiolabeling experiments, a value of primary interest was the labeling efficiency. The simple radiolabeling equation can be written as the following:

$$Labeling\ Efficiency\ \% = 100\ x\ \frac{microsphere\ activity}{(microsphere\ activity + supernatant\ activity)} \quad (2.1)$$

When the activity removed in the aliquots is considered, the activity accounting becomes slightly more complex. The simple labeling efficiency equation assumes that all of the activity introduced into the mixture remains in the mixture throughout the entire labeling process. However, in these experiments, the decay-corrected activity of the mixture at the end of the labeling process was not the same activity that was initially added to the hydroxyapatite microspheres. Small amounts of activity were removed with each aliquot. If each aliquot had been returned to the reacting mixture in the centrifuge tube, then the simple labeling efficiency equation could be used. However, this was not done.

The aliquots were not added back to the hydroxyapatite-sodium fluoride mixture for several reasons. During the handling of small amounts (50 µL) of liquid, including measurement in a dose calibrator, there would be a high probability of significant residual activity in the pipet tips and PerkinElmer vials. In addition, the experiment plan included measurement of the 50 µL aliquots in the Wizard^2 gamma counter. The aliquot activity was measured with two completely different radiation detection systems. This redundancy in data acquisition proved to be useful.

Each aliquot contained an amount of radioactivity that was permanently removed from the system. To account for the activity removed in each aliquot, a modified version of the labeling efficiency equation was used. In this metric, it is assumed that the activity that was removed with the aliquots would not have adsorbed on to the hydroxyapatite microspheres had it remained in the mixture. This is an unrealistic assumption, however is does put a lower boundary on the labeling efficiency. This metric is the minimum labeling efficiency:

$$Minimum\ Labeling\ Efficiency\ \% = 100\ x\ \frac{microsphere\ activity}{(microsphere\ activity + supernatant\ activity + \sum aliquot\ activity)} \quad (2.2)$$

The summation term in the denominator is the sum of the aliquot decay-corrected activity permanently removed from the reacting mixture. The supernatant term is the activity of the remaining supernatant remaining in the reaction vial with the hydroxyapatite. The labeling efficiency is greater than or equal to the minimum labeling efficiency.

The minimum labeling efficiency for all experiment runs was quite high. All runs except the 10-12-17 Type II run, had minimum labeling efficiencies greater than 96%. To perhaps put this labeling efficiency into perspective, most clinical radiopharmaceuticals are prepared at a commercial radiopharmacy from a "kit" and a radioactive solution. The kit contains the pharmaceutical precursor and the radioactive component is added to the kit to radiolabel the pharmaceutical. The preparation of most kits involve the addition of Tc-99m pertechnetate. After the kit is prepared, tests are performed to measure the radiochemical purity which is the amount of radiolabeled product in the desired form. Most kits for commercial radiopharmaceuticals consider a radiochemical purity of 90% or greater to be acceptable for administration to patients.

The small volume of the aliquots (50 µL) was a compromise. Each aliquot had to contain enough activity to get a reliable measurement in the dose calibrator. However, the volume needed to be kept small so as to not significantly perturb the reacting system.

The sum of the decay-corrected aliquot activity as a percent of the initial activity was kept low. In most instances the sum of the aliquot activity was less than 1% of the initial activity. In the 2/2/2018 experiment run, due to the relatively large 1 mL aliquots, the sum of the aliquot activity was 3.7% of the initial activity.

Another parameter of interest was the amount of F-18 that could be adsorbed onto the hydroxyapatite microspheres. As previously mentioned, Fan et al. were able to bind 142 mCi of F-18 per gram of crystalline hydroxyapatite. The amount of activity per gram is approximately 176 Bq per microsphere for 40 µm diameter microspheres. For all of the radiolabeling experiments, the 20 µm diameter microspheres were used. Per unit mass, there are 8 times as many 20 µm microspheres than 40 µm microspheres. Thus for a given activity per mass, 176 Bq/microsphere for 40 µm microspheres is equivalent to approximately 22 Bq/microsphere for 20 µm microspheres. This value was the initial "target" value for activity per microsphere. It was hoped that ceramic apatite would provide more surface area and active sites. It was anticipated that the amount of activity would be greater than what would be expected from crystalline hydroxyapatite.

These experiments have shown that it is possible to consistently radiolabel ceramic hydroxyapatite microspheres in the approximately 100 Bq/microsphere range for 20 µm microspheres. This is five times the "target" activity per microsphere. In two instances, the activity per microsphere exceeded 250 Bq per microsphere with a minimum radiolabeling efficiency of greater than 98%. The upper limit to the amount of activity that can be radiolabeled has not been found. It is entirely possible that 300 Bq per microsphere is achievable with a radiolabeling efficiency of 95% or more.

The activity per microsphere is an important parameter for several reasons. The number of microspheres should be kept low enough such that embolic effects are not caused by the surrogate particles. As a rule of thumb, the maximum number of surrogate particles that would be injected into a patient would be 1 million. The amount of F-18 bound to the microspheres must be sufficient to produce clinically acceptable images within a relatively short scan time. The activity of 1 million microspheres is listed in Table 3 and is sufficient activity for clinical PET imaging. The large amount of activity bound to the microspheres also would allow the clinician to reduce the amount of F-18 microspheres to less than a million while still having enough activity to produce acceptable images.

The amount of F-18 required to produce acceptable clinical PET images can be estimated by considering the following. The American College of Radiology (ACR) has published detailed instructions on how to test the image quality of a PET scanner using the ACR PET phantom [55]. The phantom is designed to produce images with similar characteristics representative of a human liver being imaged with F-18 FDG. The amount of activity used in the ACR PET phantom varies from 0.33 mCi to 1.68 mCi of F-18. The radiolabeling results presented in Table 3 indicate that a million microspheres would provide activity equivalent to what is used during imaging of the ACR PET phantom.

Table 3: Amount of F-18 that was radiolabeled to hydroxyapatite microspheres.

Date of Experiment Run	8/29	8/31	9/7	9/12	9/21	9/21	10/12	10/12	2/2
Microsphere Type	I	I	I	II	I	I	I	II	II
Activity per microsphere (Bq)	10	253	175	185	169	29	269	113	102
Activity of 1 million microspheres (mCi)	0.27	6.84	4.73	5.01	4.55	0.78	7.27	3.06	2.75

In summary, the ceramic hydroxyapatite microspheres have a capacity for binding significant amounts of F-18 from a [F-18] NaF solution. The radiolabeling is rapid and robust. Changes in a variety of parameters did not appear to greatly affect the adsorption rate or the radiolabeling efficiency. The radiolabeling efficiency does not seem to be overly sensitive to parameters such as pH, initial activity concentration or other parameters surveyed in these experiments.

B. In Vitro Binding Stability

1. Introduction

After the microspheres had been radiolabeled, tests were performed to determine how well the F-18 was bound to the microspheres. The binding stability of the radiolabeled F-18 to the microspheres was tested in the presence of a variety of materials. These materials included de-ionized water, 0.9% NaCl saline, phosphate buffered saline (PBS), bovine serum, and whole mouse blood. The materials of particular interest were the blood and blood products. Some investigations have shown that blood can remove

bound F-18 from resin microspheres [19]. These experiments were performed to help determine if similar results could be expected with hydroxyapatite microspheres.

2. Methods

The in vitro binding stability experiments were performed by applying a series of washes to the radiolabeled microspheres. The microspheres were left in the same polypropylene centrifuge tube used for the radiolabeling. A wash was performed by adding the test material to the microspheres. The volume of the test material was usually 5 mL. The mixture was then agitated and in some instances allowed to sit for a period of time. Then the mixture was centrifuged to force the microspheres into the tip of the centrifuge tube. The supernatant above the hydroxyapatite pellet was drawn off. It was critical to avoid drawing microspheres into the pipet tip. Care was taken to not get too close to the microsphere pellet when drawing off the wash fluid. Approximately 0.5 mL of liquid was typically left on the hydroxyapatite pellet. After the wash fluid was removed, material for another wash would be added to the reaction vial and a new round of washing was started. The material drawn off during a wash was measured in the dose calibrator. Aliquots of constant volume (50 µL) were collected in the PerkinElmer vials. The aliquot vials were collected and placed into a rack and measured with the Wizard^2 automated counting system.

The different types of material that were used included 0.9% sodium chloride saline. The phosphate buffered saline (PBS) solution used was Gibco PBS pH 7.4 (1X), 1000 mL container, Lot 1843259. Bovine serum, B9433, 100 mL container, lot 16A041, was purchased from Sigma-Aldrich. Whole mouse blood was obtained from a mouse

that had been sacrifice as part of a research study that was unrelated to this study. The volume of the blood was 0.8 mL. De-ionized water is available from a tap in the lab.

When new wash material was added to the mixture, there was no activity in the fresh wash material. Any residual fluid with the hydroxyapatite pellet was from the previous wash or remaining supernatant from radiolabeling. The addition of the fresh material dilutes the residual fluid. As the F-18 disassociates from the hydroxyapatite microspheres, the activity concentration in the wash material increases and may reach an equilibrium concentration. At this point, the removal of the adsorbed F-18 from the microspheres may slow or stop until fresh unsaturated material is added. This does not mimic the process in an animal. In the animal model, there is a constant flow of fresh, unsaturated material. If the F-18 is removed from the microspheres and deposited elsewhere in the body, such as the skeletal system, the activity concentration in the blood may never reach a saturation level. Even at low removal rates, the constant removal may result in a significant amount of activity removed over time.

Early in vitro stability experiments were done at the pH that the unit dose was delivered. In these cases, the measured pH remained in the 5.6 to 6.1 range. During these early experiments it was noticed that a small, but possible significant, the amount of F-18 was disassociating from the hydroxyapatite. A possible reason that the F-18 was continually being removed was found in the vendor literature. There was a strong recommendation that when working with CHT ceramic hydroxyapatite microspheres, the pH should be greater than 6.5. It was possible that the acidic conditions were contributing to the removal of the F-18 from the microspheres. Later experiments were done with materials that kept the pH above 6.5. Increasing the pH of the in vitro

experiments also brought the pH closer to the physiologic pH of 7.4 for closer modeling of the conditions in the animal model.

3. Results

Figure 26 shows the percent activity bound to the microspheres during washing. The results are also presented in Figure 27 which has an expanded vertical axis for easier visualization of the data. The start of the washing phase was considered to be time zero. At this time, 100% of the activity was considered bound to the microspheres. In general, the results were favorable

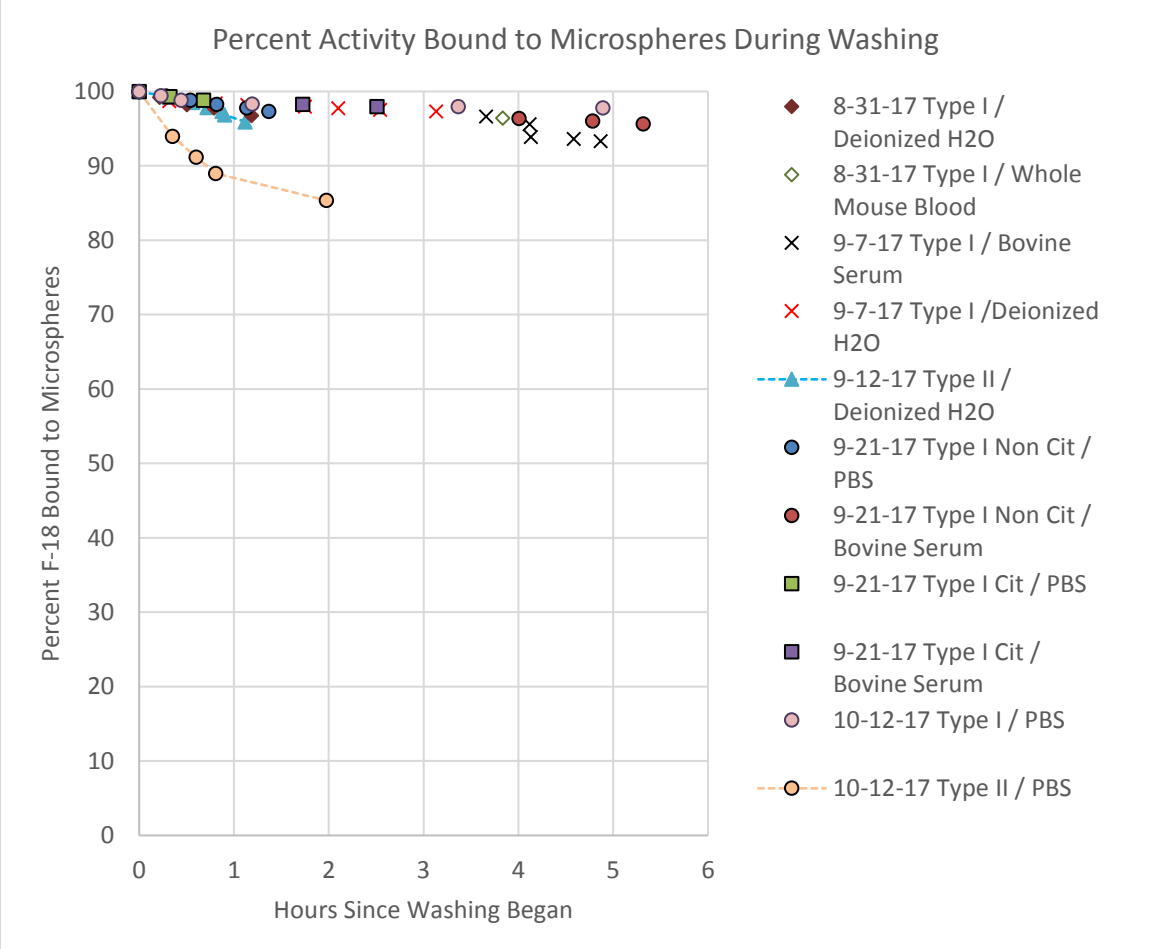

Figure 26: Activity bound to microspheres during washing with a variety of materials.

In most cases, more than 92% of the initial activity remained bound to the microspheres even after several hours of washing. The amount of F-18 that was being removed during each wash was a small fraction of the total activity bound to the microspheres. For instance, in one case the CHT was washed in deionized water for 3 hours and then bovine serum for an additional 1.8 hours. At the end of the washing, 93% of the initial activity was still bound to the CHT.

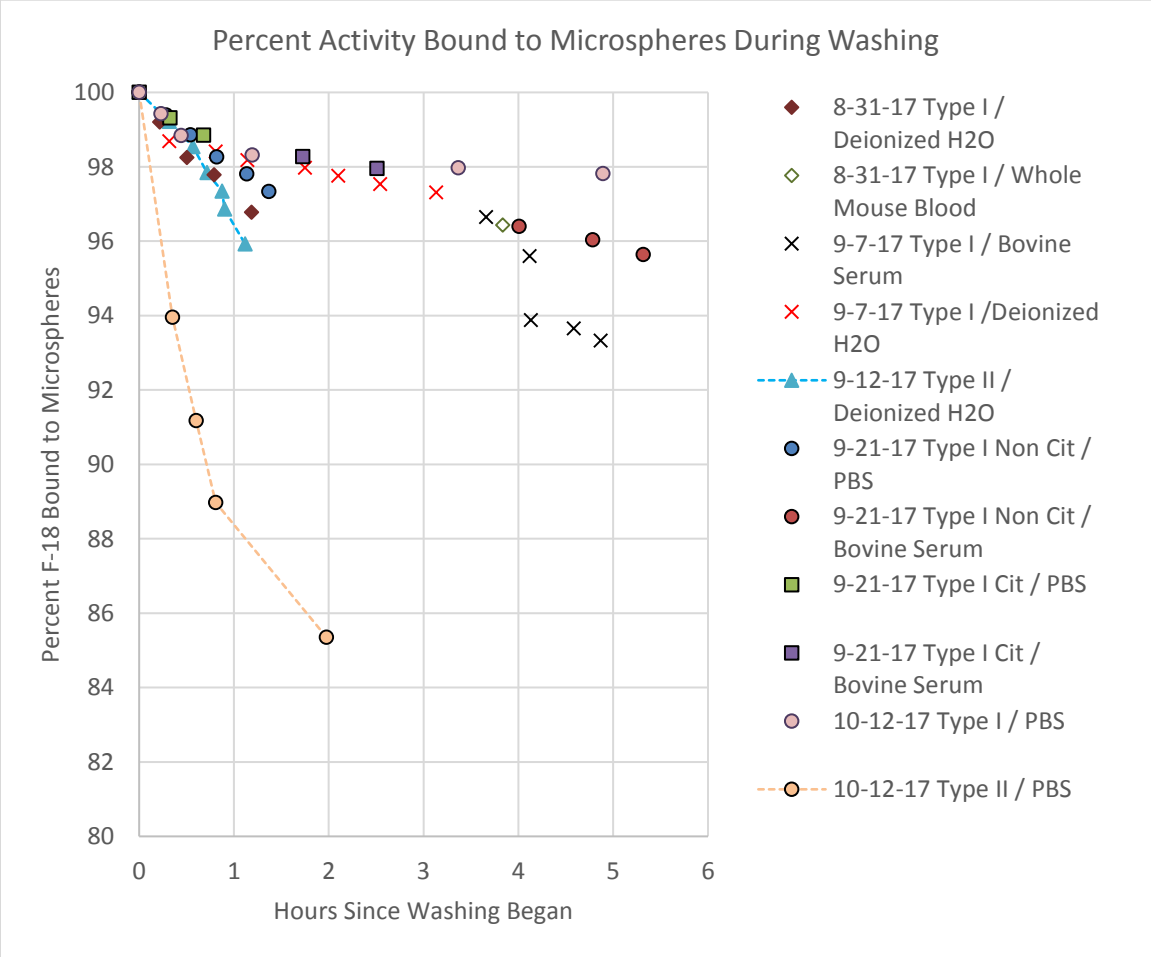

Figure 27: This is the same data as previous figure. Vertical axis has been expanded for better data visualization.

Table 4: Results of In Vitro Testing of Stability of Radiolabel.

	8/29	8/31	9/7	9/12	9/21	9/21	10/12	10/12
Microsphere Type	I	I	I	II	I	I-citrated	I	II
Wash material	0.9% NaCl Saline	0.9% NaCl Saline	D.I. Water	D.I. Water	PBS	PBS	PBS	PBS
Wash duration (hours)	0.2	1.7	3.1	1.1	1.4	1.2	4.9	2.0
Wash volume (mL)	3.0	20.0	35.0	17.0	25.0	15.0	23.8	20.0
Average wash rate (mL/hour)	15.0	12.1	11.2	15.2	18.3	12.6	4.9	10.1
Percent F-18 remaining on microspheres	99.6	96.8	97.3	95.9	97.3	98.5	97.8	85.4
Percent F-18 removed in wash	0.4	3.2	2.7	4.1	2.7	1.5	2.2	14.6
Second Wash								
Wash material		Mouse Blood +0.9% NaCl Saline	Bovine Serum		Bovine Serum	Bovine Serum		
Wash duration (hours)		3.0	1.7		4.0	1.8		
Wash volume (mL)		1.8	25.0		15.0	15.0		
Average wash rate (mL/hour)		0.6	14.4		3.8	8.1		
Percent F-18 remaining on microspheres		96.4	93.3		95.6	97.7		
Percent F-18 removed in wash		0.3	4.0		1.7	0.8		

In general, the binding of F-18 appeared stable in blood products. Results with bovine serum and whole mouse blood show that the initial activity remained bound to the microspheres hours after the washing phase of the experiments began.

In some of the experiment runs, more than one type of wash material was used. For instance on 8-31-2017, the first four washes were done with 0.9% NaCl saline over the course of 1.18 hours. Afterwards, approximately 0.8 mL of whole mouse blood was added to approximately 1 mL of 0.9% NaCl saline and used as a wash. The results from the mouse blood were favorable. The hydroxyapatite was washed in whole mouse blood for 3 hours. During this time the mixture was agitated an allowed to sit. At the end of the wash, 1.8 mL of blood was withdrawn. Measurements indicate that the blood removed 0.35% of the activity that was present on the hydroxyapatite at the beginning of the blood wash.

The two runs with the most rapid disassociation of the F-18 from the microspheres occurred with Type II microspheres. These are the 9-12-17 run with de-ionized water as the wash agent and the 10-12-17 run with PBS as the wash agent. In the 9-12-17 run 4% of the activity was removed from the Type II microsphere using 17 mL of de-ionized water. In the previous experimental run on 9-7-17, only 2.7% of the activity had been removed from Type I microspheres using 35 mL of de-ionized water and washing for nearly three times the length of time used for washing on 9-12. This suggests that the Type II microspheres disassociate F-18 more readily than Type I microspheres. The Type II microspheres are the more porous of the two types. Whether the porosity or some other factor makes the Type II microspheres more susceptible to F-18 loss is unknown.

The 10-12-2017 run with the Type II microspheres is notable in that it has most rapid disassociation of F-18 from the microspheres. This is the same experimental run that had the anomalous radiolabeling rate. There was something unusual about this run but unfortunately a conclusive reason is not available. Detector errors are unlikely since dose calibrator and Wizard^2 gamma counter measurements are in agreement.

Contamination of the unit dose is unlikely since the unit dose from PETNET was split into two doses. One dose was used to radiolabel the Type I microspheres, the other was used for the Type II microspheres. As previously mentioned, it is possible that there was a mix up in the phosphate buffered saline (PBS). It would be a simple matter to test this theory. A radiolabeling run and a wash run can be performed with 10x PBS to see if the results seen in the 10-12-17 Type II run is reproduced.

The Type I CHT microspheres were likely the best choice for use in an animal model. The in vitro stability data was used to test the quality of the radiolabel prior to injection into an animal. During preparation of the F-18 microspheres for injection into an animal, the labeling efficiency was checked. It was known that at 15 to 20 minutes after the addition of F-18 NaF to the microspheres, the labeling efficiency should be in excess of 95%. When the radiolabeling appeared satisfactory, the microspheres were then to be washed in PBS for 30 minutes. It was expected that the F-18 binding should remain stable with more than 96% of the activity remaining on the microspheres. If the F-18 binding was not stable as in the case of the 10-12-17 Type II run, then the amount of activity remaining on the microspheres was expected to be less than 96% at the 30 minute time point. This testing allowed for easy differentiation between useful and poorly labeled batches of microspheres.

C. In Vivo Binding Stability

1. Introduction

The binding stability of the F-18 radiolabeled microspheres was tested in an animal model. PET imaging was used to assess the amount of F-18 that disassociated from the microspheres. Rats were chosen as the animal model for this investigation. Rats and mice have been previously used in similar investigations with success [19], [39], [50]. For this pilot study, the protocol was submitted to the Institutional Animal Care and Use Committee (IACUC). The protocol number, 18-200686-HSC was assigned by the Office of Animal Care Compliance (OACC) upon approval. Permission was given to use up to four female rats. At the beginning of the animal experiment, the intent was to seek approval to expand the study if the radiolabel microsphere performance was acceptable.

The animal model was used to investigate the stability of the radiolabel in the entire organism. This includes the myriad of tissue types and physiological processes present in a living rat. Whole body PET imaging is very sensitive and can detect small amounts of activity in the skeleton or other locations in the body. PET imaging over time can quantify the amount of F-18 that is disassociating from the hydroxyapatite microspheres. The sequence of procedures was anesthesia, I.V. injection, imaging and then euthanasia.

The F-18 radiolabeled microspheres were injected into the tail vein of a rat. As expected, the microspheres collected in capillaries of the lungs which are the first biological filters downstream from the injection site. If the F-18 remained bound to the

microspheres, then PET imaging would show all of the radioactivity localized in the lungs. If the F-18 was removed from the microspheres, the likely place for free F-18 fluoride ions to localize was in the skeletal system. It is well known that free F-18 in the blood tends to collect in the skeletal system. F-18 sodium fluoride is routinely used for performing clinical PET skeletal imaging of humans.

The solution volume for injection into the rat was expected to be 200-400 microliters. This volume contained approximately 200 to 500 micrograms of hydroxyapatite particles. This is equivalent to 60,000 to 120,000 microspheres. The microspheres have a nominal diameter of 20 microns. The number of microspheres is not unusually large. For instance, Selwyn et al. injected 100,000 resin microspheres into the tail vein of a rat without incident[19]. The resin microspheres were 30 microns in diameter.

There is evidence that hydroxyapatite in lungs is stable in vivo while hydroxyapatite in liver may not be stable. In an investigation by Jauregui-Osoro et al. 2011, they injected several forms of hydroxyapatite radiolabeled with F-18 [50]. The size of the particles used were 200 nm or less. This group found that the nanoparticles in the lungs were stable. There was evidence that nanoparticles that migrated to the liver and spleen were taken up by phagocytic cells of the reticuloendothelial system. Over a period of four hours, these nanoparticles then gradually released F-18 which then collected in the skeleton. These nanoparticles are two orders of magnitude less than the microspheres used in this investigation. Microspheres that are 20 µm in diameter are much less likely to be incorporated into phagocytic cells [51]. In addition, our imaging study occurred within 2 hours, not 4 hours after injection [50].

2. Methods

Hydroxyapatite microspheres were labeled with F-18 using the methods described in the radiolabeling section. To begin, 4 milligrams of Type I CHT microspheres was measured and placed in a 15 mL centrifuge tube. The volume of the [F-18] NaF unit dose was increased with PBS. A 50 µL aliquot was removed from the [F-18] NaF solution. The pH of the initial solution was measured with BAKER-pHIX pH test strips and found to be 6.7. The [F-18] NaF was then added to the centrifuge vial containing the microspheres. At the time that the F-18 NaF was added to the microspheres, the [F-18] NaF activity was 3.33 mCi. The residual dose was 0.25 mCi. After the fluid was added, the vial was capped and the mixture was agitated by hand for approximately one minute. The contents were centrifuged at 2500 RPM for 3 minutes. After centrifuging, a 50 µL aliquot was removed. The aliquot was measured in the dose calibrator and found to have an activity of 2.0 µCi. This was 12 minutes since the addition of the [F-18] NaF to the microspheres. The aliquot activity measurement was compared to the 50 µL aliquot taken from the [F-18] NaF prior to the addition of the NaF to the hydroxyapatite. The activity of this aliquot measured 58.9 µCi. Calculation showed that the activity in the supernatant was approximately 3% of the initial activity (2/58.9 = 0.03). The process was repeated. The mixture was agitated by hand and centrifuged. At 19 minutes since the addition of the [F-18] NaF to the microspheres, a 50 µL aliquot was again taken from the supernatant. The activity of the aliquot was measured in the dose calibrator and found to be 0.40 µCi. This activity was compared to the aliquot taken prior to addition of the NaF to the microspheres. This measurement indicated that the activity of the

supernatant was 0.6% of the initial supernatant activity. At this point, the amount of F-18 that could be bound to the microspheres had likely reached a maximum. Subsequent calculations indicate that the labeling efficiency was greater than 99%.

The mixture was agitated and centrifuged again to separate the microspheres from the supernatant. Approximately 1.8 mL of supernatant was then removed from the centrifuge vial. The microspheres and approximately 0.2 mL of supernatant remained in the centrifuge vial. The microspheres were washed by adding 5 mL of phosphate buffered saline (PBS). The mixture was shaken by hand and then centrifuged at 2500 RPM for 3 minutes. An autopipette was used to remove 5 mL of the wash liquid. The 5 mL of wash liquid measured 10.66 µCi. A second wash was performed by adding 5 mL of PBS to the microspheres, agitating and centrifuging. After being centrifuged, the second wash was removed and measured in the dose calibrator. The second wash measured 8.53 µCi. The centrifuge tube contained 1 mL of liquid and the hydroxyapatite microspheres. The activity of the centrifuge tube was 1.89 mCi. The activity in wash 2 was approximately 0.4% of the total activity. At this point, it was decided to draw the dose for injection into the rat.

The animal that was selected was a small female Sprague Dawley rat that was acclimated one week before being used. The animal weighed 170.3 grams prior to injection. The animal was anesthetized with isoflurane which is an inhalant. The initial dose was 4% to 5% at induction with oxygen and then 1.5% to 2% for maintenance of the anesthetized state.

The volume of the fluid containing the microspheres was adjusted to 2.0 mL with PBS. The pH of the fluid was measured with BAKER-pHIX pH test strips and was

found to be 7.0 to 7.3. A dose volume of 400 µL was drawn into a 1 mL TB syringe and measured in the dose calibrator. The measured activity was 223 µCi. The microspheres were slowly injected into the tail vein of the rat. The residual activity in the syringe was measured in the dose calibrator and found to be 66 µCi. The injected activity at the time of injection was 151 µCi. The injected volume contained 9.56 x 10^4 microspheres. The activity per microsphere at the time of injection was 58 Bq/microsphere. The activity per microsphere was lower than initially planned for. However, the number of microspheres that were injected was close to what was specified in the protocol. The protocol called for 120,000 to 100,000 microspheres to be injected. Due to delays and the short half-life of F-18, the total injected activity was lower than initially planned. However, the activity proved to be sufficient for imaging.

Within a few minutes of injection, the rat was placed into the bed for the PET scanner. The animal was then transferred to the scanner and positioned for imaging. The imaging was done with a LabPET small animal PET scanner. The scanner is built as a ring of detectors. Each detector contains LYSO and LGSO crystals coupled to an avalanche photodiode. The scanner has a 10 cm transaxial field of view.

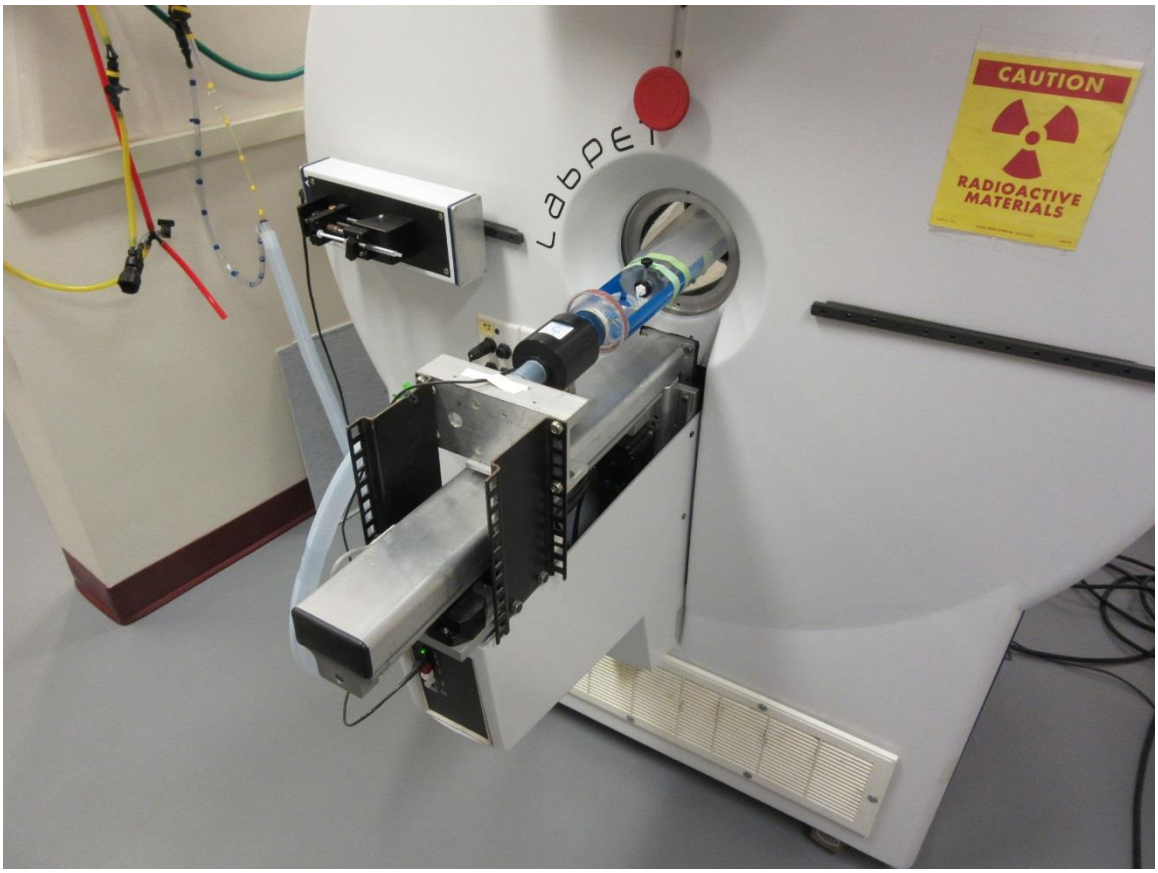

Figure 28: LabPET small animal PET scanner

The first PET imaging series was started 12 minutes post-injection. This was a 10-minute acquisition of a single bed position. The animal was positioned with the lungs in the field of view. The second imaging series was another 10-minute lung acquisition started 32 minutes post-injection. The third series was a whole-body acquisition that was started 43 minutes post-injection. The entire imaging time for the whole-body scan was 25 minutes. A total of 4 bed positions were scanned. The imaging time was roughly divided equally over the 4 bed positions. The fourth series was another whole-body acquisition that was started 79 minutes post-injection. The entire imaging time was 25 minutes over 4 bed positions. The last PET series was another 10-minute acquisition of

the lungs. This was started 109 minutes post-injection. After the PET acquisitions, that animal was transported to the small animal SPECT/CT. Here a helical whole body CT was acquired with a scan time of 6 minutes and a pitch of 1.5. The tube voltage was 65 kVp. The tube rotation time was 0.5 seconds. CT images were reconstructed using filtered backprojection with a Ram-Lak filter. The PET images were reconstructed using the MLEM iterative reconstruction algorithm using 10 iterations.

The animal was euthanized immediately after imaging with no chance for recovery in accordance with the approved IACUC protocol. This was performed by increasing the isoflurane to 5% with oxygen. The animal was monitored for signs of death. The animal carcass was held for radioactive decay in storage.

3. Results

The results of the rat imaging showed that all of the injected activity remained in the lungs. Careful examination of the Maximum Intensity Projection (MIP) images show that the accumulation of F-18 in the skeletal system was not present. Figure 29 shows two views of the rat. This whole-body acquisition took a total of 25 minutes to acquire. The start time was 79 minutes post-injection. The feature labeled A in Figure 29 is a fiducial created by placing 50 µL of radioactive fluid in a 0.2 mL PCR tube. The activity of the source was 54 µCi 20 minutes prior to injection. The feature labeled B in Figure 29 is the injection site in the tail. This is not unusual. Residual activity is often found at injection sites. The intensity scale was set in Figure 30 to maximize visualization of activity. Note that the activity in the tail is easier to see. Activity was not visible in the joints or bones.

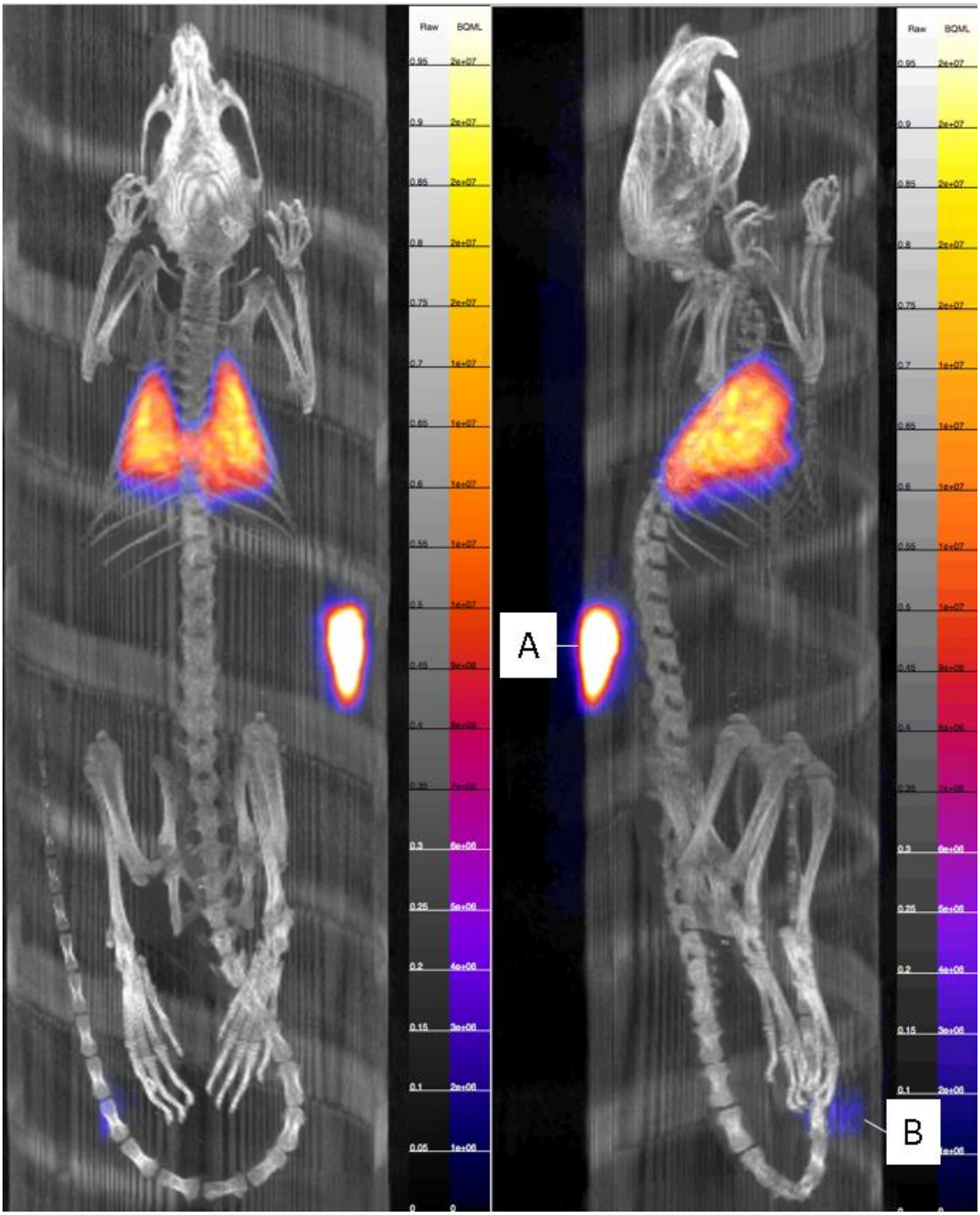

Figure 29: Coronal and oblique views of rat. Feature A is a small fiducial. This was 48 µCi of F-18 in 50 µL of fluid in a 0.2 mL PCR vial at the time of injection. Feature B is residual activity in the injection area.

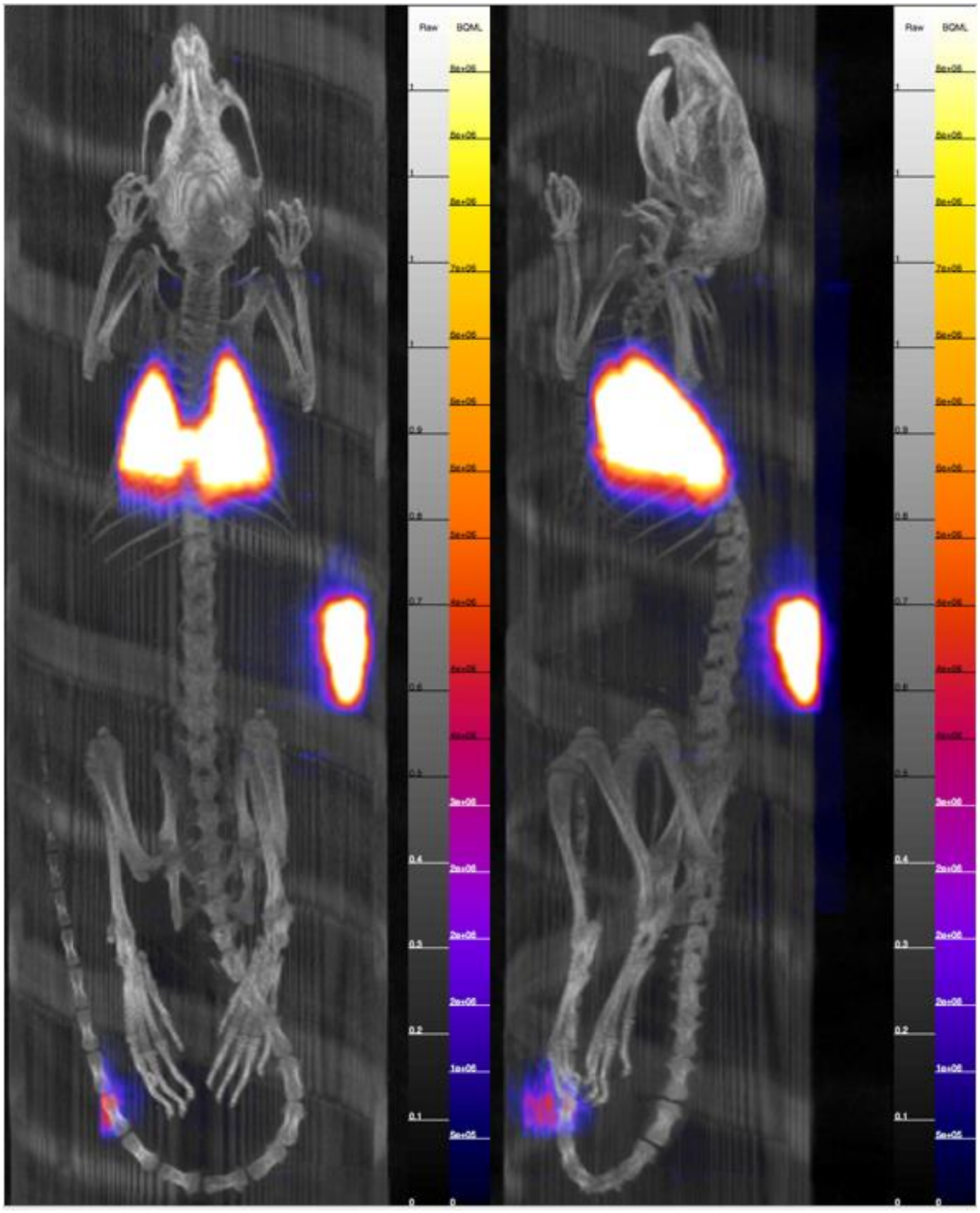

Figure 30: Two views of rat. Intensity has been set to maximize visualization of activity.

A Volume of Interest (VOI) was drawn around the lungs in the three lung-only series. The CT with the lung VOI overlaid in green is shown in Figure 31. The same

lung VOI was drawn in all three lung series to collect data to form a time-activity curve (TAC) for the lungs shown in Figure 32. The TAC for the lungs has been corrected for radioactive decay. The amount of F-18 in the lungs appears to remain constant over the time the animal was scanned which was approximately 2 hours.

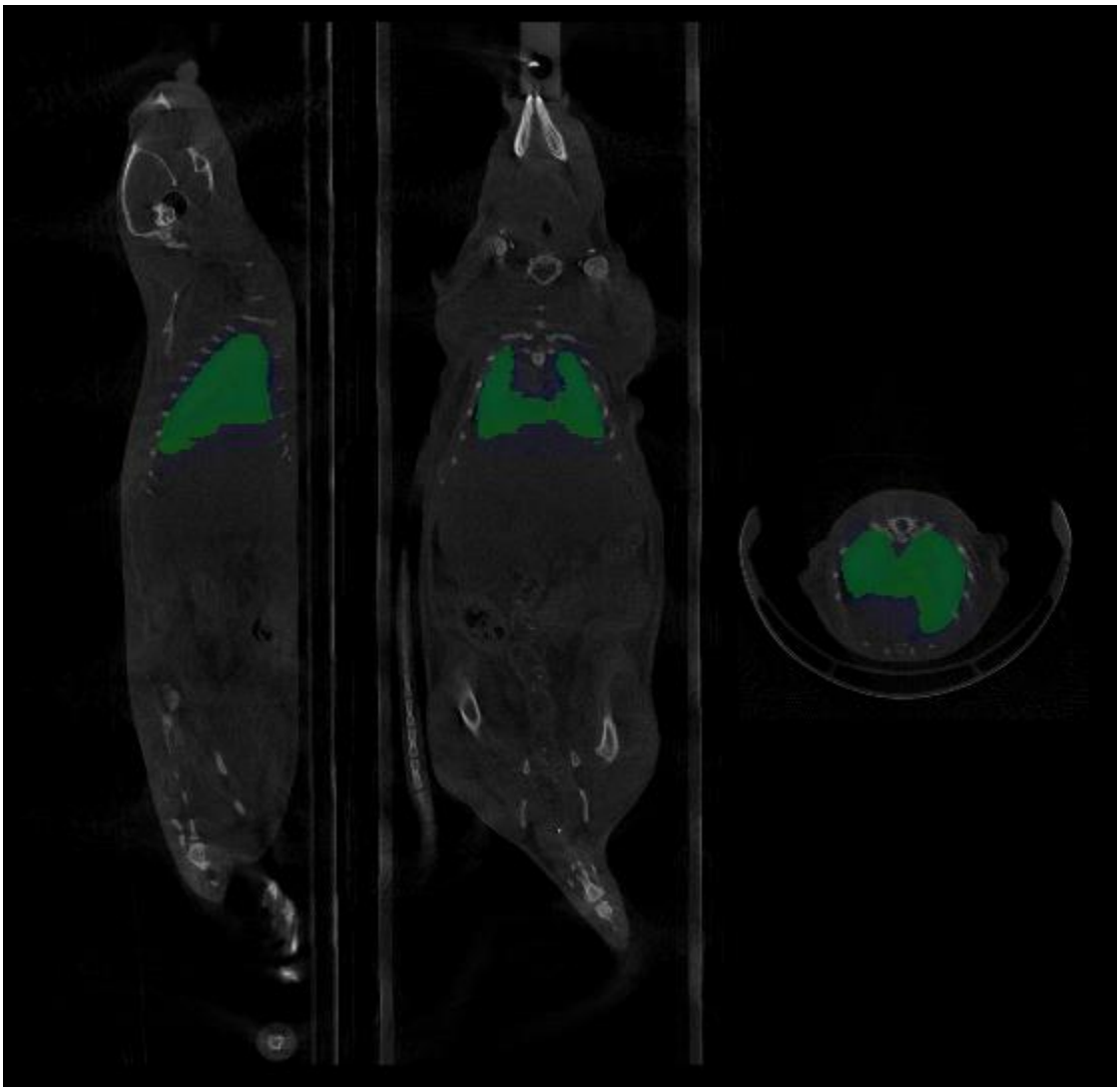

Figure 31: CT of rat with lung VOI in green. The same VOI was used in all five series to form TAC curve.

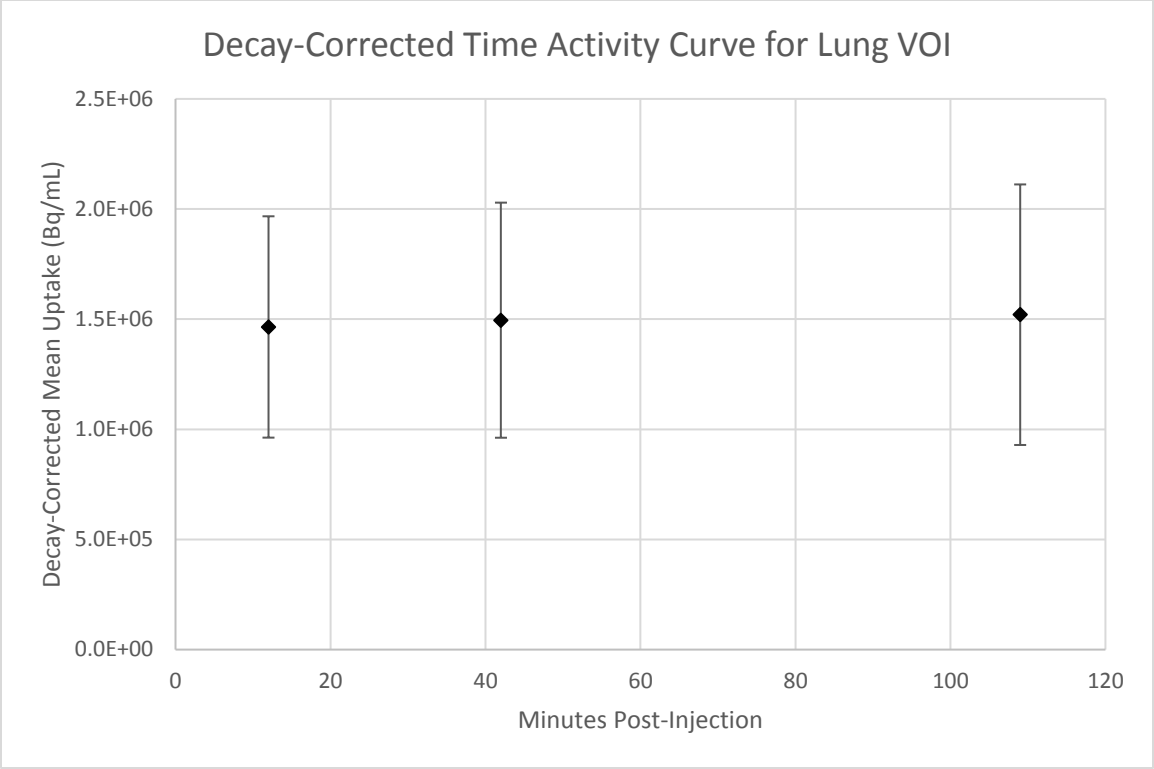

Figure 32: Time Activity Curve for lung VOI. Each data point is placed at the start time for the imaging series. The activity has been decay corrected to the time of injection. The error bars represent one standard deviation from the mean.

A similar process was followed to draw a volume of interest in the spine. The spine VOI was used to measure potential uptake in the skeleton over the imaging time. The CT with the spinal VOI overlaid in cyan is shown in Figure 33. The decay-corrected, data was used for the TAC shown in Figure 34. The amount of activity in the spine VOI appears to remain constant over the imaging time of nearly 2 hours.

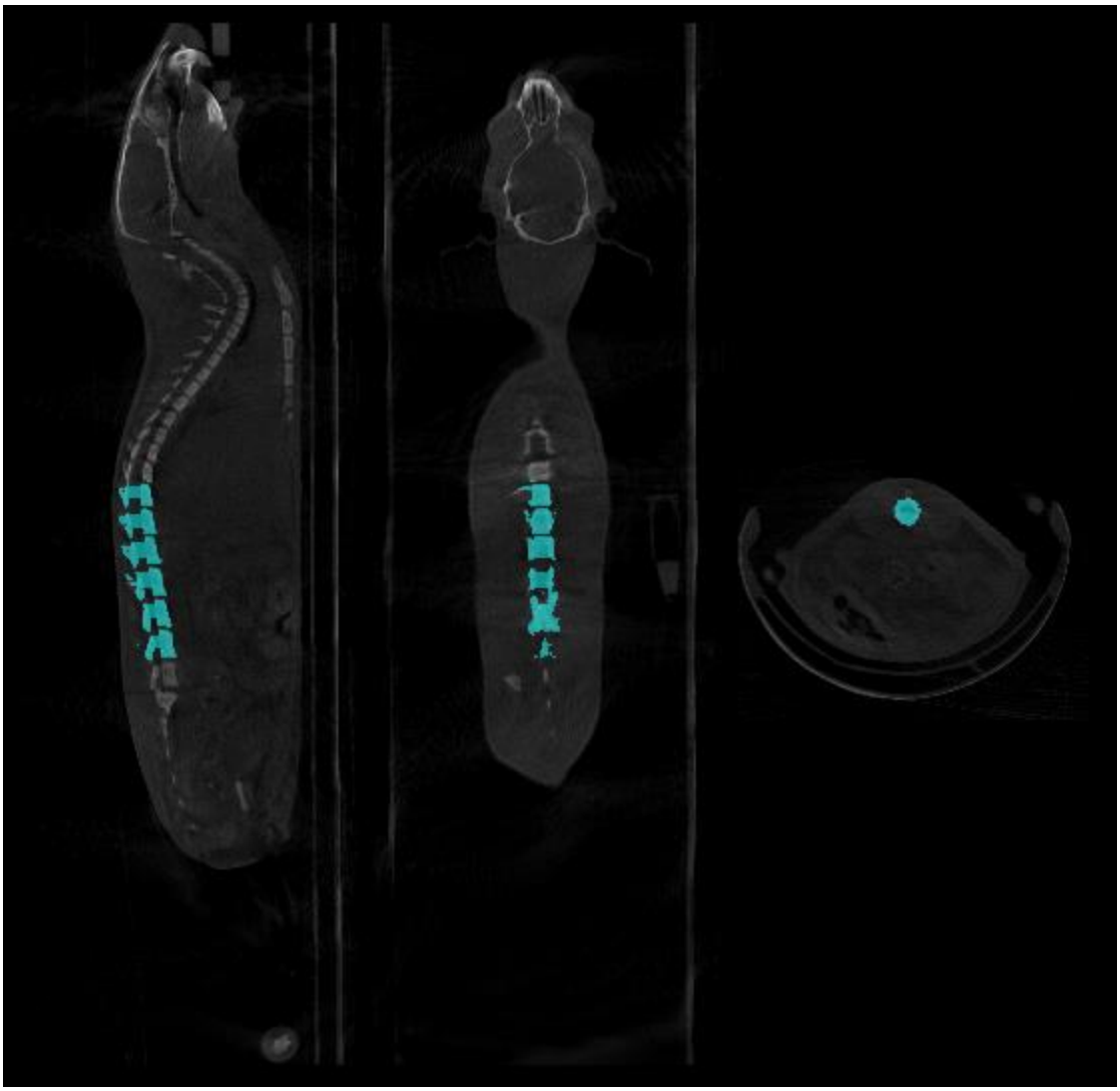

Figure 33: CT of rat with spinal VOI shown in cyan. The same VOI was used in all three lung-only series to collect data for a TAC for the spine.

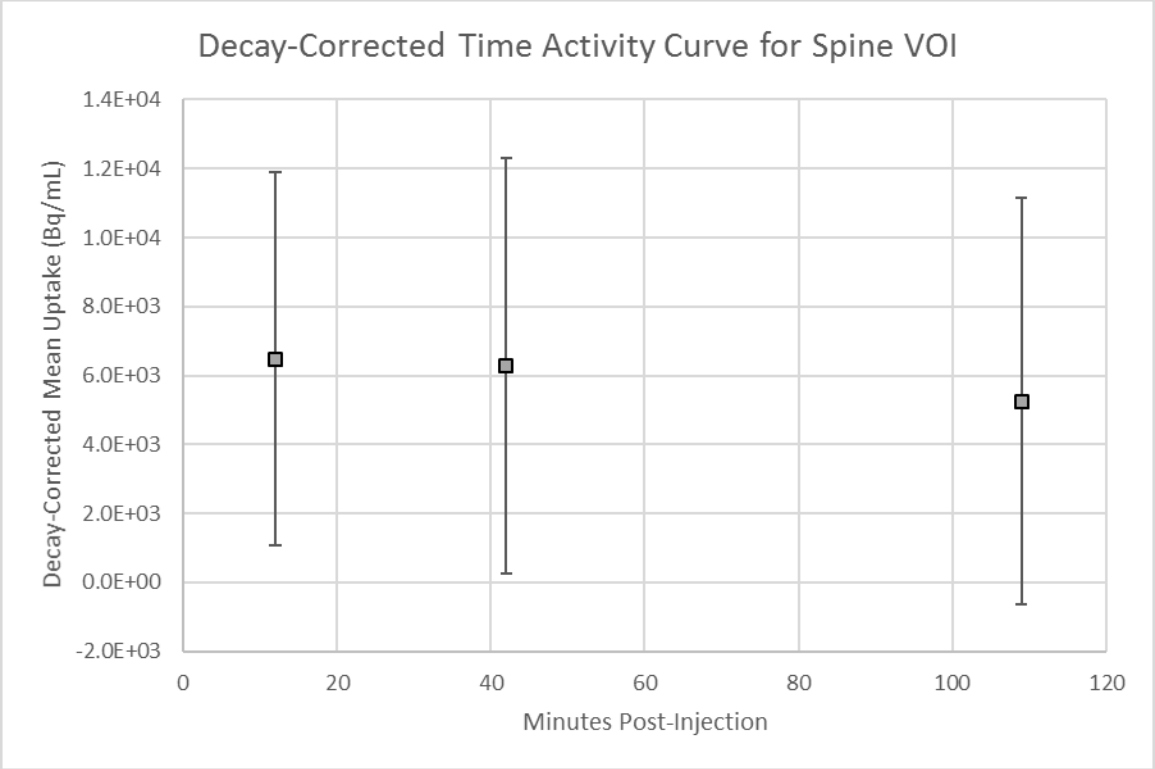

Figure 34: Time Activity Curve for spine VOI. Each data point is placed at the start time for the imaging series. The activity has been decay corrected to the time of injection. The error bars represent one standard deviation from the mean.

It was suspected that he measured uptake in the spine VOI was likely due to scatter from the lungs and fiducial. Three additional VOIs were drawn to measure the background uptake values. The background VOIs are shown in Figure 35. A plot of all VOIs is shown in Figure 36. The uptake in the spine VOI is on the same order of magnitude as the background VOIs. Note that the mean uptake is measured in activity concentration (Bq/mL) not activity. The uptake in the background VOIs appears to correlate with the proximity to the lungs and fiducial. This confirms that the uptake measured in the spine VOI was likely due to scatter.

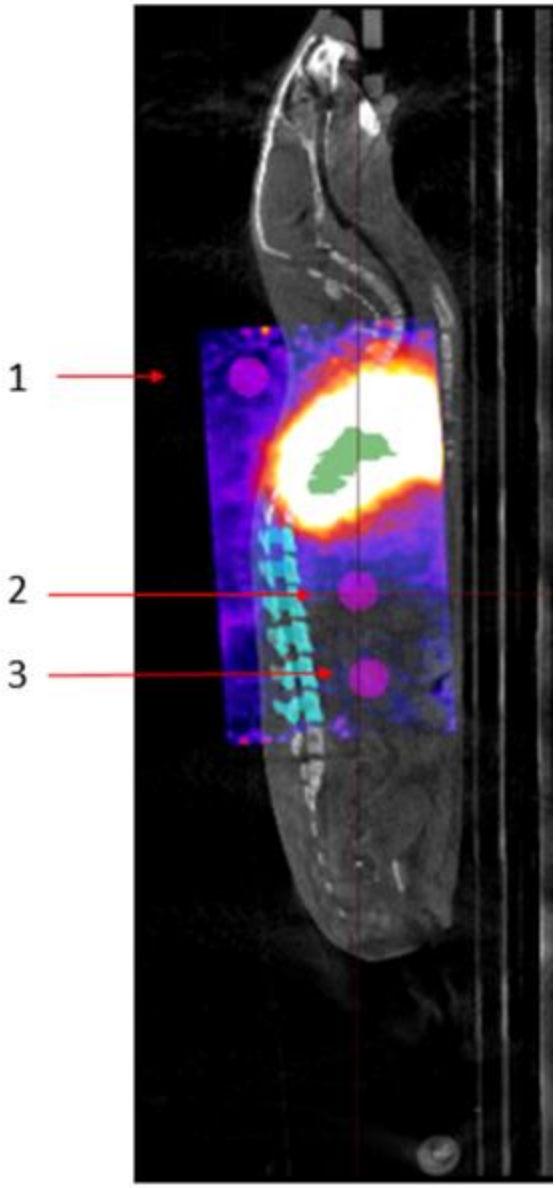

Figure 35: Three background VOIs colored magenta are shown labeled as 1, 2, and 3. The intensity of the PET image has been increased to maximize visualization of scatter.

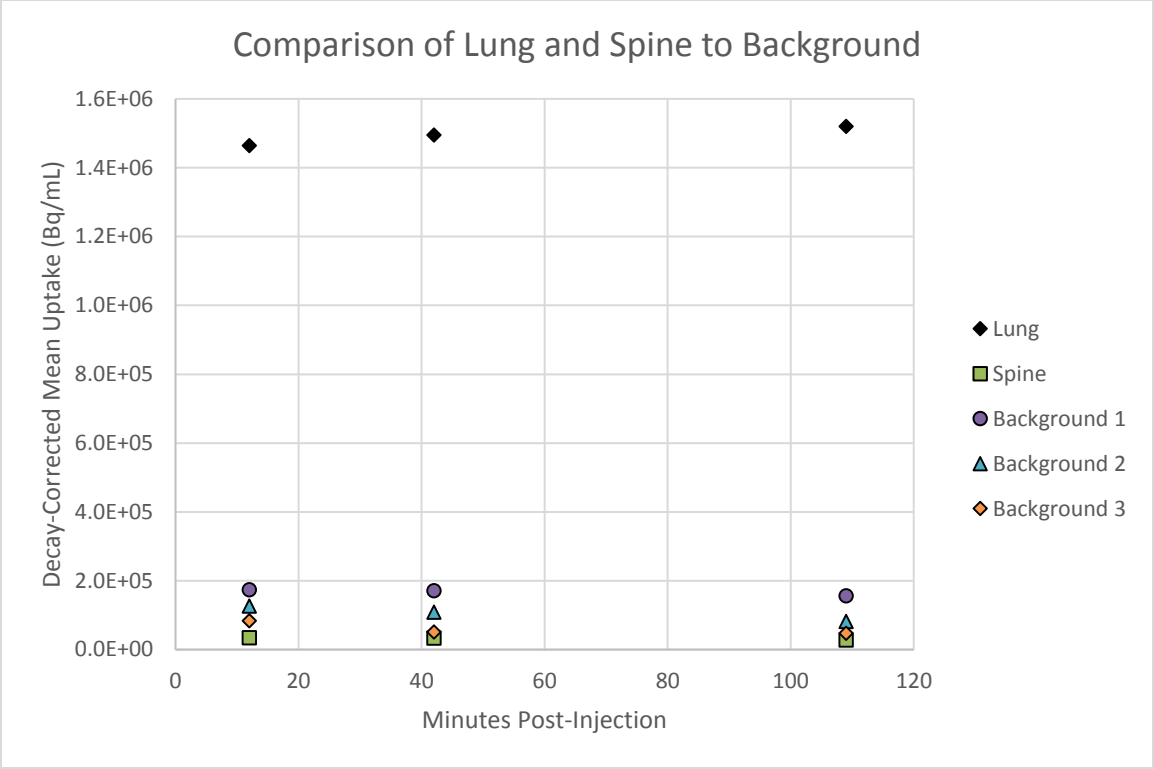

Figure 36: The decay-corrected uptake for the lungs, spine and background VOIs are shown. The uptake in the spine VOI is similar to the uptake in the background VOIs.

The conclusion from the animal imaging is that the F-18 radiolabel is stable in vivo over two hours post-injection. The particles did not appear to breakdown or fragment during imaging. Due to the microspheres size and shape, the expected localization of the particles was in the lungs. The activity per microsphere is sufficient for animal imaging and would provide enough activity for translation into imaging in humans.

III. Image-Based Dosimetry

A. Monte Carlo Modeling

The advantage of full, direct Monte Carlo modeling is that it is possible to closely model the physical processes underlying radiation transport and interaction with matter. Monte Carlo modeling naturally takes into account the stochastic nature of radiation interactions. The primary disadvantage is the computation time required to achieve results with acceptable levels of statistical uncertainty. Depending on the needs of the user, the computation time required for Monte Carlo may not be an issue. Typically, there is one to two weeks between the administration of the surrogate Tc-99m MAA and the administration of the Y-90 microspheres. If a similar time frame is assumed for a positron-emitting surrogate, the use of the Monte Carlo method should be sufficient. When the clinical situation requires faster dose calculation for treatment planning, methods to reduce computation time can be explored.

Other methods of performing image-based dosimetry will be briefly described. In the dose point kernel (DPK) method, a dose point kernel is a three-dimensional representation of the absorbed dose delivered by a point source in a homogeneous medium. The activity in a material can be considered an array of point sources weighted by the activity of each source. In the process of convolution, the dose to a point of interest is the superposition of all of the doses delivered by the array of point sources surrounding the point of interest [8], [56], [57]. The dose point kernel method can be performed rapidly with the Fast Fourier Transform or Fast Hartley Transform[8]. The use of a transform speeds the dose calculation but imposes a constraint that the kernel is

spatially invariant. The use of the DPK method for calculation of dose at inhomogeneities such as tissue interfaces can result in significant errors.

The S-voxel method was developed within the MIRD schema [57]. The following equation is used for calculation of dose:

$$Dose_k = \sum_{h=0}^{N} \tilde{A}_h \cdot S(voxel\ k \leftarrow voxel\ h) \tag{3.1}$$

In this method, a source voxel, h, has an associated cumulated activity, $\tilde{A}_h$. The dose to voxel k from the activity in voxel h is the product of the cumulated activity in voxel h multiplied by an S-value that describes the dose delivered to voxel k by the activity in voxel h. The total dose delivered to voxel k is the sum of the dose contributed by N surrounding voxels. In MIRD publication 17, three-dimensional arrays of S-values are tabulated for a variety of isotopes and voxel sizes. The S-voxel method is susceptible to error and inhomogeneities such as tissue interfaces.

The Local Deposition Model (LDM) is based on the assumption that the dose in a voxel is due to the activity within a voxel [56]. The activity within a voxel is multiplied by a LDM constant to produce a dose per voxel. Image blurring will spread the activity associated with a source. This will in turn, spread the dose calculated with the LDM.

These other methods are primarily used to reduce the computation time for image-based dose calculations. In some instances, the Monte Carlo modeling has been done before hand. When applied to a specific dosimetry problem, the method relies on a straightforward look-up and summation. Full Monte Carlo modeling can handle inhomogeneities such as tissue interfaces but at the expense of large computational time.

There were several considerations when choosing which Monte Carlo program to use. The ability to use medical images as input to the Monte Carlo program was important. Other considerations included having examples, good documentation and established validation in the literature. Programs that were considered included MCNP, GEANT4, and Penelope.

GATE (GEANT4 Application for Emission Tomography) is an open source toolkit based on the Monte Carlo program GEANT4 [58], [59]. GATE is designed for modelling emission tomography imaging systems such as Positron Emission Tomography (PET) and Single Photon Emission Computed Tomography (SPECT). The user is able to use medical images in the MetaImage format as input. The output options from GATE also include images in the MetaImage format. These images contain a header (.mhd file extension) and raw data (.raw file extension). An open-source program with the name "VV" can be used to convert tomographic image series in the DICOM format into the MetaImage format [60]. Once in the MetaImage format, the tomographic data can be imported into GATE and used as a non-radioactive object or as a voxelized source of radioactivity. The ability to import PET image data and to use the PET object as a source of radiation in the Monte Carlo simulation was a large factor in the selection of GATE as the modeling software of choice.

In addition to the ability of GATE to handle medical images, there is a pre-built version of GATE available. The program vGATE is a virtual machine that is configured to run GATE version 7.2. Using Oracle VirtualBox software, a virtual machine is created that runs Ubuntu Linux 14.04 LTS and GATE version 7.2. All Linux and GATE dependencies are pre-built which save considerable time in program setup.

1. Validation of GATE Using Dose Point Kernels for Monoenergetic Electrons

a) Introduction

It was necessary to evaluate the accuracy of GATE 7.2 for photon and electron transport and interactions. One method used was the calculation of dose point kernels (DPK). A dose point kernel is a representation of absorbed dose as a function of distance from an isotropic point source in a homogeneous medium[57]. They have simple and reproducible geometry. This facilitates comparison of results from different Monte Carlo programs. The dose point kernels calculated in this study were compared to those published in the literature.

b) Methods

A survey of the literature showed many reports on the calculation of dose point kernels for beta emitters [61]–[63]. However, only a few were found that actually contained numerical data [64]–[66]. In one of these publication, the Monte Carlo program FLUKA was used to produce DPKs for monoenergetic electrons in the energy range from 10 keV to 3 MeV in water and compact bone [65]. These same researchers also calculated DPK data for beta-emitting radionuclides of interest in medical applications. These radionuclides include Y-90, Sr-89, I-131, Sm-153, Lu-177, Re-186 and Re-188. The FLUKA results were then compared to DPKs generated by other Monte Carlo programs, specifically, PENELOPE v2008, ETRAN, GEANT4.8.2, and MCNPX 2.5.0. Comparison of GATE results to FLUKA results were especially beneficial in that

by comparison to FLUKA, a secondary comparison to other Monte Carlo programs was a result. All of these results proved to be useful in establishing confidence in the GATE 7.2 results. Another researcher, Seltzer, provided DPK data for monoenergetic electrons in the energy range 20 keV to 20 MeV [66]. This researcher used the Monte Carlo code ETRAN to calculate the scaled point kernel values. A subset of this data is available in Appendix C, Table C.1 of ICRU publication 56 [67].

In this study, GATE 7.2 was used to calculate the scaled dose point kernels for monoenergetic electrons in water. The method used was very similar to that outlined in the FLUKA study [65]. The scaled dose kernel was calculated by creating a set of concentric shells surrounding a monoenergetic point source. The concentric shells were of equal thickness. The outer surface of the largest shell was at a radius of $1.5 \cdot R_{CSDA}$. The range of electrons in water using the continuous slowing down approximation is the value R_{CSDA}. For an electron initial kinetic energy, the value of R_{CSDA} was found in the NIST ESTAR database [68]. There were 60 shells for each scaled dose point kernel. Each shell had a thickness of $0.025 \cdot R_{CSDA}$. The innermost shell had an inside radius of 0 cm and an outer radius of $0.025 \cdot R_{CSDA}$ centimeters.

For the calculation of each scaled DPK, a total of 10^7 primary particles were used in the GATE simulation. The energy that was deposited in each shell was tallied and reported in the results from GATE. Using 10^7 primaries resulted in a typical reported uncertainty of 0.1% or less for energy deposited in each shell for all shells within a radius of $0.9 \cdot R_{CSDA}$. The scaled dose point kernel can be expressed as shown in equation 3.2. In the literature, this formula is also referred to as the scaled point kernel. The scaled dose point kernel, F, is a function of the scaled radius, r/R_{CSDA}, which is dimensionless.

$$F(r/R_{CSDA}) = \frac{\delta E(r)/T_0}{\delta r/R_{CSDA}} \quad (3.2)$$

The scaled dose point kernel, F, is the fractional energy divided by the scaled shell thickness, $\delta r/R_{CSDA}$. The fractional energy for a shell is calculated as the energy deposited in the shell, $\delta E(r)$, divided by the total electron kinetic energy, T_0. For monoenergetic electrons, the total electron kinetic energy, T_0, in a simulation run is simply the initial electron kinetic energy, E_0, multiplied by the number of primary electrons used in the simulation, N_p.

$$T_0 = E_0 \cdot N_p \quad (3.3)$$

The scaled shell thickness is the shell thickness, δr, divided by R_{CSDA}. In the GATE simulations performed for monoenergetic electrons, each shell was $0.025 \cdot R_{CSDA}$ thick and was located between radius r and $r + \delta r$.

In GATE, for charged particle interactions, the user must set a range cut-off using the SetCutInRegion command. Below this threshold, secondary particles will not be generated. For the monoenergetic scaled DPK runs, range cuts were set to 0.005 mm for electrons. In water, this range corresponds to a kinetic energy of 4.3 keV. The lowest energy scaled DPK calculated was for 10 keV electrons.

Users of GATE have several choices regarding the statistical output. GATE can provide an output file for energy deposition and dose to voxels. Additional files can be selected that contain what the User's Manual describes as "dose squared" or "energy

squared". The "energy squared" value is not the square of the sum but is actually the sum of the squares of each individual energy deposition.

$$\text{"Energy Squared"} = \sum_{i=1}^{N} E_{k,i}^2 \tag{3.4}$$

Where $E_{k,i}$ is the energy deposited in voxel k in history i. The quantity N is the total number of primary particles [69].

$$s_{Ek} = \sqrt{\frac{1}{N-1}\left[\left(\frac{\sum_{i=1}^{N} E_{k,i}^2}{N}\right) - \left(\frac{\sum_{i=1}^{N} E_{k,i}}{N}\right)^2\right]} \tag{3.5}$$

In addition to the "energy squared" output file, there is an uncertainty file. This has an estimate of the relative uncertainty. The uncertainty reported by GATE is the ratio of the estimated standard error of the mean energy, s_{Ek}, divided by the mean energy [69]. For a given volume, the uncertainty for the energy deposited is also the same numerical value as the reported uncertainty for the dose. There are more detailed discussions of the statistical uncertainty in GATE [69]–[71]. It was confirmed by calculations that the statistical output is indeed being calculated by the method presented here.

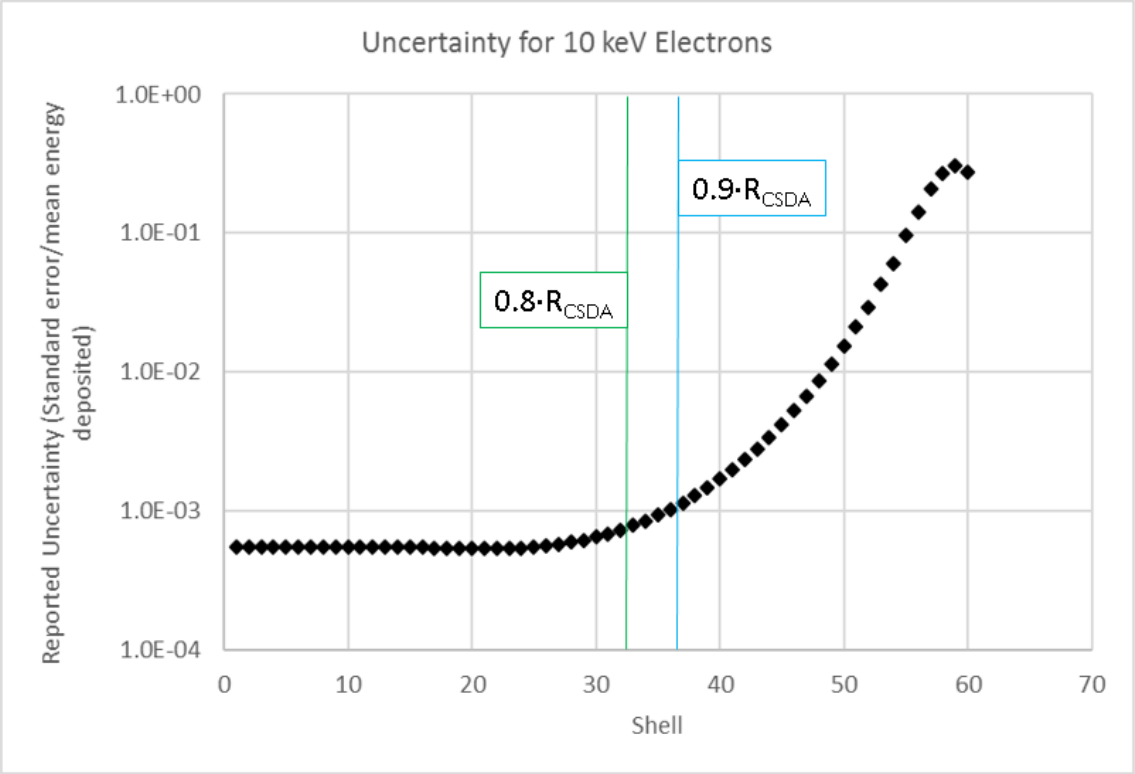

Figure 37: Uncertainty reported for energy deposited in shells of scaled dose point kernel for 10 keV monoenergetic electrons. $0.8 \cdot R_{CSDA}$ occurs at boundary between shells 36 and 37. The distance $0.9 \cdot R_{CSDA}$ occurs at the boundary between shells 36 and 37.

Figure 37 shows the uncertainty reported by GATE for a scaled DPK run with 10^7 simulated primary electrons. In this case, the distance, $0.8 \cdot R_{CSDA}$ occurs at the boundary between shell 32 and shell 33. The distance $0.9 \cdot R_{CSDA}$ occurs at the boundary between shell 36 and 37. The uncertainty is less than 0.1% at a distance less than $0.8 \cdot R_{CSDA}$ from the origin. Within the distance $0.9 \cdot R_{CSDA}$ the uncertainty is less than 0.12%. At distances past $0.9 \cdot R_{CSDA}$ the uncertainty increases rapidly.

c) Results

Using GATE, scaled dose point kernels were calculated for the following monoenergetic electron sources in water: 10 keV, 50 keV, 100 keV, 500 keV, 1 MeV and 2 MeV. When comparing different transport algorithms, differences often becomes more prominent at lower energies [65]. For this reason, the lower energy scaled DPK's were of particular interest. It is relatively straightforward to change the physics processes used for modeling within GATE. The physics processes are specified using the physics list builder command. The default physics constructor for Geant4 10.02 is "emstandard". The modeling can be switched to the Penelope physics models by using the physics list builder "empenelope".

A comparison study of the results generated with empenelope and emstandard_opt3 was performed. For the relatively high-energy electrons at 1 MeV, there was little difference between the calculated scaled DPK values. However, the calculated scaled DPK for 10 keV electrons were very different for the two physics packages.

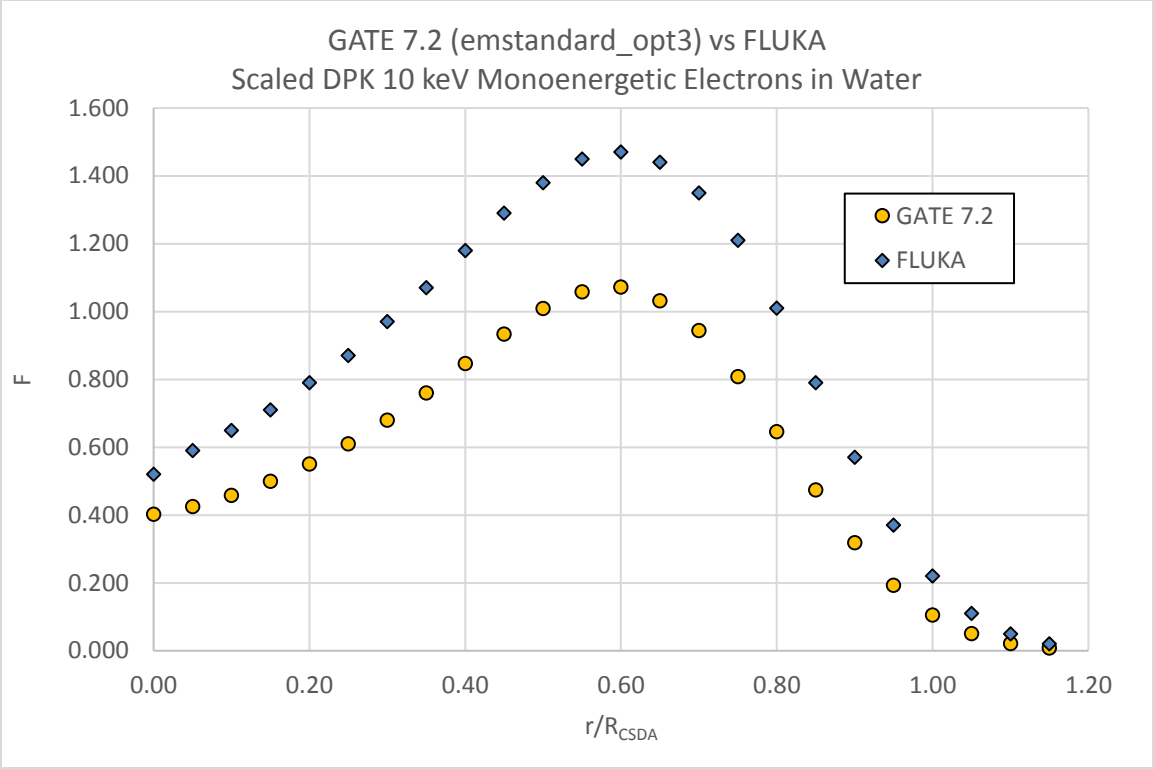

Figure 38: Scaled Dose Point Kernel for 10 keV Electrons. Results from GATE 7.2 compared to FLUKA. The physics package used was "emstandard_opt3".

In Figure 38, the 10 keV scaled DPK calculated with GATE using emstandard_opt3 is compared to the same scaled DPK calculated by Botta et al. using the FLUKA code.

The agreement between the 10 keV scaled DPK values was poor. In Figure 39, "empenelope" was used as the physics list builder replacing "emstandard_opt3". Otherwise, all other parameters were identical. The resulting scaled DPK for 10 keV electrons was in much better agreement with the scaled DPK calculated by FLUKA.

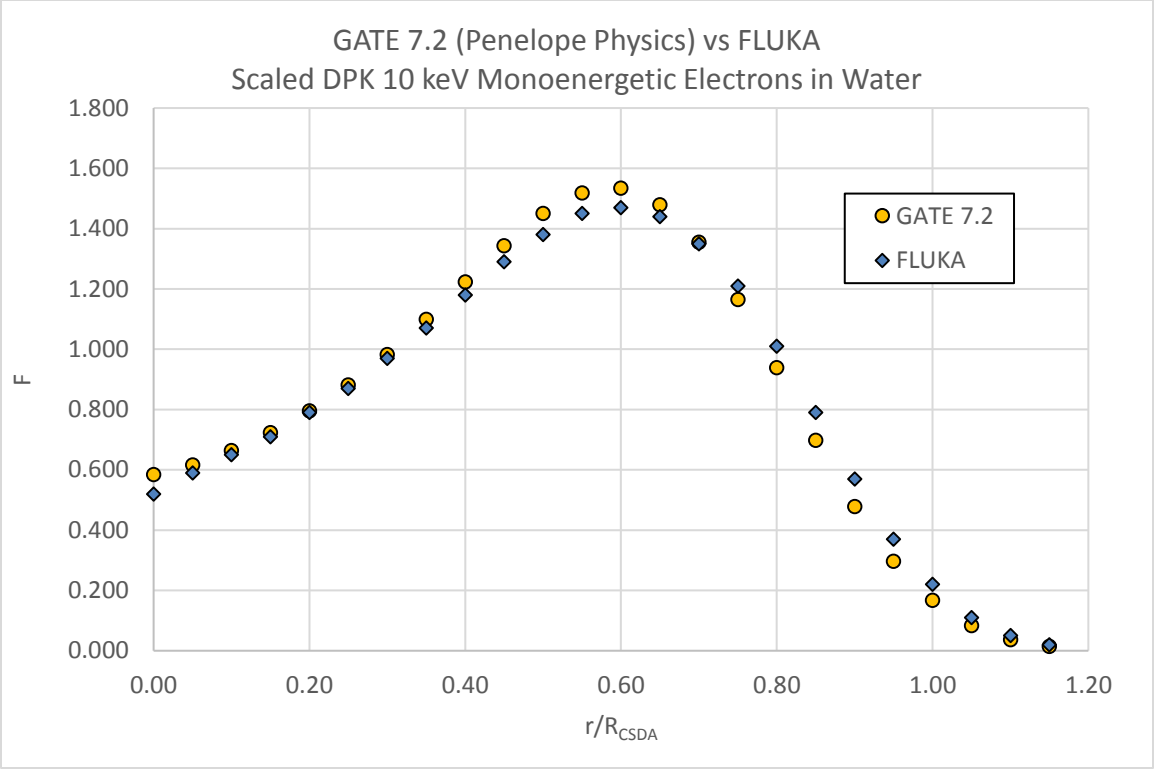

Figure 39: Scaled Dose Point Kernel for 10 keV Electrons. Results from GATE 7.2 compared to FLUKA. The Penelope physics package was used.

The FLUKA group had also published a comparison of their 10 keV scaled DPK results to other Monte Carlo programs including PENELOPE v2008, ETRAN, GEANT4.8.2, and MCNPX 2.5.0. The agreement among the different programs was acceptable. It was decided that "empenelope" would be used for the calculation of all subsequent electron scaled DPKs.

The following figures display the other monoenergetic scaled DPK's in water calculated by GATE and compared to results reported for FLUKA. Seltzer provides DPK values calculated with ETRAN for monoenergetic electrons [66]. These data were also used for comparison. The comparisons are shown in the following images.

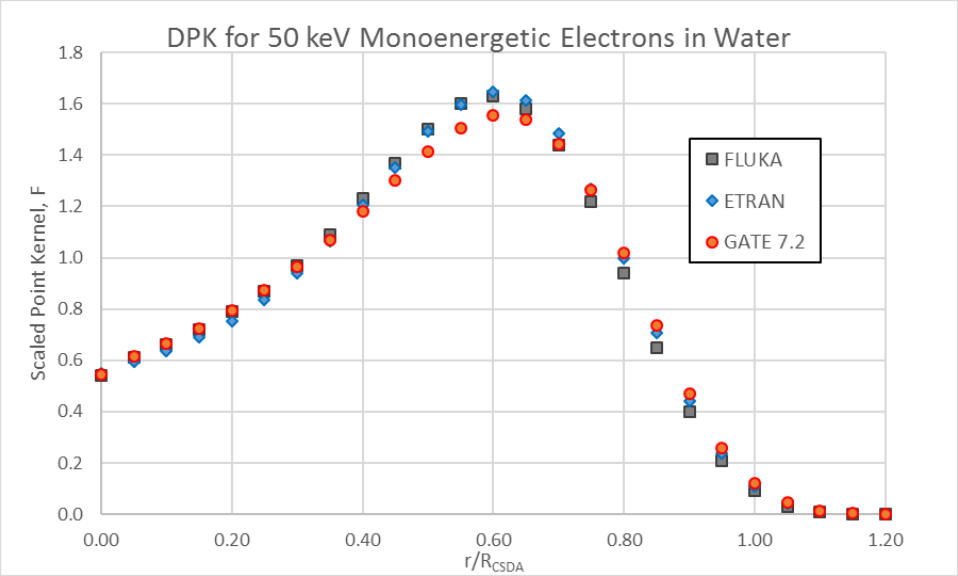

Figure 40: Scaled DPK for 50 keV monoenergetic electrons in water as calculated by GATE, ETRAN and FLUKA.

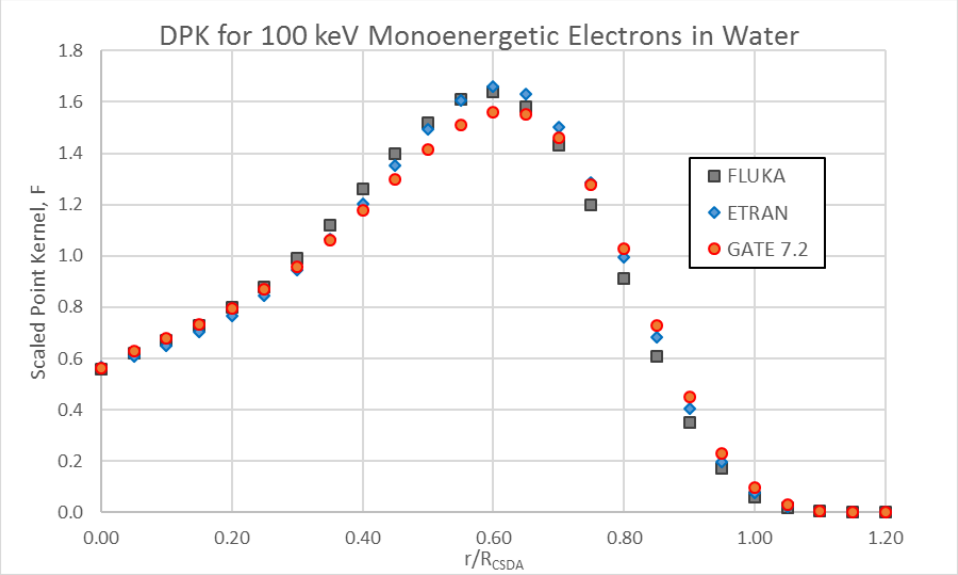

Figure 41: Scaled DPK for 100 keV monoenergetic electrons in water as calculated by GATE, ETRAN and FLUKA.

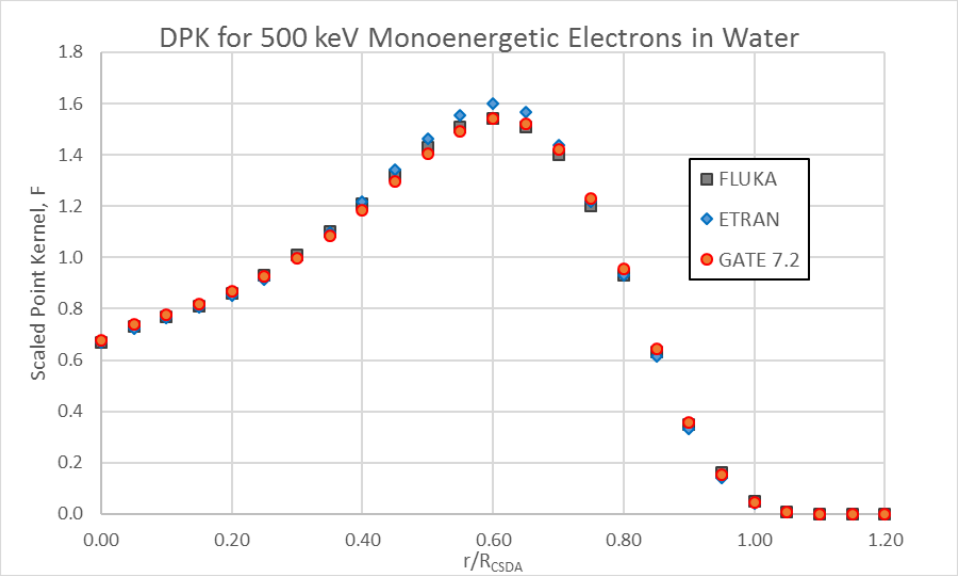

Figure 42: Scaled DPK for 500 keV monoenergetic electrons in water as calculated by GATE, ETRAN and FLUKA.

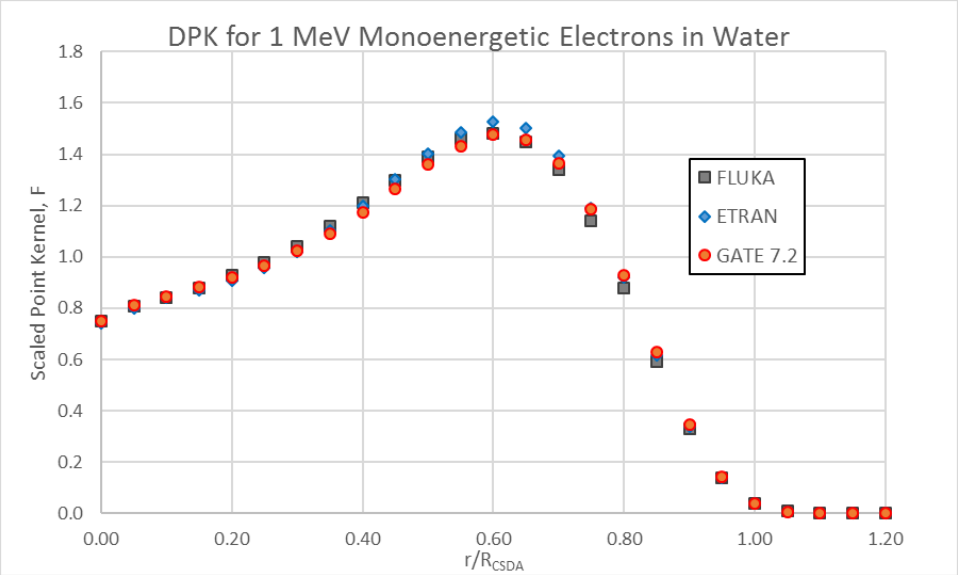

Figure 43: Scaled DPK for 1 MeV monoenergetic electrons in water as calculated by GATE, ETRAN and FLUKA.

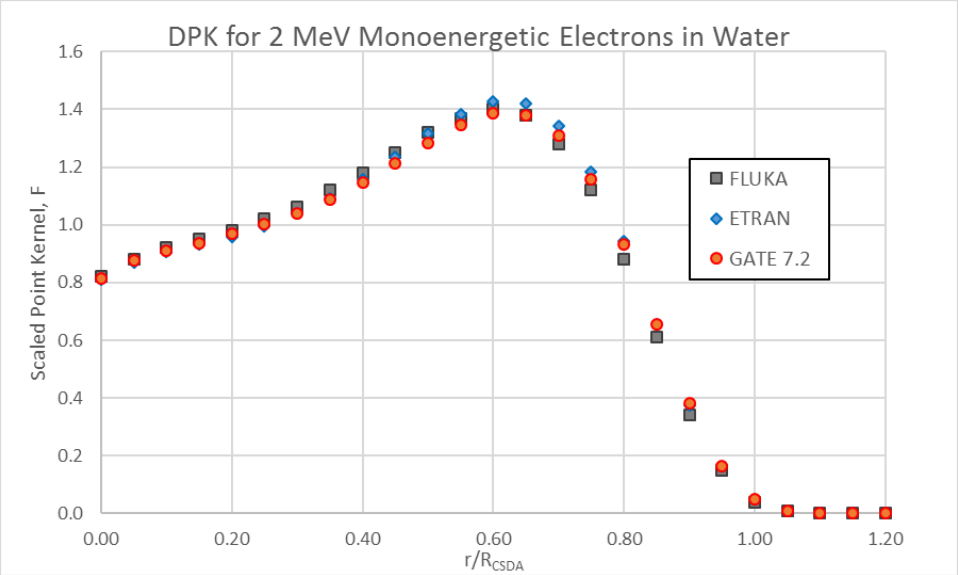

Figure 44: Scaled DPK for 2 MeV monoenergetic electrons in water as calculated by GATE, ETRAN and FLUKA.

Percent differences between GATE and FLUKA were calculated for values in which data was available. The percent difference was calculated using the formula below.

$$Percent\ Difference = 100 \cdot \frac{(F_G - F_F)}{min(F_G, F_F)} \tag{3.6}$$

F_F and F_G are the scaled point kernel values for a given shell. F_G was the value calculated by GATE 7.2 and F_F was calculated with FLUKA. The results are shown in Table 5. A comparison of this data to similar data in Botta et al. shows that the magnitude of the percent difference between the GATE results generated in this study are the same magnitude found when comparing scaled DPK values among other Monte Carlo programs [65].

Table 5. The percent discrepancy between GATE 7.2 results and FLUKA results [65]. Also shown is the average percent difference within $0.9 \cdot R_{CSDA}$.

Electron Kinetic Energy	Maximum Percent Discrepancy Within 0.8 R_{CSDA}	Maximum Percent Discrepancy Within 0.9 R_{CSDA}	Average Percent Discrepancy Within 0.9 R_{CSDA}
10 keV	12.3	-13.2	4.3
50 keV	-6.2	13.5	3.4
100 keV	-7.7	19.6	5.0
500 keV	2.4	2.8	1.4
1 MeV	4.0	6.6	2.0
2 MeV	3.5	7.7	2.3

d) Conclusions

What was consistent throughout the literature was that there was never perfect agreement between different Monte Carlo programs. There was acceptable agreement between monoenergetic scaled DPKs calculated with GATE 7.2 and other DPK values presented in the literature. This confirms that electron transport and interactions are being handled adequately. These results verify that the energy deposition in thin water targets is accurately modeled.

2. Calculation of Dose Point Kernel for Y-90

A necessary step prior to calculation of the dose point kernel for a beta-emitting radionuclide is to find the energy spectrum for the emitted beta particles. Several candidate spectra were found. A Y-90 beta spectrum evaluated in this study was

published by Eckerman et al. [72]. Subsequently, another Y-90 beta spectrum was found in ICRU publication 56 [67]. Another Y-90 beta spectrum was generated by Dr. Doug Simpkin. This was provided via personal communication by Dr. Reed Selwyn.

An initial survey of the data showed that the number of data points in each spectrum differed. The spectrum from Eckerman had 20 energy bins. The spectrum from ICRU 56 had 40 energy bins. The spectrum from Simpkin had 200 energy bins. To compare the spectra, the data was rebinned and normalized. Specifically, the 40 bins of the ICRU 56 data were collapsed into 20 bins and renormalized. Likewise, for the Simpkin data, the 200 energy bins were collapsed into 20 bins and renormalized. The comparison of the data found that the agreement between the spectra was good.

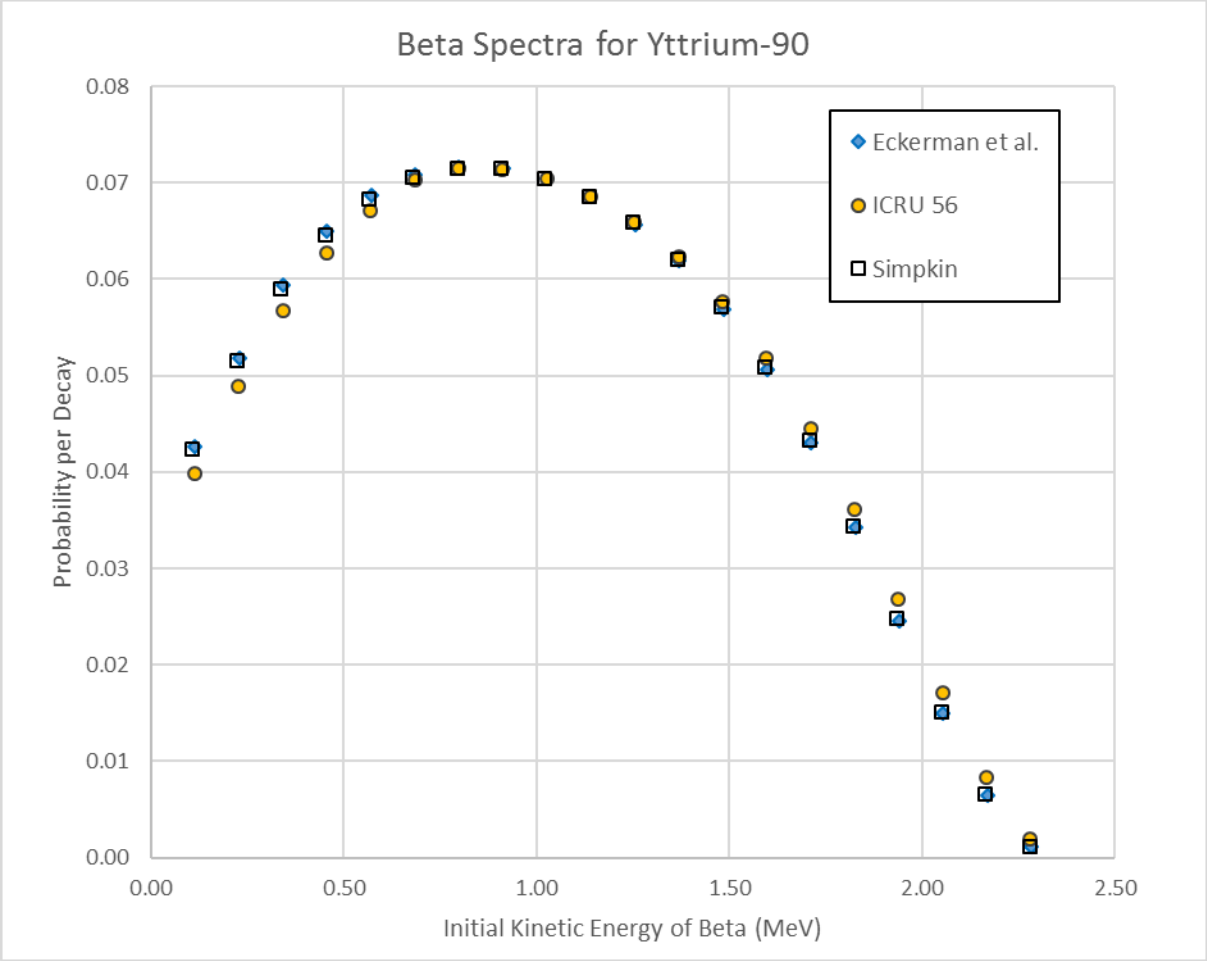

Figure 45: Comparison of beta spectra for Y-90. These were the three spectra that were considered for use in the subsequent Y-90 simulations. For purposes of comparison, the ICRU 56 data and the data from Simpkin were rebinned.

The primary difference between the spectra is in the energy resolution. The effect of the different energy resolution on the DPK calculation was examined. The beta energy spectrum from Simpkin is essentially the same as the beta energy spectrum from Eckerman. The spectrum from Simpkin has 200 data points while that of Eckerman has 20.

Figure 46 shows the Y-90 DPK calculated with the 20 bin Y-90 spectrum from Eckerman et al. and the Y-90 DPK calculated with the 200 bin Y-90 spectrum from Simpkin. Other than the different beta spectra, the input files for GATE were identical. The result is essentially the same DPK. Within $X_{90,\ the}$ maximum difference between the two spectra was less than 0.6%. X_{90} is the radius of a sphere in which 90% of the energy is deposited [65].

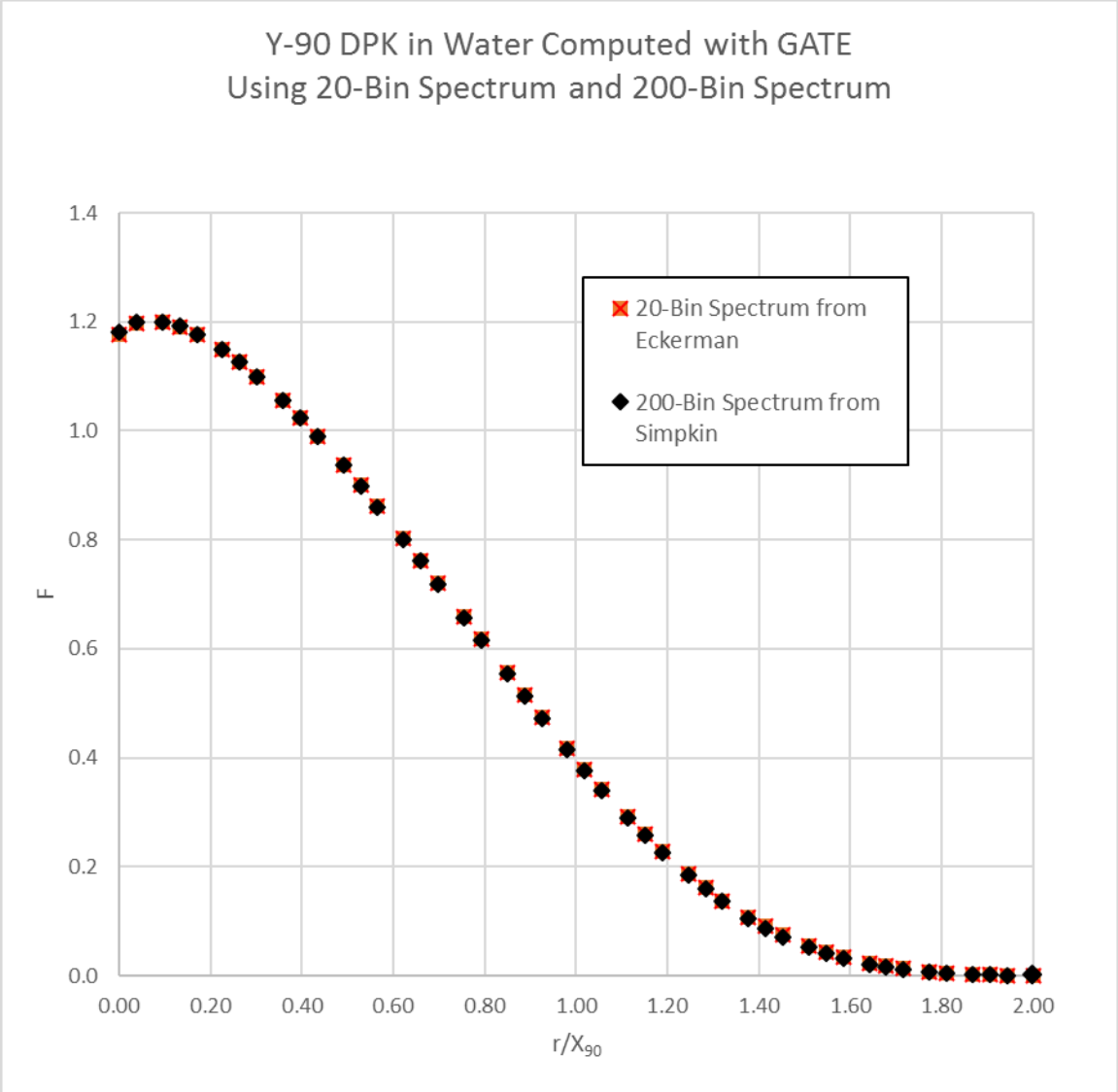

Figure 46: Scaled DPK for Y-90 calculated with 20 point Y-90 beta spectrum from Eckerman et al. and a 200-point beta spectrum from Simpkin. Within X_{90}, the maximum difference between the two DPK was less than 0.6%.

The scaled dose point kernel for Y-90 was calculated using GATE. To facilitate comparison, the same geometry that was used for calculation of the Y-90 scaled DPK with FLUKA was used for GATE [65]. The geometry for the Y-90 DPK was similar to the geometry used for the monoenergetic electrons. A simulation was created of an

isotropic point source of Y-90 placed in water. A series of concentric shells were defined about the point source and the energy deposited in each shell was calculated using GATE. The shell thickness was set to 0.1 mm which is approximately $0.02 \cdot X_{90}$. The inner surface of the outer most shell was at $2 \cdot (r/X_{90})$. The result was 107 shells. Within the supplemental material of their paper, Botta et al. provide values for the scaled dose point kernel, F, for approximately half of their shells. Simpkin and Mackie also provided data for scaled point kernels using EGS4 [61]. The data for the three dose point kernels is plotted in Figure 47.

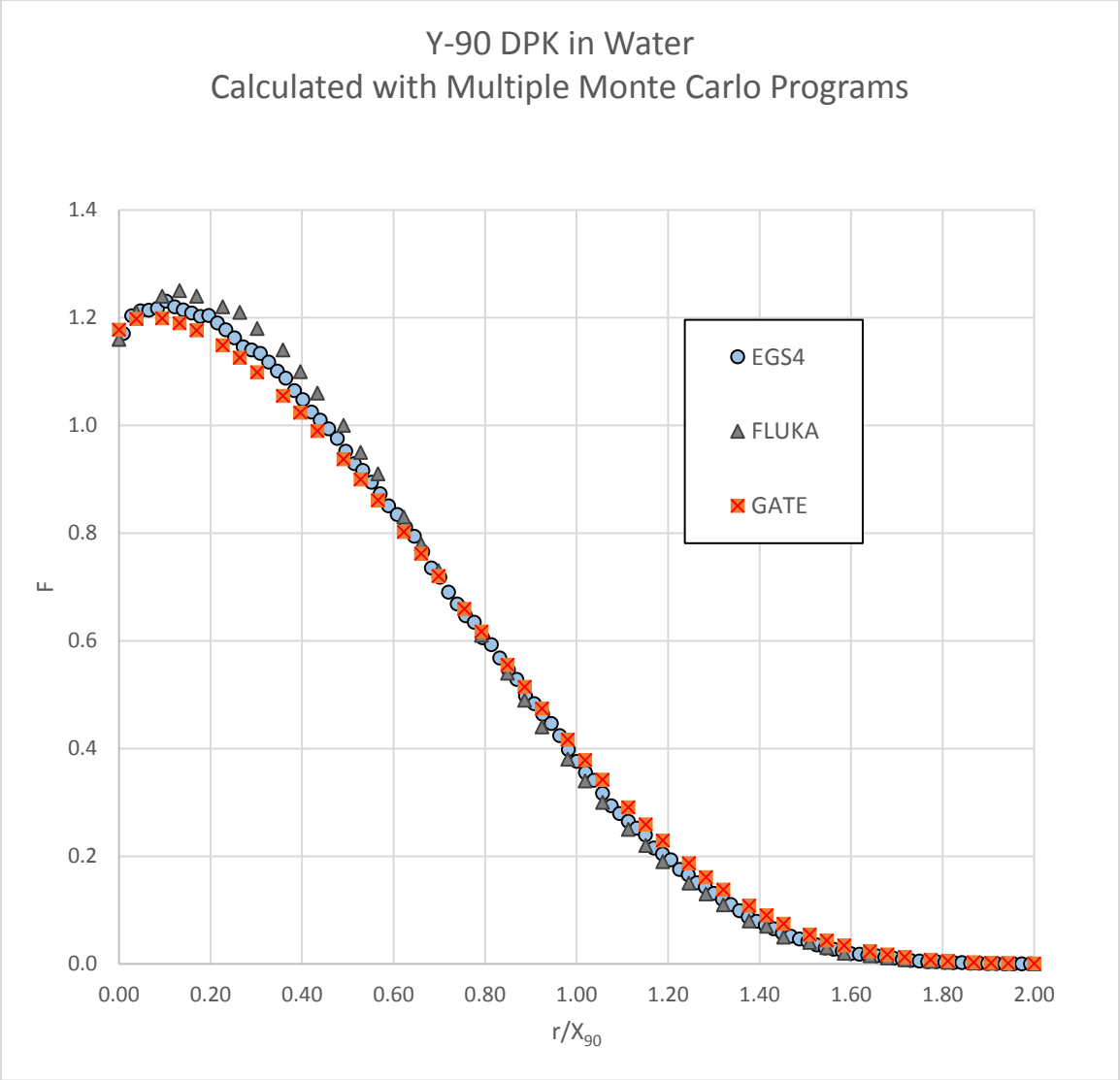

Figure 47: Scaled DPK for Yttrium-90 as calculated with GATE, FLUKA and EGS4.

3. Validation of GATE and Image-Based Dosimetry

Experiments were performed to assess the use of GATE and PET data for image-based dosimetry. PET images were acquired with fluorine-18. This is the same radionuclide used to label the surrogate microspheres.

a) Case 1: Homogeneous water-filled phantom

In the United States, clinically used PET scanners are coupled to a Computed Tomography (CT) scanner to form a dual-modality PET/CT. The CT provides high-resolution anatomic imaging which aids in the localization of PET activity within the patient. The CT also provides important attenuation properties of the patient. Each volume element, voxel, in a CT image has an associated Hounsfield Unit (HU). The value of the HU for a voxel is measured by the transmission of the x-ray beam through the material in the voxel. The gray scale map of the HU values is the data used to produce the CT images. The formula for the Hounsfield Unit is shown below. The linear attenuation coefficient of the voxel is μ. The linear attenuation coefficient for water is μ_{water}. For a water-filled voxel, the Hounsfield Unit value will be close to zero. The electron density of the material in a voxel is the primary determinant for the attenuation properties of the voxel. In general, for material denser than water, the HU value will be greater than one. For material less dense than water, the HU will be less than one. The CT images are a 3-dimensional map of the attenuation properties of the object being scanned.

$$HU = 1000 \times \frac{\mu - \mu_{water}}{\mu_{water}} \tag{3.7}$$

The CT data is used to correct the PET images for attenuation. When a positron undergoes annihilation with an electron, two photons are formed each with 511 keV of energy. These photons travel in opposite directions. For a "true" count to be recorded by

the PET imaging system, both photons must be recorded by detectors within the ring of the PET scanner. Thus, both photons must make it out of the object being scanned. There is a significant probability that attenuation can occur to the photons as they travel through material. The probability of attenuation depends on the material and path length through the material being traversed. Annihilation photons born deep in the patient have a higher probability of attenuation than annihilation photons produced near the surface of the patient. The CT data is used to correct the PET images for attenuation. Typically, two set of clinical PET images are produced for each patient, an attenuation-corrected set of images and a non-attenuation-corrected set of images.

For the Siemens PET/CT scanners used in this study, the vendor provides a "uniformity" phantom for use in PET quality control. The uniformity phantom is a hollow, plastic cylinder which is filled with water. The vendor states that the volume of the cylindrical phantom is 6.283 liters. When preparing the phantom for imaging, a positron-emitting radionuclide such as F-18 is carefully measured in a dose calibrator. The activity of the F-18 and the time of measurement are recorded. The radionuclide is then added to the water in the phantom and mixed. The result is a cylinder containing a uniform distribution of a known activity concentration. The activity concentration is typically expressed in Becquerel per milliliter (Bq/mL). In the experiment presented here, the activity injected into the uniformity phantom was 1.624 mCi (60.08 MBq) of F-18.

The dose calibrator used to measure the F-18 was a Capintec 15R (SN#152530) located in the hot lab at University of New Mexico Hospital. The instrument was a clinically used dose calibrator that met regulatory quality control. The F-18 calibration

number had been previously set using the NIST traceable Ge-68/Ga-68 source described in the radiolabeling section. The calibration sheet for the source is presented in Appendix A.

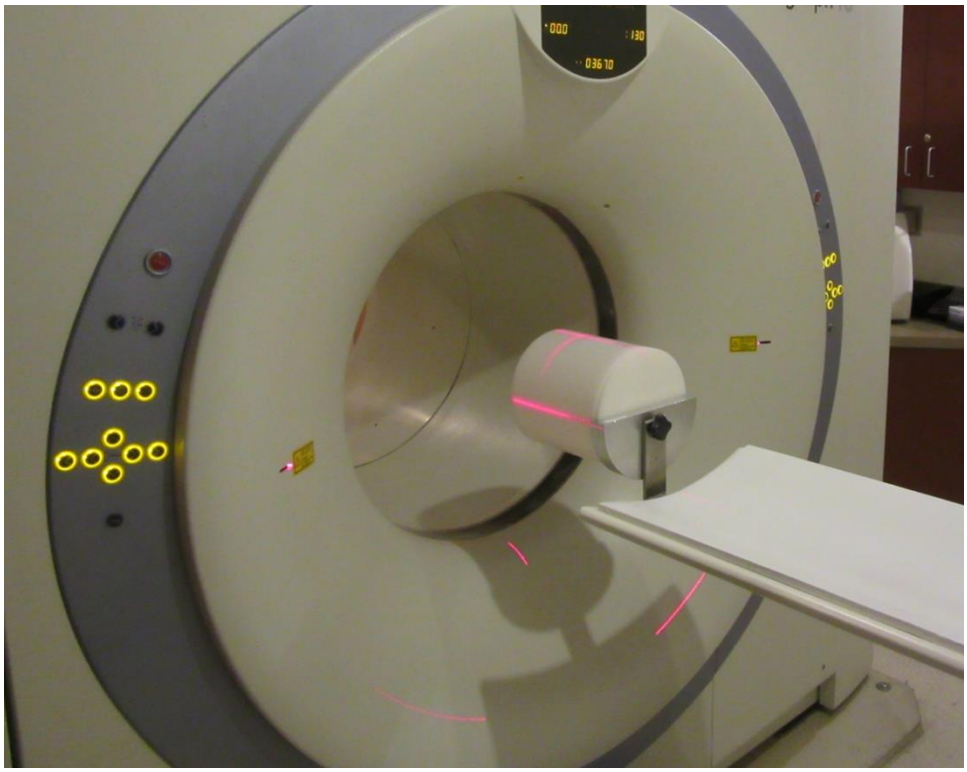

Figure 48: Cylindrical uniformity phantom mounted on bracket at end of patient table. The uniformity phantom is used for quality control of the PET/CT scanner. Phantom volume is 6.283 liters. Scanner is a Siemens Biograph 16 PET/CT.

Prior to scanning, the phantom was mounted on to the holder at the end of the patient bed as shown in Figure 48. The whole body scanning protocol that would be used on a patient was used to scan the phantom. A scout image was acquired with CT. The PET acquisition was set for a stop condition of 100 million counts per bed position. Two bed positions were used to completely image the phantom in the axial direction. The

phantom was then scanned using CT. The scan parameters were 120 kVp, 48 mA and a tube rotation time of 0.5 seconds. The images were 3 mm thick reconstructed using the B31f reconstruction kernel. The PET scan was then started and the start time was recorded. The PET was acquired with a 168 x 168 matrix and a Gaussian convolution kernel with FWHM of 5 mm. The PET images were reconstructed with a slice thickness of 3 mm using an OSEM2D iterative reconstruction algorithm using 2 iterations and 24 subsets. The CT data was used to produce attenuation-corrected PET images.

The resulting attenuation-corrected PET and CT image DICOM series were imported into the program VV and converted into MetaImage format. The MetaImage PET and CT image series were then imported into GATE. The CT series was used as the "patient". In the GATE simulation, the attenuation properties in a voxel is determined by the Hounsfield Unit (HU) for that particular voxel. The HU values are determined by the CT scan as described previously.

The PET image was imported into GATE and converted into a voxelized source. The activity of the simulated source was independent of the activity used to produce the PET image. In the GATE simulation, it is possible to use an activity that is different than the activity used to produce the PET images. It was also possible to change the radionuclide to one different from the radionuclide used to acquire the PET image. For instance, in this case, 1.624 mCi of F-18 was used to produce the PET images. Within GATE, the source was then assigned an activity of 30.1 Bq of Y-90. The assigned activity was determined by the number of primary particles used in the GATE simulation. In this case, the primary particles were electrons created using the Y-90 energy spectrum.

In this way, the voxelized source within GATE was converted to a uniform cylinder with a volume of 6283 mL containing 30.1 Bq of Y-90.

The PET images were essentially a three-dimensional map of the relative F-18 activity within the phantom. This relative activity map was converted into a voxelized, three-dimensional map of the relative Y-90 activity. This was done by setting the source emission to be electrons with kinetic energy determined by the Y-90 beta energy spectrum. For this initial experiment, the number of electrons emitted was set to 10^7. For the Monte Carlo run, the number of primary particles is equivalent to the integrated activity, A_c. For a permanent implant, A_c is the total number of disintegrations between calibration time t = 0 and t = infinity is given by the following equation. The integrated activity A_c, is equivalent to the cumulated activity $\tilde{A}_h$ in the MIRD schema.

$$A_c = \int_0^\infty A(t)dt \tag{3.8}$$

$$A_c = A_0 \cdot T_{1/2} \cdot \frac{1}{\ln(2)} \tag{3.9}$$

If A_c is set to 10^7 and the half-life of Y-90 is 230550 seconds, we can solve for A_0:

$$10^7 = A_0 \text{ x } (230550 \text{ seconds}) \text{ x } 1.443$$

$$A_0 = 30.1 \text{ disintegrations/second} = 3.01 \text{ x } 10^{-8} \text{ GBq}$$

The following relation can be used to calculate the absorbed dose delivered to the phantom from 30.1 Bq of Y-90. Recall the volume of the phantom is 6.283 liters of water, thus the mass of the phantom is 6.283 kg.

$$Dose_{target}(Gy) = 49.38 \cdot \left[A_0(GBq)/Mass_{target}(kg)\right] \quad (3.10)$$

Thus,

$$Dose_{Target}\ (Gy) = 49.38 \times [3.01 \times 10^{-8}\ GBq/6.283\ kg] = 2.363 \times 10^{-7}\ Gy$$

A GATE run was performed using 10^7 primary electrons. The 20 bin beta spectrum from Eckerman et al. was used to produce the simulated beta particles [72]. The physics package was "empenelope". Total run time was 12489 seconds (3.47 hours) on a laptop with an Intel Core i5-4300U CPU at 1.90 GHz. The output of the GATE run was a 3D dose map of the phantom. The tomographic dose image was opened in 3DSlicer software version 4.6.2. A large volume of interest (VOI) was placed into the center of the phantom and the resulting dose in the VOI was found to be:

$$2.337 \times 10^{-7}\ Gy \pm 0.232 \times 10^{-7}\ Gy$$

The percent difference between the calculated absorbed dose and the dose measured with the VOI was:

$$100\% \times [(2.337-2.363)/2.363] = -1.1\% \pm 9.8\%$$

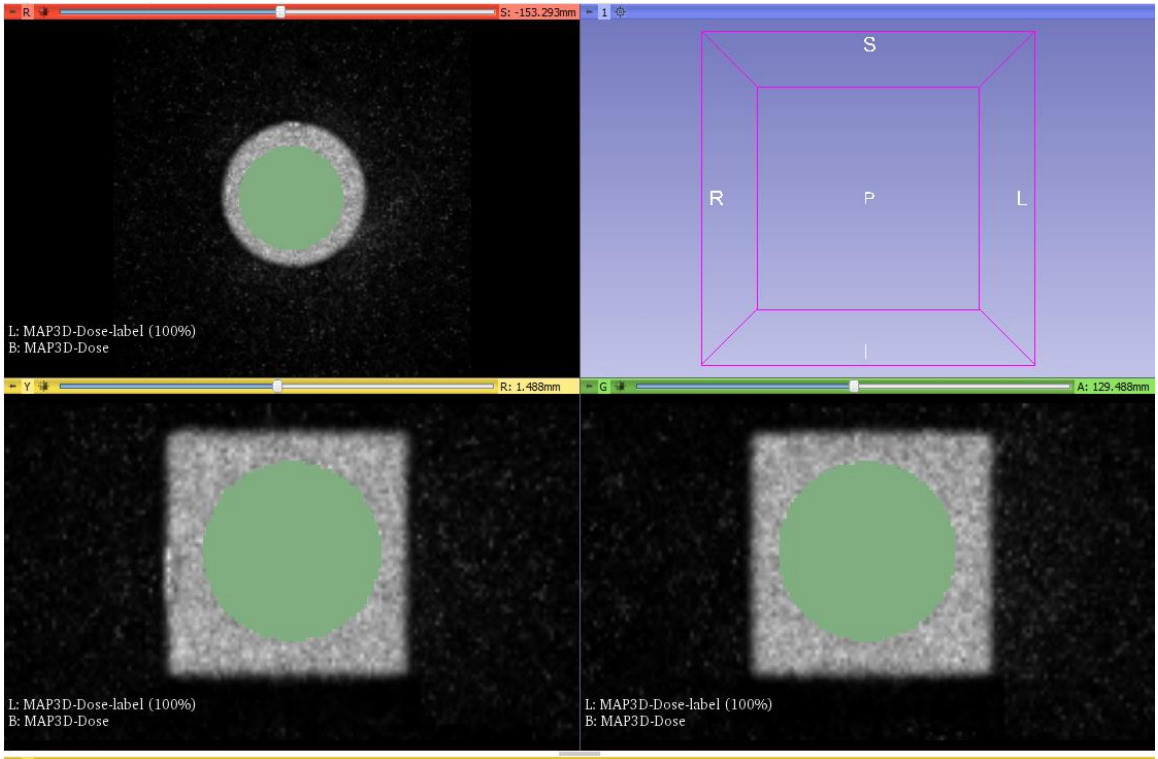

	A	B	C	D	E	F	G	H	I
1	Type	Index	Count	Volume mm^3	Volume cc	Min	Max	Mean	StdDev
2	background	0	2257318	68274373.0419	68274.3730419	0.0	3.64755180726e-07	2.57039087254e-08	5.35008087352e-08
3	tissue	1	57050	1725522.49264	1725.52249264	1.26867178096e-07	3.65047355899e-07	2.33712669065e-07	2.61996357104e-08

Figure 49: Voxelized dose map of uniform PET phantom displayed in 3DSlicer. The green sphere is the volume of interest (VOI). The mean dose in the VOI is 2.337×10^{-7} Gy ± 0.262×10^{-7} Gy.

The results of this experiment confirms that GATE can be used to produce accurate image-based dosimetry. The use of more primary particles in the GATE simulation would reduce the associated error at the cost of increased computing time.

b) Case 2: Inhomogeneous water-filled phantom

Image-based dosimetry in the case of a homogeneous phantom has been shown to be accurate. The case of an inhomogeneous phantom is presented next. The activity in a PET source must be enough to produce an acceptable image. Beyond this requirement,

the activity used to produce the PET image is not used in the dosimetry calculations. The issue addressed with the study of the inhomogeneous phantom was if the relative activity distribution is maintained in the voxelized source. For instance, if a region had twice the amount of F-18 than another region, the 2:1 ratio in activities should be maintained throughout the Monte Carlo simulation. If the F-18 was replaced with Y-90, the resulting dose to the two regions should still maintain the 2:1 ratio.

The initial step was to acquire a PET/CT image of the phantom. In this case, the PET/CT was acquired during the 2016 annual survey of the Siemens mCT PET/CT at UNM Outpatient Surgery and Imaging Services. The PET acquisition was performed using the clinical whole body PET protocol. A 200 x 200 matrix was used with a Gaussian convolution kernel with a FWHM of 5 mm. The time per bed position was set to 1 minute. The slice thickness was 5 mm. The reconstruction used OSEM iterative reconstruction with 3 iterations and 21 subsets. This included high-resolution point spread correction (TrueX) and Time-of-Flight (TOF) PET imaging. CT imaging was done with 170 kVp, 73 mAs, tube rotation time of 0.5 seconds and a helical acquisition with a pitch of 0.8. The CT images were reconstructed using the B19f convolution kernel. The PET images were corrected for attenuation using the CT data.

Figure 50: The ACR PET phantom. The lid contains objects that enable measurement of the imaging capability of a PET/CT scanner. A positron-emitting radionuclide is added to the bulk fluid in the phantom and also to the 'hot' cylinders in the lid. The hot cylinder-to-bulk contrast ratio is 2.5:1

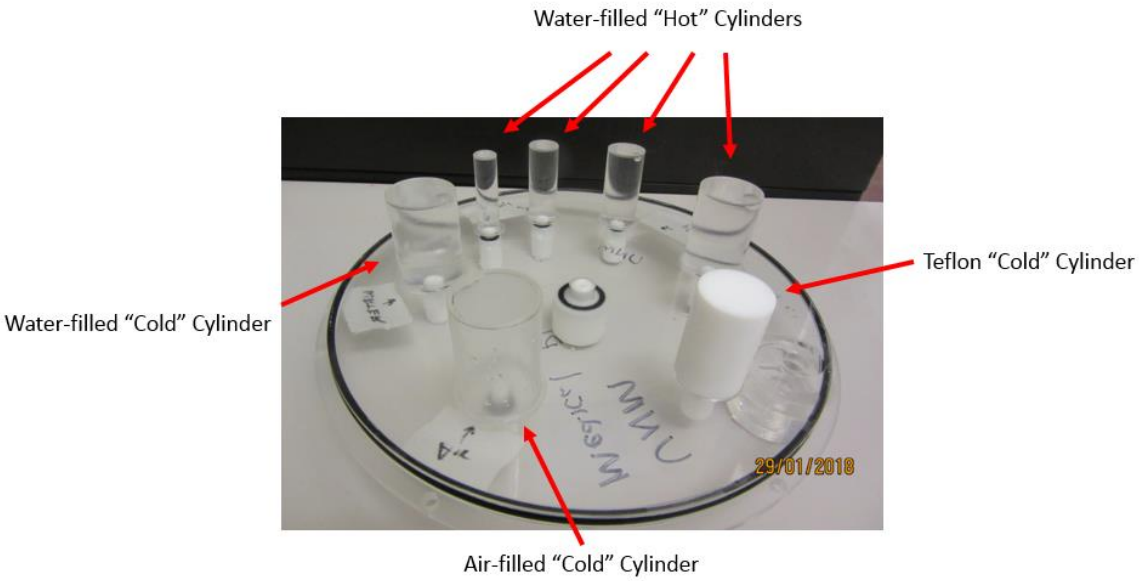

Figure 51: Underside view of the lid for the ACR PET phantom. The "hot' cylinders are filled with a positron-emitter and water. The "cold" cylinders are free of activity.

The American College of Radiology (ACR) requires a specific model of PET phantom is to be used for ACR PET accreditation. The PET phantom is an acrylic cylinder with an inner diameter of 20.4 cm. The cylinder is filled with water. Prior to scanning, a small amount of positron-emitting radionuclide is added to the bulk fluid to produce a "warm" background. Within the large cylinder are wedge-shaped groups of rods. The rods are made of solid acrylic and during imaging are free of radioactivity. These "cold" rods are used to determine the spatial resolution of the PET camera.

The lid of the ACR PET phantom contains four fillable cylinders. These are the "hot" cylinders. Prior to use, the hot cylinders are filled with a solution of positron-emitter and water. The ACR provides a standard set of instructions for determining the activity concentrations used to fill the cylinders in the lid and the bulk fluid. The activity amounts for the cylinders and the bulk fluid is designed to be near a 2.5:1 ratio. This contrast ratio is representative of a hot lesion in a liver. The diameters of the four hot cylinders are 8 mm, 12 mm, 16 mm and 25 mm [55]. There are also three "cold" cylinders that are free of radioactivity. These are cylinders containing water, air and Teflon.

The attenuation-corrected PET images were used as the voxelized source in a GATE simulation. The CT provided the material densities so that absorbed dose could be calculated. The attenuation-corrected PET, non-attenuation corrected PET and CT series of DICOM images were exported from the scanner. The open-source software "VV" was used to convert the DICOM series into the MetaImage (*.mhd and *.raw) format. The image below is a screen shot of the VV program with the CT image

displayed in MetaImage format. In this case, the matrix size of the CT image was 512 x 512 x 75. The size of the image was 500 mm x 500 mm x 225 mm.

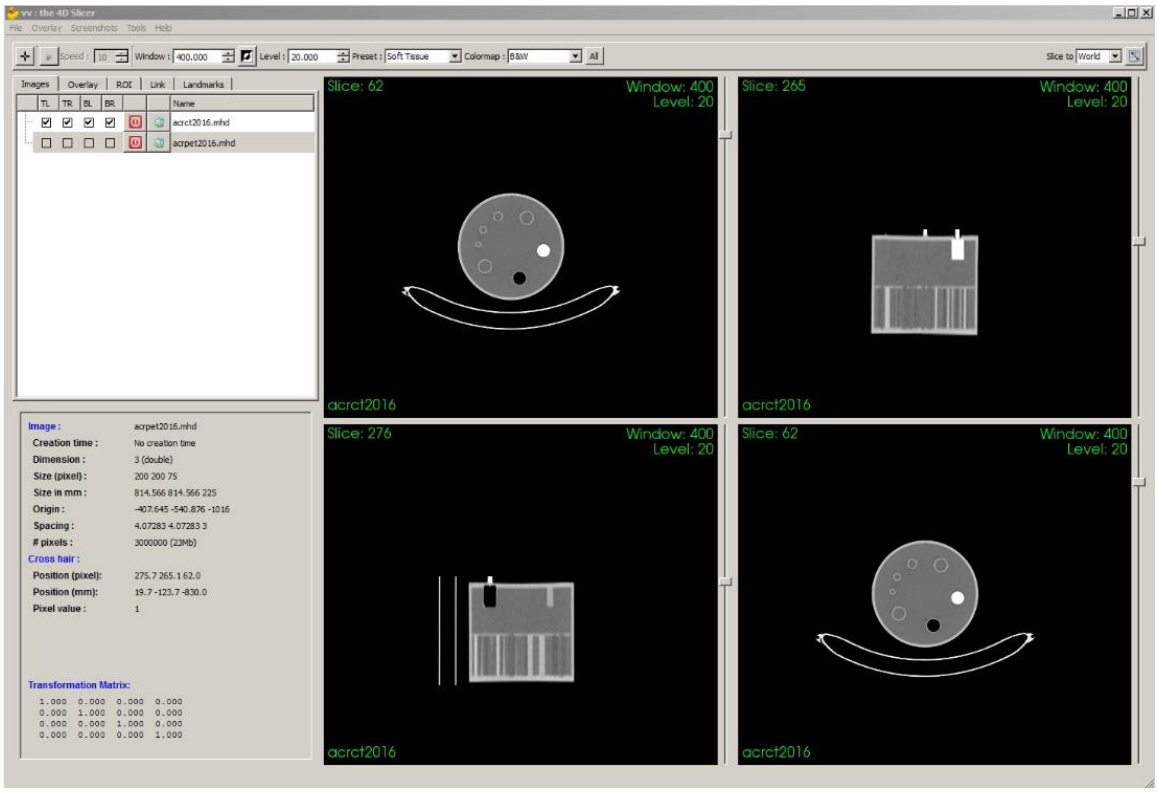

Figure 52: CT image of ACR PET phantom displayed in VV. In the axial slice, the white object at the 3 o'clock position is the Teflon cylinder. The air-filled cylinder is at the 6 o'clock position.

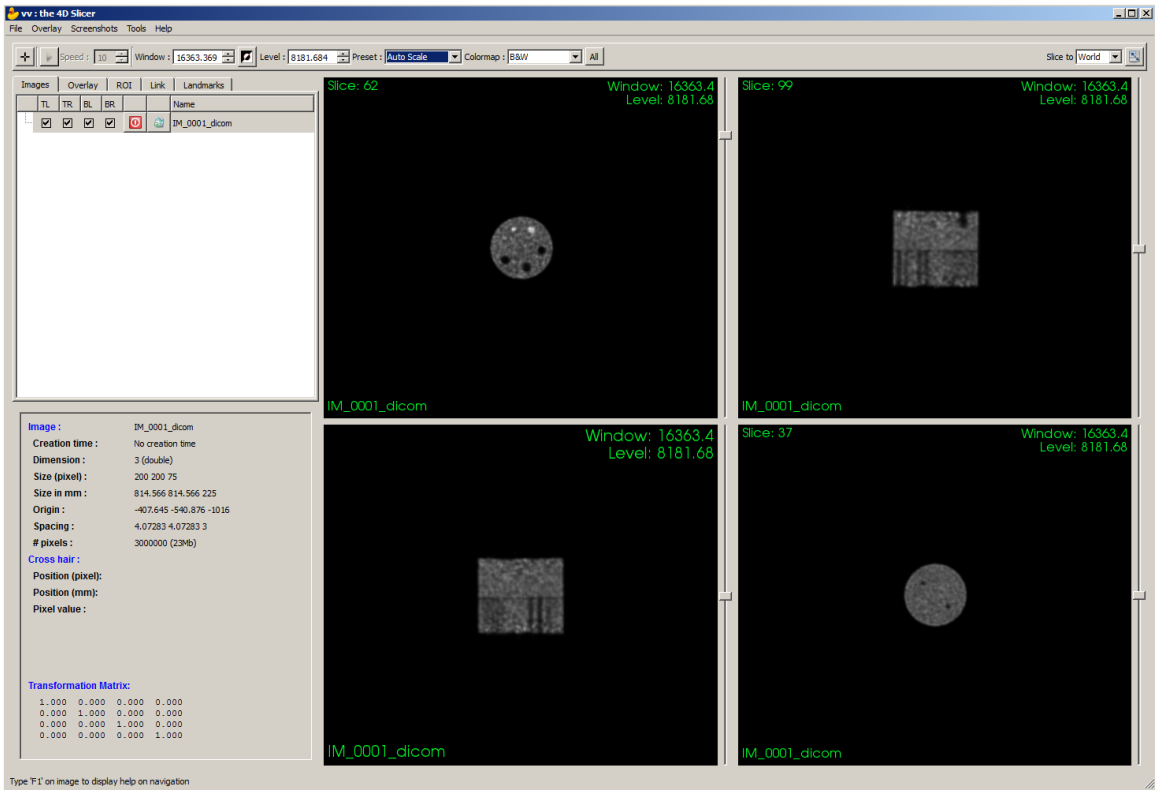

Figure 53: PET image of ACR PET phantom displayed in VV. Bright object at 1 o'clock is 25 mm diameter hot cylinder.

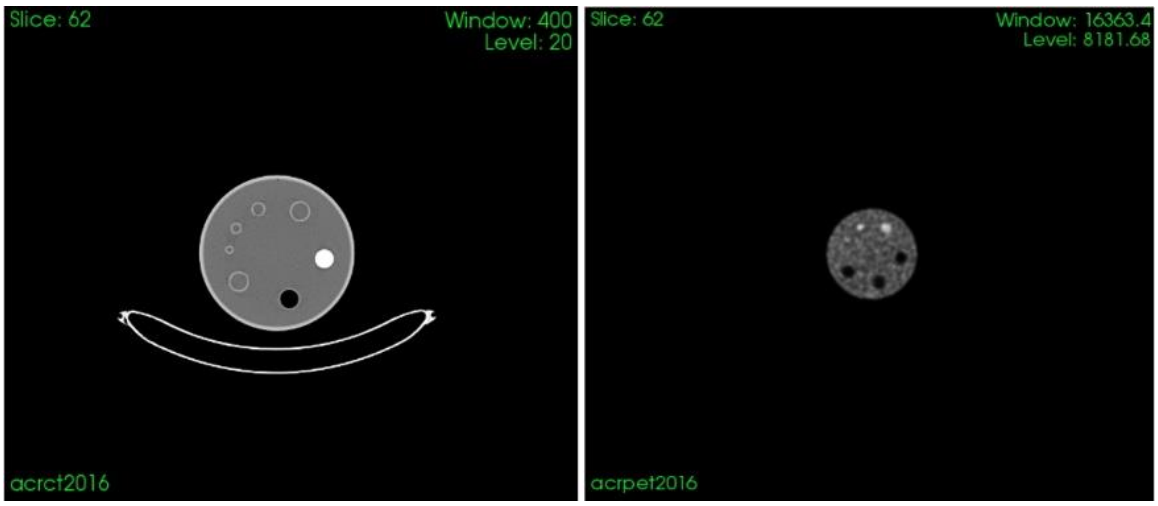

Figure 54: Side by side comparison of CT (left) and PET (right) of slice 62 through ACR PET phantom.

The attenuation-corrected PET DICOM series were imported into VV and converted into MetaImage (*.mhd and *.raw) format. The PET image had a matrix size of 200 x 200 in the axial plane and 75 voxels in the z-axis which is parallel to the patient bed and the axis of the phantom cylinder.

A way to check the PET and CT registration was to do a GATE run with a few thousand monoenergetic electrons. Using relatively low-energy electrons ensured that the particles did not move far from the point of origination. Figure 55 shows the PET phantom with the several thousand electrons being produced. The registration was found to be acceptable.

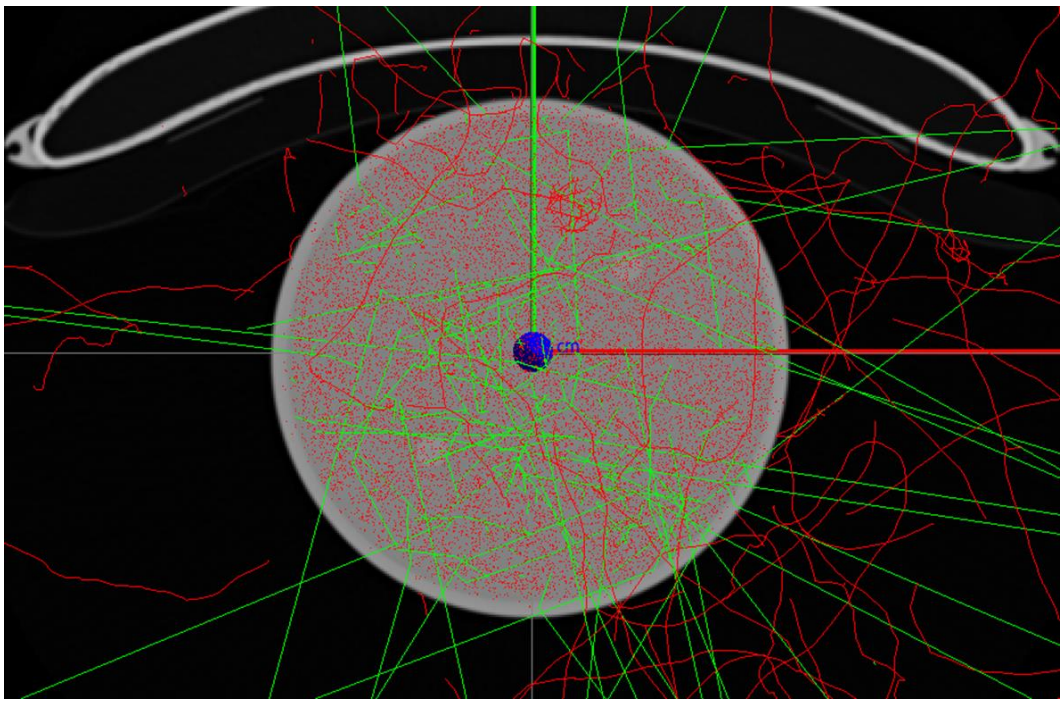

Figure 55: ACR PET phantom in GATE. The slice shown is through the uniformity section of the phantom. The registration of the PET and CT images can be checked visually by running the simulation with a few thousand monoenergetic electron with relatively low energy. Here the initial kinetic energy of the electrons is 200 keV.

The GATE run was performed with the Y-90 beta spectrum from Eckerman et al. The empenelope physics package was used. The SetCutInRegion length for electrons was set to 0.005 mm. The total number of primary electrons generated was 10^7. The run time for the simulation was 12063 seconds (3.35 hours). Output included a tomographic map of the energy deposition in the phantom and a tomographic map of the absorbed dose in the phantom. Figure 56 shows the same slice through the cold rod region of the phantom in the original F-18 PET image (left), in the Y-90 energy deposited image (middle) and the Y-90 absorbed dose image (right). The number of cold rods that can be visualized was the same in all three images. This indicates that the spatial resolution was maintained during the conversion of the original F-18 PET image into the Y-90 PET image. As expected the relative activity concentration of the Y-90 has produced an energy deposition and absorbed dose distribution that closely matches the activity distribution of the surrogate F-18 activity in the original PET data. The surrogate F-18 activity has been used to accurately map the absorbed dose produced by the Y-90.

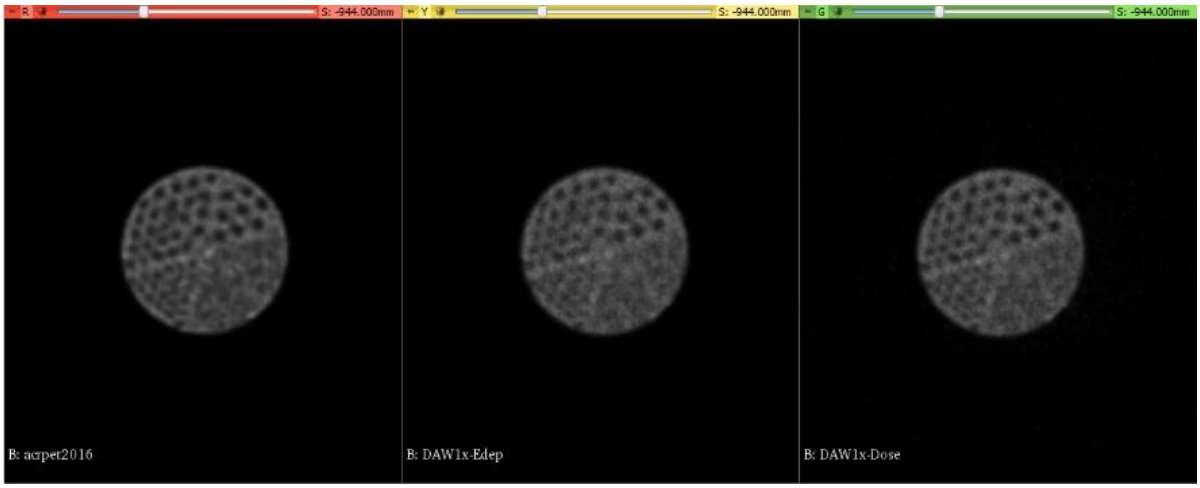

Figure 56: Comparison of F-18 PET (left), Y-90 Energy Deposited (middle) and Y-90 Absorbed Dose (right). Slice was through cold rods. Note that the number of rod groups visualized was the same in all three images. The spatial resolution has been maintained.

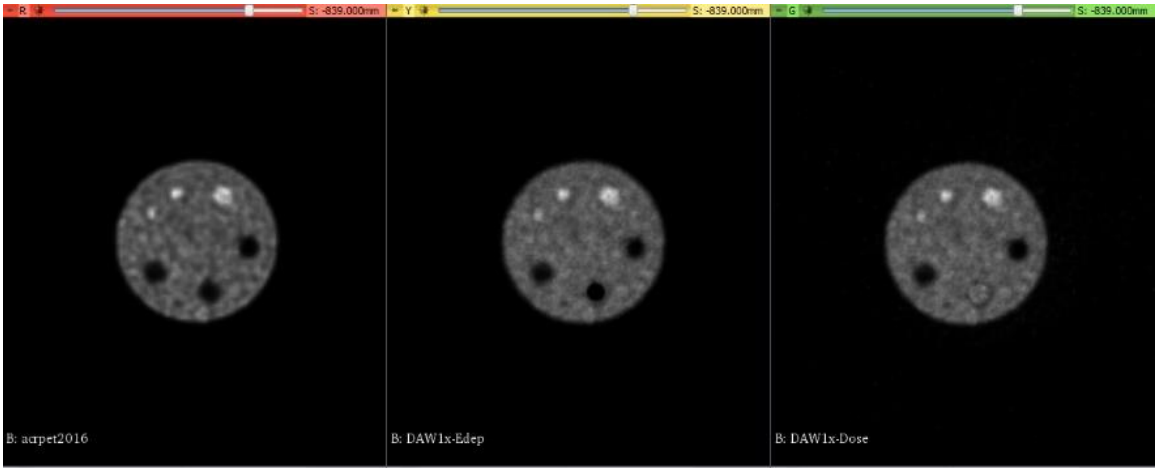

Figure 57: Comparison of F-18 PET (left), Y-90 Energy Deposited (middle), and Y-90 Absorbed Dose (right). The slice was through the hot and cold cylinders. Visual assessment indicates that contrast was maintained.

Figure 57 shows the same slice through the hot and cold cylinders displayed in the original F-18 PET image, the Y-90 energy deposition image and the Y-90 dose image. Notice the dose in the air-filled cold cylinder near the 6 o'clock position has a relatively

high dose. The absorbed dose is the energy deposited per unit mass. Due to the low mass of the air, the absorbed dose in the air-filled cylinder was relatively large.

The activity distribution in the original F-18 PET phantom was compared to the final Y-90 energy deposition by drawing volumes of interest (VOIs) in the largest hot and cold cylinders and comparing the values to the bulk fluid. In Figure 58, a red VOI is drawn in the largest hot cylinder, a green VOI is drawn in the bulk fluid and a yellow VOI is drawn in the cold, water-filled cylinder. The ratio of the activities was measured for the F-18 PET. The ratio of the deposited energy is measured for the Y-90.

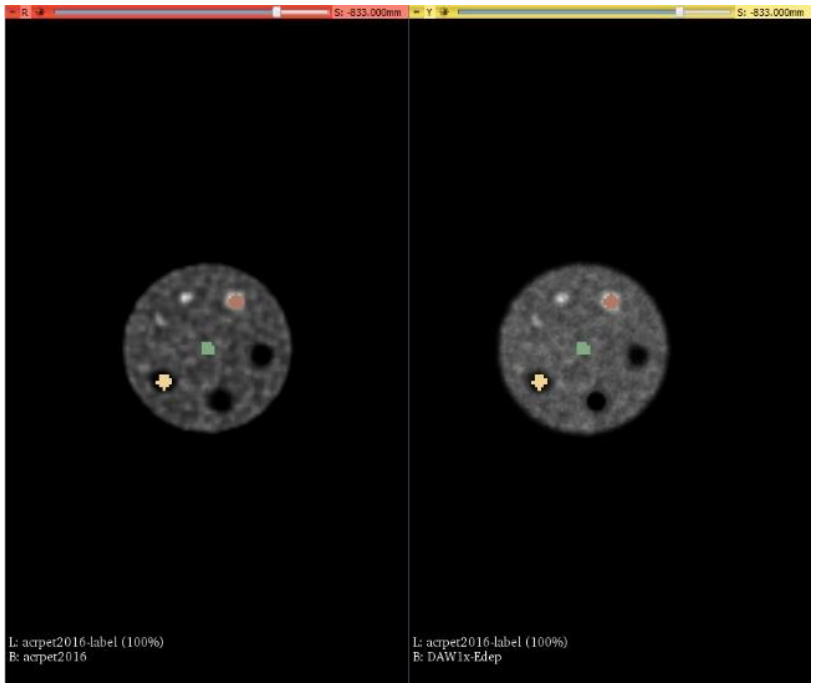

Figure 58: F-18 PET (left) and Y-90 Energy Deposited (right) and with spherical volumes of interest (VOIs) colored yellow, green, and red.

Table 6: Ratios of activities in F-18 PET phantom compared to Y-90 energy deposited map

Quantity	F-18 PET (ratio of activity concentration)	Y-90 Energy Deposited (ratio of energy deposited)
Ratio of hot 25 mm cylinder to bulk fluid (red/green)	2.291 ± 0.225	2.236 ± 0.214
Ratio of cold water cylinder to bulk fluid (yellow/green)	0.099 ± 0.545	0.137 ± 0.577

When the ACR PET phantom was loaded with F-18 FDG prior to scanning, the activity concentration in the hot cylinders was 2.42 times the activity concentration in the bulk fluid. Volumes-of-interest, (VOIs) were used to measure the activity concentrations from the images. Using the F-18 PET images, the image-based measurement of the ratio of the activity concentration in the hot cylinder to the bulk fluid was 2.291 ± 0.225. Performing the same measurement on the Y-90 energy-deposited images results in a ratio of the energy deposited of 2.236 ± 0.214. The results are in agreement within the stated uncertainty. VOIs were also drawn and compared for the cold water cylinder and the bulk fluid. The ratio (cold cylinder/bulk) with the PET image was 0.099 ± 0.545 while the same ratio measured on the Y-90 energy-deposited image was 0.137 ± 0.577. The quantities were in agreement within the stated uncertainty. It is apparent that the subject contrast was maintained from the surrogate F-18 PET phantom to the dosimetric calculations for Y-90 using GATE.

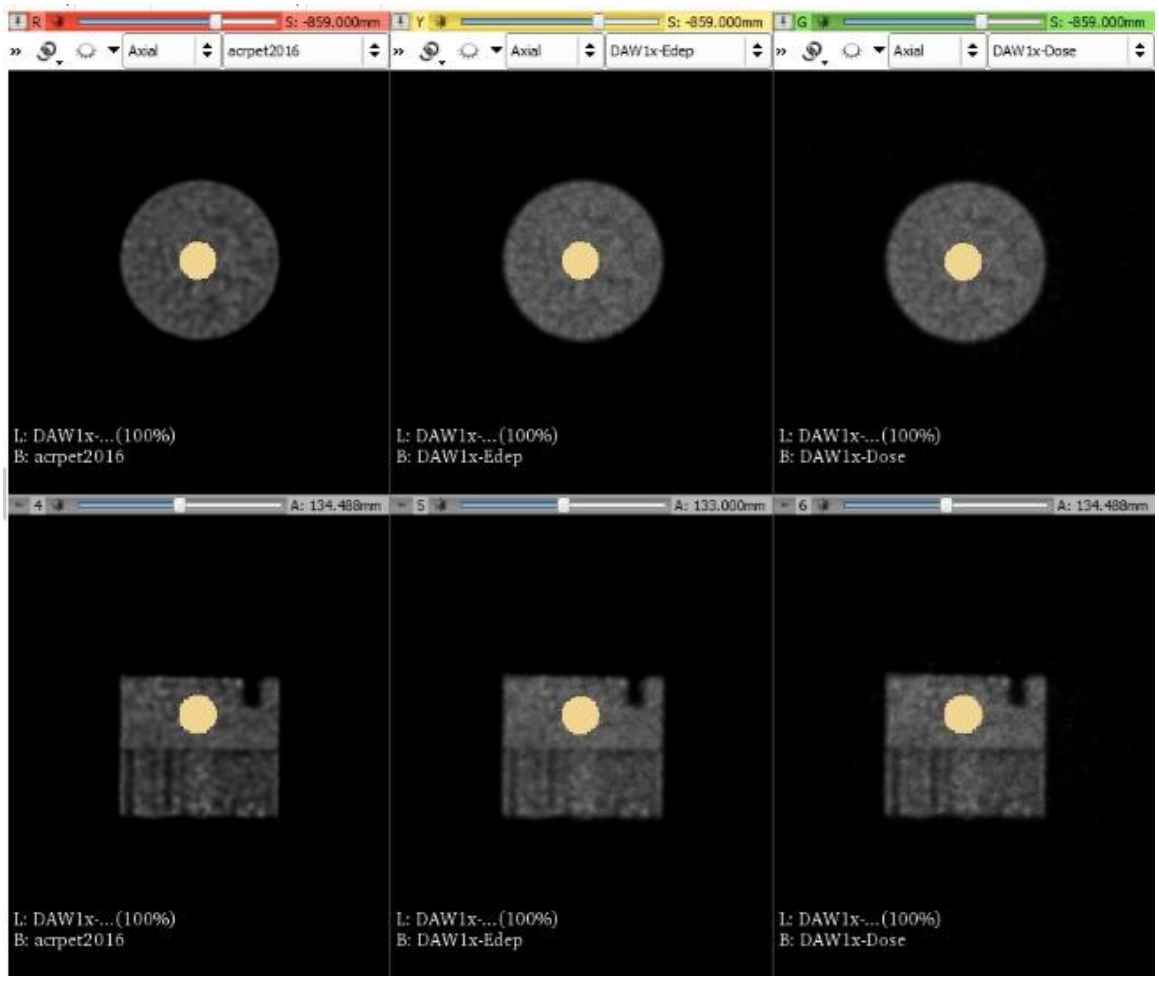

Figure 59: Spherical VOIs placed for signal-to-noise ratio measurements in F-18 PET (left), Y-90 Energy Deposited (middle) and Y-90 Absorbed Dose (right). Each VOI was identical 5 cm diameter sphere.

Table 7: Signal-to-noise ratios for the same VOI drawn on the three image types

	F-18 PET Image	Y-90 Energy Deposited Image	Y-90 Absorbed Dose Image
Signal-to-Noise Ratio	6.52	6.59	6.59

The signal-to-noise ratio (SNR) for the F-18 PET images were in good agreement with the Y-90 energy-deposited images and Y-90 absorbed-dose images produced by GATE. The GATE images actually had a slightly higher SNR. This may be due to

smoothing of the noise in the simulated Y-90 tomographic maps. The energy deposition due to the activity distribution has the effect of smoothing or blurring the activity distribution [8].

In conclusion, F-18 PET data can be used as a surrogate for Y-90 activity distribution. A Monte Carlo program such as GATE can use the F-18 activity distribution to produce accurate maps of the absorbed dose from Y-90.

B. Dosimetry Verification with Film

1. Introduction

The goal of the phantom and film experiment was to verify the absorbed dose calculated by imaging of a surrogate radionuclide and Monte Carlo modeling. Fluorine-18 was placed into a phantom which was imaged on the Siemens Biograph 40 mCT PET/ST scanner at OSIS. Y-90 was then introduced into the phantom and the absorbed dose to water in the phantoms was measured using radiochromic film. The film had been calibrated using a Sr-90/Y-90 source with a known output. The measured absorbed dose in the water was compared to the absorbed dose calculated from the PET/CT images and Monte Carlo modeling.

The average range of the Y-90 beta in water is 2.5 mm and the maximum range in water is 11 mm. In materials of interest such as water and tissue, there may be a large change in dose within a small spatial range. The steep dose gradient can make beta dose measurements very challenging. A dosimeter with a high spatial resolution may be required to sample the dose at different distances from the source. Radiochromic film

dosimetry is an established method of performing dose measurements from a beta-emitting source.

When radioactive microspheres are injected into a patient during radioembolization, the microspheres collect into capillaries and remain fixed in position. This produces a volumetric distribution of radioactivity. When radioactive microspheres are added to an aqueous solution, density differences cause the microspheres to settle to the bottom of the container. The hydroxyapatite microspheres used in these experiments would visibly clear from a solution within a few minutes. The microspheres then collect at the bottom of the container into a compact radioactive mass while the remaining aqueous solution is clear of radioactive material. This distribution is not similar to that expected in an organ such as the liver. To create a distribution that is more "life-like" several ideas were explored.

For the phantom imaging experiments, a homogenous system that was large enough to avoid partial volume effects was desired. Partial volume effects begin to affect the apparent activity of an object when the object size is three times the Full Width and Half Maximum (FWHM) of the reconstructed image resolution or smaller [73]. In general, the FWHM of PET scanners is approximately 5 mm. Thus, the size of an object in the phantom should be 1.5 cm or greater to avoid partial volume effects.

The simplest case was to use an aqueous solution of radioactive material and not use radiolabeled microspheres. This avoids the settling problem. When the F-18 and Y-90 are in solution, it is much easier to make homogeneous mixtures of different sizes.

At the time of this study proposal, it was possible to acquire surplus resin SIR-Spheres. However, the physicians at our facility have moved towards almost exclusive

use of glass TheraSpheres. Due to the nature of how the TheraSpheres are ordered and delivered, there were no surplus TheraSpheres available. It was necessary to purchase a source of Y-90. For this experiment, an amount of Y-90 yttrium chloride was purchased from a commercial supplier of radionuclides.

2. Methods

There are several factors that were considered when selecting the type of film to use. The film had to be sensitive in the expected range of absorbed dose. A waterproof film was selected to allow for direct measurement of radioactive fluid. Ultimately, the water-proof property of the film was not utilized. The thickness of the active emulsion layer and the protective layer were considered. The film active layer and protective layers were symmetric. There was not a front or back to the film. The film was transparent.

The film that was chosen was Gafchromic™ EBT-XD made by Ashland Global Holdings Inc. Lot number 08021701. The expiration date of the film is February 2020. The film is temperature sensitive. The film package contains a high-temperature warning strip to alert the user if the ambient temperature exceeded the vendor recommended value. EBT-XD contains an inner active layer 25 um thick situated between two polyester outer layers. Each outer layer is 125 um thick. The active layer contains a material that when exposed to radiation forms a blue polymer that has an adsorption maxima near 633 nm. The polyester layers protect the inner layer and make the film waterproof if the cut edges are kept dry. EBT-XD film is transparent. Exposure to

radiation causes the active layer to change color and darken. The amount of film darkening is dependent on the absorbed dose to the film.

Complete instructions on the use of Gafchromic film for dosimetry are available from Ashland [74]. The scanner used was an Epson model 11000XL, serial number 040059. This is a model recommended by Ashland for performing dosimetry with Gafchromic films. . The acquisition software was Epson Scan v.3.49A running in Windows 7. The film vendor provides recommendations for the scanner settings. Scans were done in professional mode with 48-bit color, 72 dpi resolution and color correction off. The scanned images with saved in the lossless format TIFF.

The film response is orientation dependent. The long side of the film can be parallel or perpendicular to the scan direction. An orientation should be chosen and films should be scanned in a consistent manner. In this experiment, the film was typically marked with a permanent marker to indicate orientation.

A 2 mm thick glass compression plate was used to keep the film flat against the scanner bed. The same glass plate was always used in the same orientation when scanning calibration and measurement films

A well-known effect exists known as the lateral response artifact [75]. For flat-bed scanners, the readout response varies in the direction lateral or perpendicular to the scan direction. Thus, for scanning of the film, the same lateral position should be used. For scans in this study, care was taken to ensure that objects of interest were centered laterally with respect to a reference line in the scan direction

The film response changes with time. After exposure the film was stored in a dark area. This allowed post-exposure changes in the active layer polymer to stabilize.

At least 24 hours was allowed between exposure and reading. Exposure times and reading times were recorded.

If the scanner has not been idle for more than an hour, the film manufacturer recommends that several "warm up" scans be performed prior to meaningful scans. The warm up scans equilibrate the light source which helps provide a consistent color.

The TIFF images were imported in the program ImageJ version 1.51k. Here the color images were separated into the three component channels, red, blue and green. The red channel image was used for dosimetry. However data from all three data channels can be used.

A film calibration curve was created with a calibrated source of Y-90. Calibrated Sr-90/Y-90 ophthalmic applicators with known dose rate have been used with success[76]. To produce an exposure, the applicator was placed on the film for a measured amount of time. The dose delivered to the film was determined by the product of the dose rate and the exposure time. The darkening of the film was measured with a flatbed scanner as described previously. By exposing film over the expected range of doses, a calibration curve was built. In subsequent measurements, the absorbed dose to the film was determined by measuring the amount of film darkening and comparison to the calibration curve.

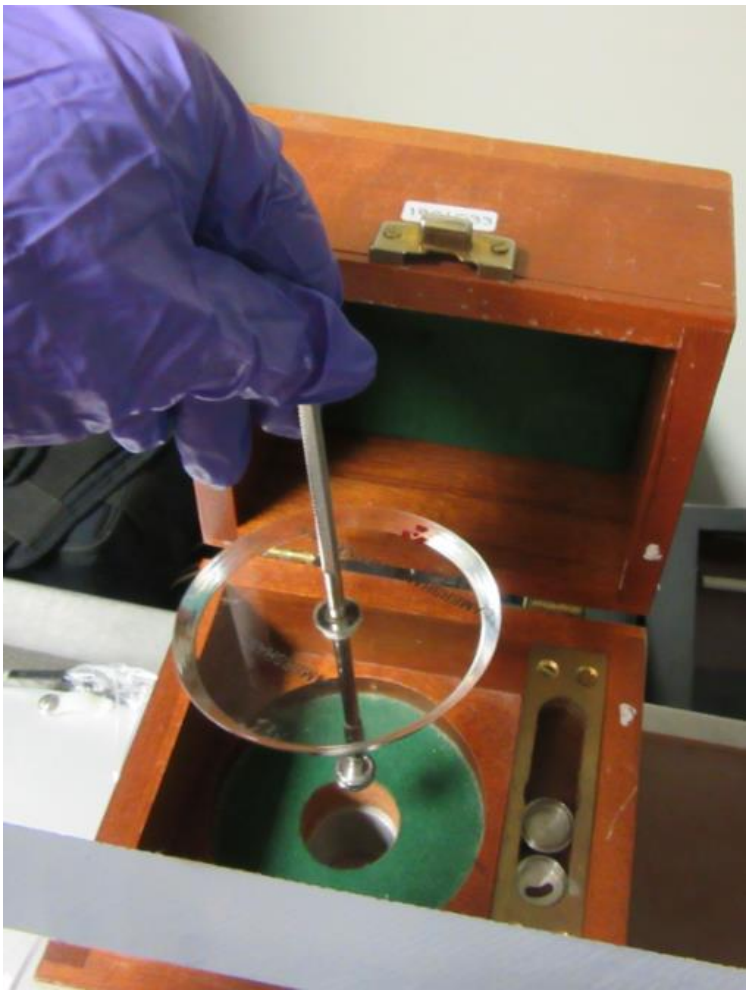

Figure 60: Amersham SIA.20 Sr-90/Y-90 ophthalmic applicator being withdrawn from its case. The source is the disk at the end of the rod.

The Sr-90/Y-90 source that was used was a model SIA.20 planar ophthalmic applicator produced by Amersham International, serial number 0547ML. Details regarding the construction of the source were difficult to find. The NCS 70 report states that the Sr-90 is embedded in silver with an active diameter of 9 mm and has a stainless steel container with a thickness of 0.05 mm at the face [77]. The parent nuclide Sr-90 has a relatively long half-life of 28.78 years. It decays by beta-minus decay into Y-90 which has a much shorter half-life. The parent and daughter nuclides are in secular equilibrium.

The applicator was calibrated in 2008 by the Accredited Dosimetry Calibration Laboratory (ADCL) at the University of Wisconsin-Madison. The Average Surface Absorbed Dose Rate to Water was found to be 0.39 Gy/sec over the central 4 mm diameter region of the source face. The dose rate was dependent on the activity of the Sr-90 source. The source strength was decay corrected using the same half-life that was used by the ADCL. The ADCL used a half-life of 28.78 years. The decay-corrected source strength at the time of this experiment was found to be 0.31 Gy/sec. The calibration uncertainty stated by the ADCL was +/-11%. A copy of the calibration documentation is in Appendix B.

A stopwatch was calibrated using the Direct Comparison Method described in Special Publication 960-12 published by the National Institute of Standards and Technology (NIST) [78]. The stopwatch was a Timex 1440. When performing the Direct Comparison Method, a phone call was placed to NIST located in Fort Collins Colorado U.S. The phone number for this location is (303) 499-7111. At the start of each minute, there is a voice recording announcing the upcoming time. Then a 1500 Hz tone marks the beginning of the minute. At the start of this tone, the stopwatch was started. The stopwatch was stopped when the tone of the next minute was heard. After the stopwatch had been stopped, the elapsed time was recorded. A total of 20 measurements were performed. The mean elapsed time was 59.998 seconds with a standard deviation of 0.068 seconds. For a 60 second measurement, the percent error associated with the error in time measurement is 0.11%. For a 10 second measurement, the percent error associated with the error in time measurement is 0.68%.

In the phantom, the radiochromic film is separated from a mixture of water and Y-90 by a "beta-window" made of a thin layer of polyester film. The film that was used was 0.001" (25 µm) thick "Dura-lar" sold by Grafix Plastics.

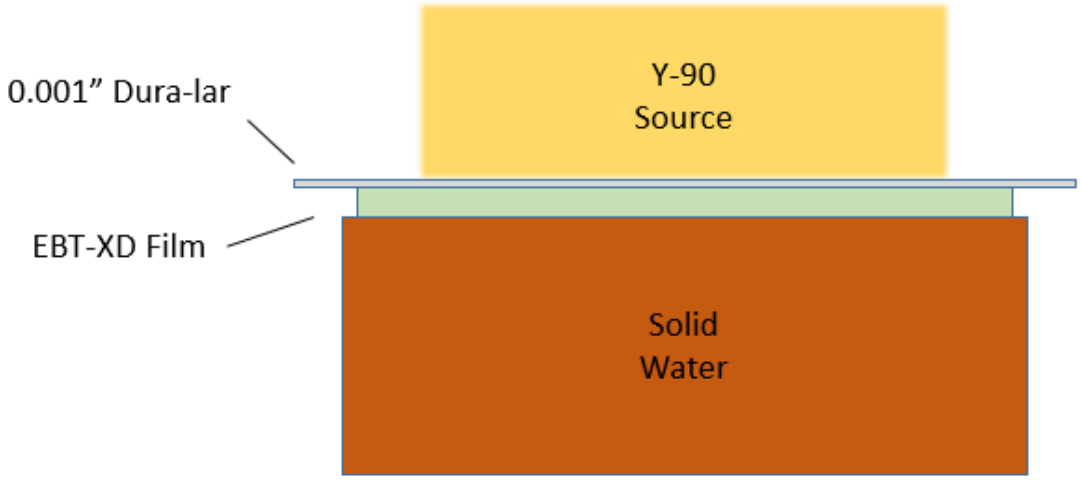

Figure 61: Depiction of the detector arrangement. During calibration, the Y-90 source was an ophthalmic applicator. During the experiment, the Y-90 source was Y-90 chloride in water.

There were several advantages of the phantom arrangement shown in Figure 61. When assembled, the film was in close proximity to the Y-90 and water source. The weight of the water placed a gentle pressure against the beta window that pushes out air from between the beta window and the radiochromic film. Another advantage is that the radiochromic film can be placed and removed without direct contact with the Y-90 source. This minimizes the likelihood of contamination of the EBT-XD film with Y-90.

It was also easy to remove the film if the phantom was going to be imaged with CT. The radiochromic film was to be removed prior to exposure to x-rays from the CT.

Each phantom was made from a Nalgene brand 500 mL jar. A hole was cut in the lid to allow access for the radiochromic film and solid water plug. The beta window was made by creating an inner-lid ring out of thick polyester. The thin (0.001") Dura-lar of the beta window was glued across the ring with contact cement. Green PVC cement was used to waterproof the seal between the thin film and the support ring. Figure 62 shows the phantom with the outer lid off. The inner support ring and beta window are visible. The phantom is filled with 400 mL of water and blue food coloring. Silicone grease was used to seal the support ring and the phantom body.

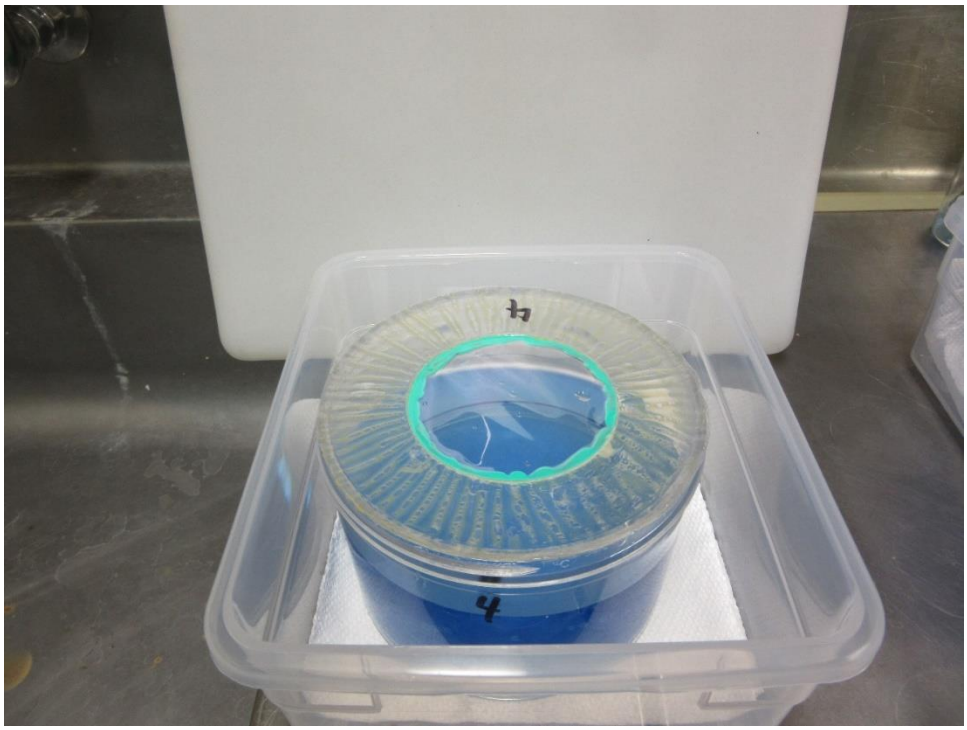

Figure 62: Phantom 4 with lid off showing the support ring and 0.001" thick polyester beta-window. The phantom contains 400 mL of fluid and blue food coloring. Silicone grease is used to seal the support ring and body of phantom.

In Figure 63, the blue outer lid has been installed. A 40 mm diameter paper disk is shown taped to the solid water plug. The paper disk was used during leak testing of the phantom. When making measurements, a disk of EBT-XD film would be taped into the same position as the paper disk.

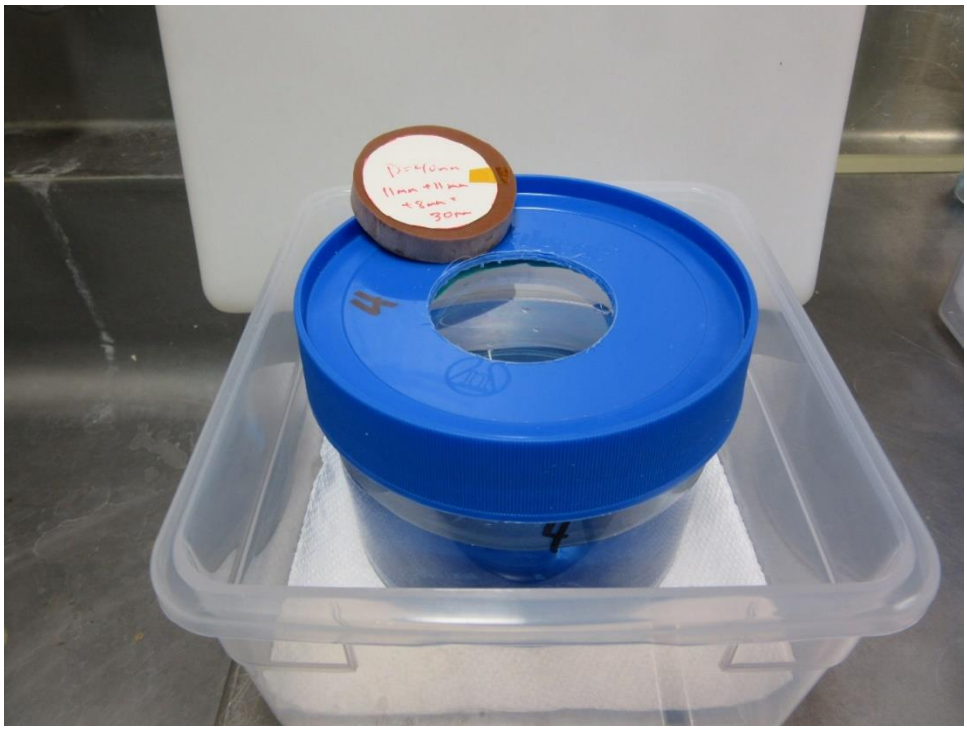

Figure 63: Phantom with outer lid on. There is a 40 mm diameter paper disk taped to the solid water plug. During use, the radiochromic film was taped to the solid water plug in the same manner.

Figure 64 shows the completely assembled phantom. When containing radiochromic film, the film would be sandwiched between the beta window and the solid water plug. To begin exposure to the film, the entire phantom was inverted so the beta window and plug was at the bottom of the phantom. The water/Y-90 mixture formed a layer that was approximately 4 cm thick above the radiochromic film.

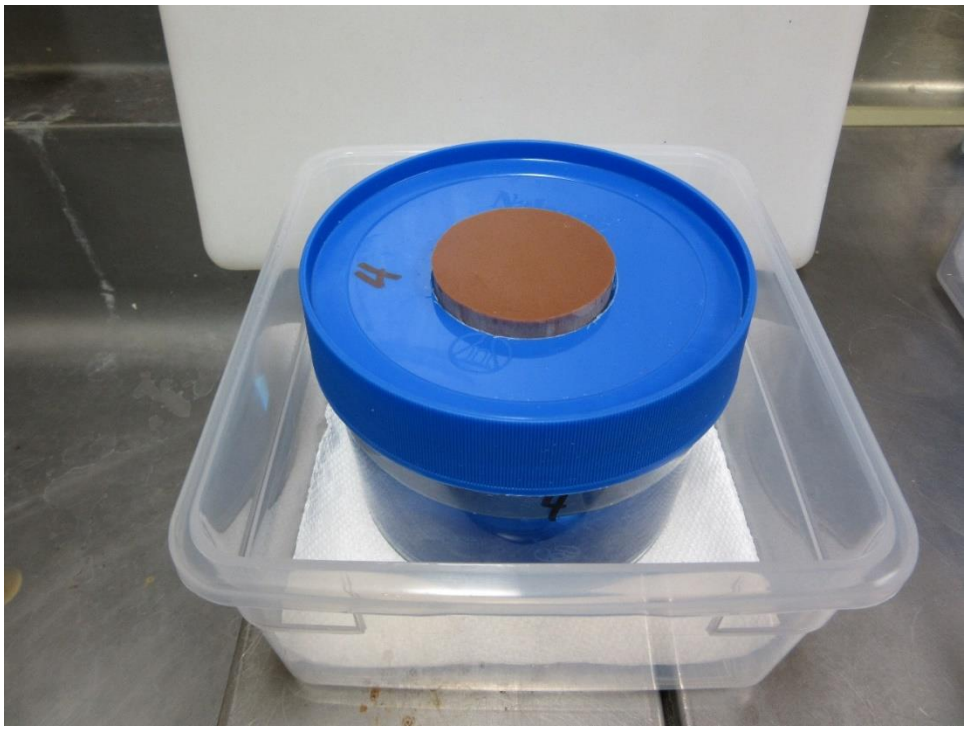

Figure 64: Phantom completely assembled. The solid water plug and film are in place. The final step in deployment of the phantom is to invert the entire assembly.

To perform calibration of the EBT-XD for a phantom, a strip of Gafchromic EBT-XD was cut from the original sheet. The unexposed strip was scanned with the Epson 11000XL. The radiochromic film was placed on a plate of solid water. This is the same solid water material that was used for the plugs backing the beta-windows. The Dura-Lar beta window from the phantom was placed over the radiochromic film. The SIA.20 applicator was then placed on the beta window. Irradiation of the radiochromic film occurred through the beta window of each phantom. Thus, each phantom had a calibration curve. In this manner, variation in thickness or other non-uniformity in the beta window material was accounted for in the calibration curve. The exposure time for each exposure was recorded using the calibrated stopwatch. The dose delivered to the calibration strip was determined by multiplying the dose rate to water at the face of the

Sr-90/Y-90 source by the exposure time. As noted previously, the error associated with the stopwatch measurements was low (±0.7% or less) compared to the error stated by the ADCL laboratory for the dose rate from the applicator (±11%)

The film vendor recommends a geometric progression of exposure time. The exposure time for the calibration curve generally followed the progression, 10, 15, 23, 34, 51, 76 and 114 seconds. This is a geometric progression with a common ratio of 1.5.

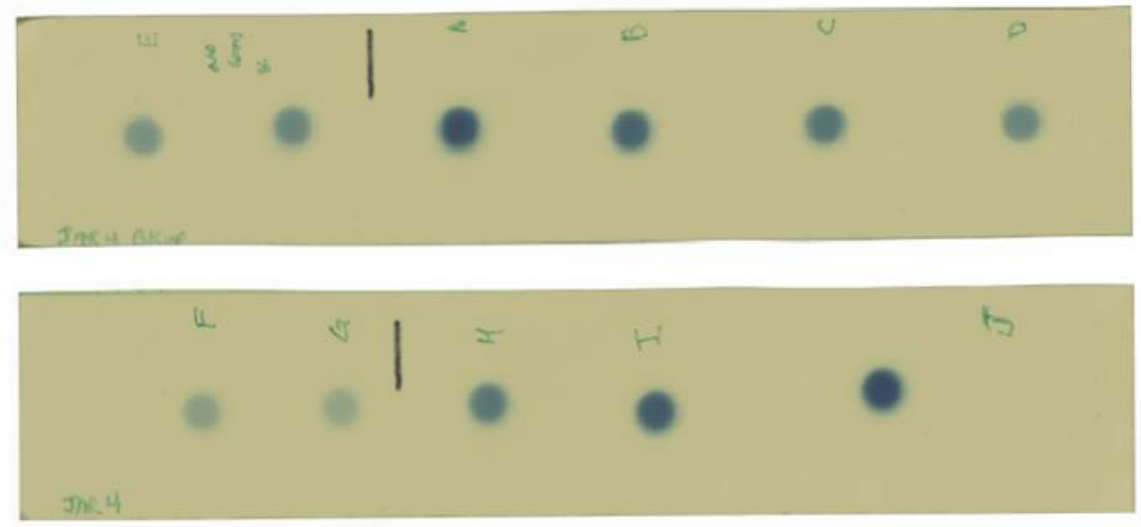

Figure 65: Strips of EBT-XD radiochromic film used for calibration of phantom 4. The dark circles are where the film was exposed with the Sr-90/Y-90 calibration source. The absorbed dose ranged from 3.6 to 38.6 Gy.

A region on interest (ROI) tool in ImageJ version 1.51k was used to measure film darkening. A circular region of interest 4 mm in diameter was placed in the center of each exposed area on the calibration film. The ROI tool was used to measure the mean pixel value and the standard deviation of the pixel value in the ROI.

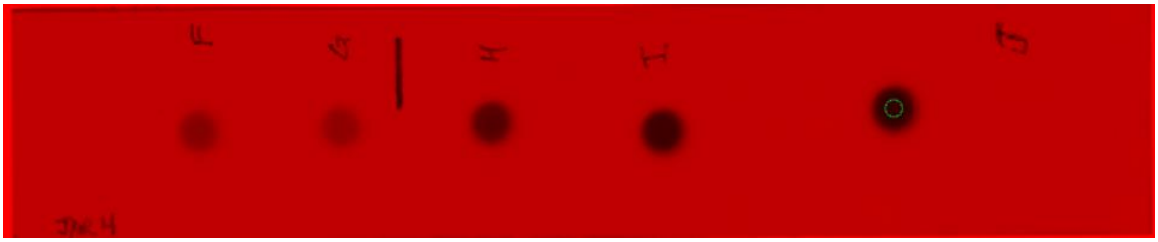

Figure 66: Red channel image of one of the calibration films for phantom 4. A green circular ROI is shown on the exposed area J.

The calculated absorbed dose and the mean pixel data were entered into MATLAB R2016a 64-bit version (MathWorks, Inc.). The curve fitting application in MATLAB was used to fit a curve to the data. Figure 67 shows a curve fit to the calibration data for phantom 4.

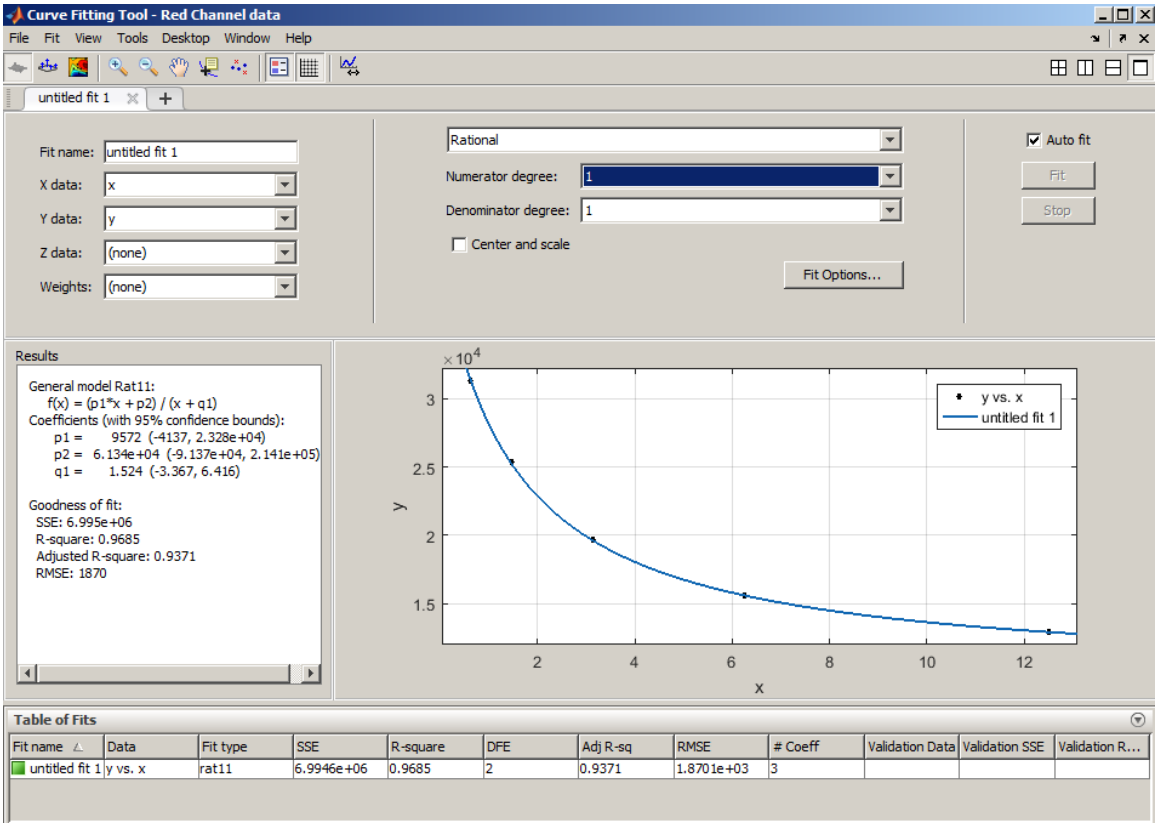

Figure 67: Screenshot from MATLAB curve fitting application showing the curve fit using a rational function.

In the literature are several recommendations regarding the form of the equation used to fit the calibration data Some suggestions, including those published by the film vendor, have been to use the general class of equations known as rational functions [79], [80]. The form of the rational function that was used for this study was:

$$F(x) = \frac{a + bx}{c + x} \tag{3.11}$$

The absorbed dose, x, is the product of the irradiation time and the dose rate produced by the applicator. The measured film response, i.e. darkening, is F(x). The curve fitting application in MATLAB was used to find the three parameters, a, b and c. This specific form was discussed in a paper by Micke et al. [81]. The EBT-XD white paper describes several advantages of using rational functions to fit the calibration data [80]. These include:

1. Rational functions are simple to invert. The equation above can be rewritten as:

$$x = \frac{a - cF(x)}{F(x) - b} \tag{3.12}$$

2. The functions plateau at high doses much like the film response.

3. The functions can be fitted with few data points. The vendor recommends six to eight data points with the doses spaced in a geometric progression.

The calibration curve for phantom 4 is shown in Figure 68.

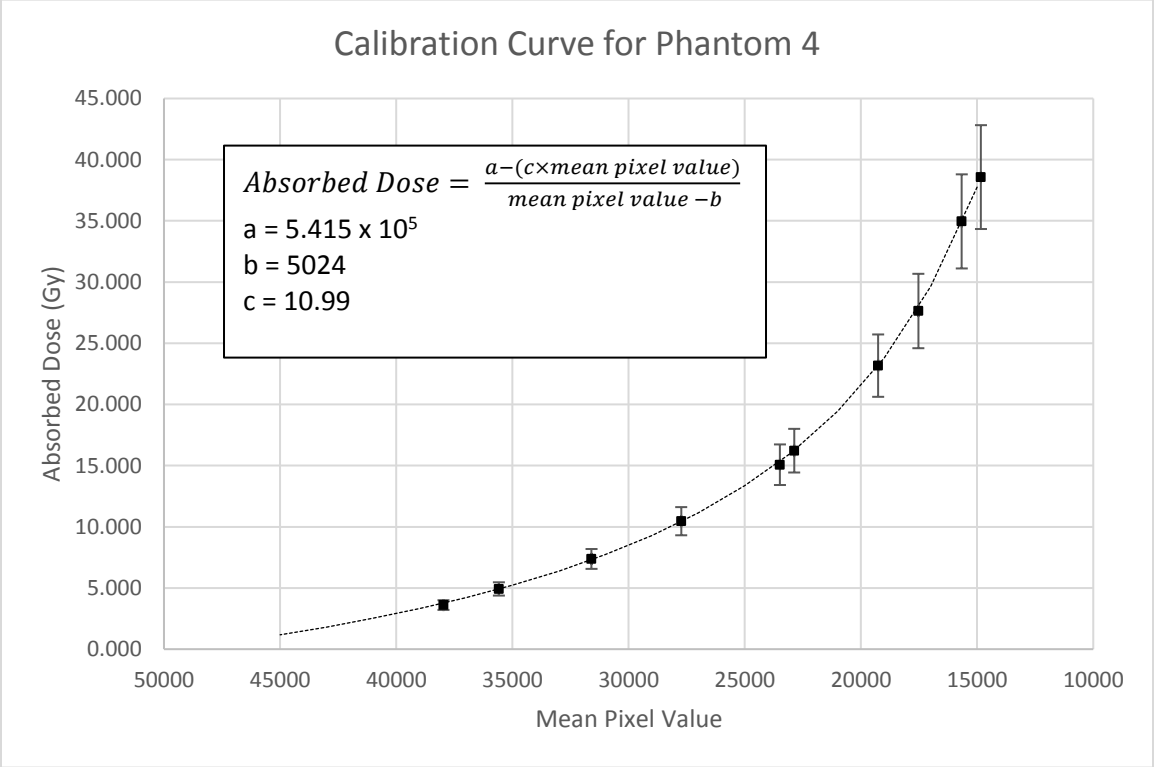

Figure 68: Calibration curve for phantom 4. The uncertainty in the absorbed dose is dominated by the uncertainty in the dose rate of the Sr-90/Y-90 applicator.

Due to the lack of availability of surplus Y-90 microspheres, it was decided to use Y-90 yttrium chloride. A source of Y-90 yttrium chloride, YCl_3, was purchased from Eckert and Ziegler, lot number YGB07. The calibration activity was 30 mCi at noon 12:00 EST 2018-Mar-05. The vendor stated that the uncertainty of the activity was within ± 10%. The source contained 1 mL of Y-90 chloride in 0.04 M HCl in a 10 mL P6 vial. The material was carrier free.

The Y-90 yttrium chloride was originally going to be divided among three phantoms, however, delays necessitated using only two phantoms. The material was divided among the phantoms on March 6, 2018. This was the day after the calibration

date. The activity in the vial was to be used to find the best calibration potentiometer setting for the dose calibrator. The activity in the vial was calculated using the decay equation. The vial was placed into the CRC-7 dose calibrator and the calibration potentiometer was adjusted until the dose calibrator reading matched the activity of the Y-90 yttrium chloride solution. Previous work with SIR-spheres in the same dose calibrator provided an estimate of the calibration potentiometer setting that would work for the P6 vial. In addition, a paper on dose calibrator setting for Y-90 ibritumomab tiuxetan also provided an estimated calibration setting for Capintec dose calibrators [82]. It was found that a calibration potentiometer setting of 43 provided an accurate activity reading for the Y-90 chloride in the P6 vial. At this setting, the displayed activity needed to be multiplied by a factor of 10 to arrive at the correct activity.

Activity measurements were done on the 20 mCi range setting. The calibrator was zeroed prior to measurement. The Y-90 chloride had been delivered in a volume of 1 mL. To split the activity between the two phantoms, the volume of the fluid in the vial was increased to 2 mL. To do this, a solution of 0.04 M HCl was created and 1 mL was injected into the vial. The activity was measured again in the CRC-7 dose calibrator with a calibration setting of 43. It was found that the activity was significantly different that the activity reading with a fluid volume of 1 mL. This indicated that the dose calibrator activity reading was sensitive to the fluid volume in the vial. A 5 mL syringe was used to withdraw 1 mL of fluid. This brought the fluid volume in the P6 vial back to 1 mL. The activity in the P6 vial was remeasured. The activity in the 5 mL syringe was determined by subtracting the initial activity measurement at 1 mL from the post-withdrawal activity measurement also with a 1 mL volume in the vial. The activity in the syringe was

injected into phantom 4. The residual activity in the syringe was measured and found to be 0.00 mCi. It was determined that a total of 11.2 mCi had been injected into the jar phantom. The remaining 1 mL of fluid in the P6 vial was withdrawn from the vial with the 5 mL syringe. Non-radioactive solution of 0.04 M HCl was used to bring the volume in the P6 vial back to 1 mL. The residual activity in the P6 vial was then measured. The activity in the 5 mL syringe was determined by subtracting the post-withdrawal measurement of residual activity from the pre-withdrawal measurement. Note all activity measurements were done with the fluid volume in the P6 vial at 1 mL to reduce variation in the dose calibrator readings due to geometric effects. The activity in the 5 mL syringe was added to phantom 2. The residual activity was measured and found to be 0.00 mCi. The activity placed into phantom 2 was 9.7 mCi.

Figure 69: 10 mL P6 vial containing 30 mCi of Y-90 yttrium chloride in 1 mL volume.

Disks of EBT-XD film had been scanned and cut prior to loading the phantoms. Each disk of film was 40 mm in diameter. The maximum range of the Y-90 beta electrons in water is 11 mm. Thus, the planned area for reading the film was the central portion of the film that was 11 mm from the edge. This was the circular central area 18 mm in diameter.

After the phantoms had been loaded with Y-90 chloride, a disk of radiochromic film was taped to the solid water plug. The film and plug were placed against the beta window and taped into position. The phantoms were then inverted. The time of inversion was recorded.

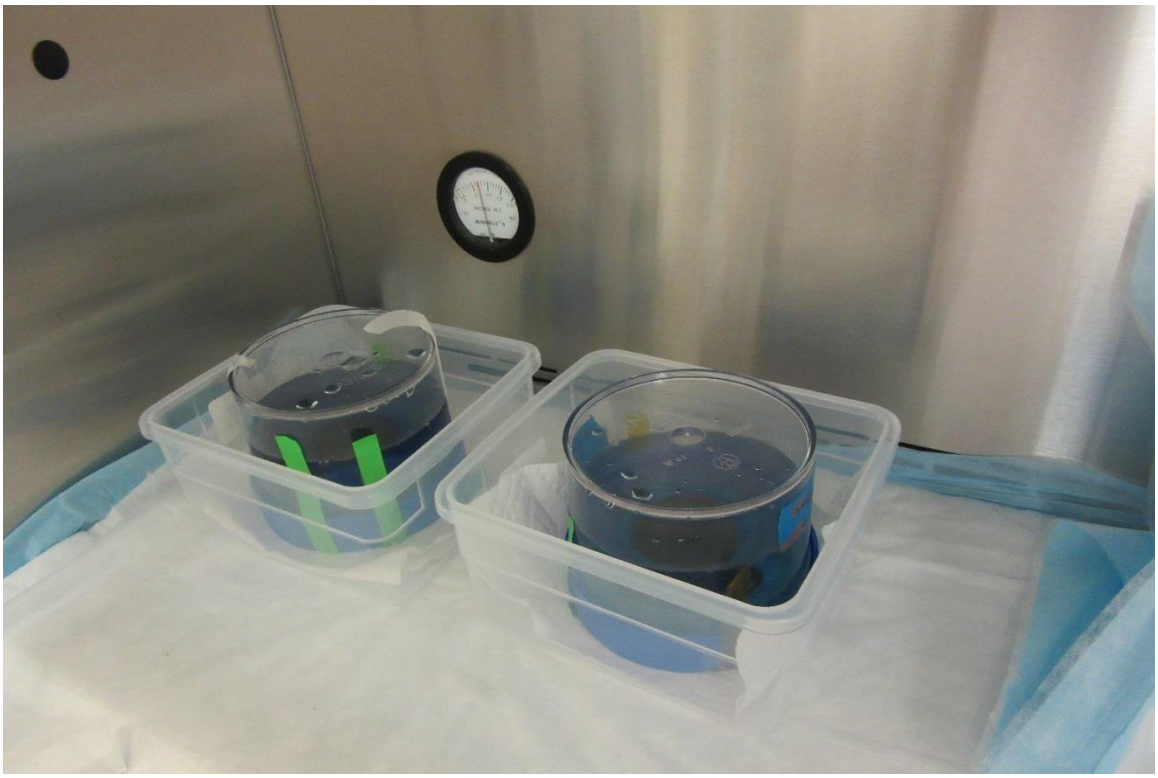

Figure 70: Phantoms 4 and 2 in the inverted position. Each phantom had the radiochromic film and solid plug on the underside.

The length of time that the radiochromic film was exposed to the solution of Y-90 chloride and water determined the absorbed dose to the film. The integral of the activity equation between the two times could be used to determine the total number of disintegrations in the water solution. The total number of disintegrations multiplied by the average energy per disintegration provided the total energy deposited in the water solution. The energy deposited in the water was then divided by the mass of the water to determine the absorbed dose to the water. The radiochromic film had been calibrated with the ophthalmic applicator through the beta window to a known dose delivered to water at the surface of the applicator.

A GATE run was performed using the same geometry and phantom as used to expose the film. The input to the GATE run were PET and CT DICOM series acquired on the Siemens Biograph mCT PET/CT at OSIS. The phantom had 61 μCi of the surrogate radionuclide, F-18 added to 400 mL of water. One bed position was used. A stop condition of 100 million counts was set. A 400 x 400 matrix and a Gaussian filter with a 2.0 FWHM was used. Time-of-Flight and TrueX with an iterative method using 1 iteration and 21 subsets were used to reconstruct the PET series. A CT was acquired for attenuation correction. The CT was acquired using 120 kVp, 40 mAs, helical acquisition with a reconstructed slice thickness of 5 mm.

Figure 71: Phantom in position for scanning in Siemens Biograph mCT PET/CT.

The software 'VV' was used to convert the DICOM PET and CT images into the MetaImage format for importation into GATE. The number of primary electrons used in the GATE run was equivalent to the number of disintegrations as discussed previously in the section on the homogenous phantom. A GATE run was performed with 10^7 primary electrons produced using the Y-90 beta energy spectrum. This is equivalent to an integrated activity of 30.1 Bq of Y-90. The absorbed dose to water for this activity was measured by opening the absorbed dose tomographic map in 3DSlicer and placing a VOI

in the water near the area where the radiochromic film was exposed. The absorbed dose to the water in the phantom was scaled according to the number of disintegrations that occurred in the water. The number of disintegrations that occur between two points in time is given by the following equation.

$$Total\ Disintegrations\ =\ A_0 \int_{t_1}^{t_2} e^{-\lambda t} dt \tag{3.13}$$

Here A_0 is the calibration activity at the calibration time = 0. The times t_1 and t_2 are referenced to the calibration time and lambda, λ, is the decay constant.

If the radiochromic film was to be immersed in the water, the dose to the film would be nearly equal to the absorbed dose to the water. When the film dosimeter is moved to the bottom of the phantom, the geometry changes from 4π geometry to 2π geometry. The absorbed dose in the film will be half of the absorbed dose in the water.

GATE runs were performed in which the attenuation properties of the EBT-XD film were examined. The run set up is shown in Figure 72. It was found that the dose to the active region of the film was nearly equal to the dose to the bulk water. To examine the effect of moving the film dosimeter to the edge of the phantom. The same run depicted in Figure 72 is shown in Figure 73. However, for the second case, only one water-filled cylinder contained Y-90. The dose to the radiochromic film was half of the dose delivered when the film was completely surrounded by Y-90 and water. Thus, the dose measured with radiochromic film in the geometry used in the phantoms was half of the absorbed dose in the bulk fluid. Small changes due to attenuation in the beta window have been taken into account by calibration of the film through the beta window with the Sr-90/Y-90 applicator.

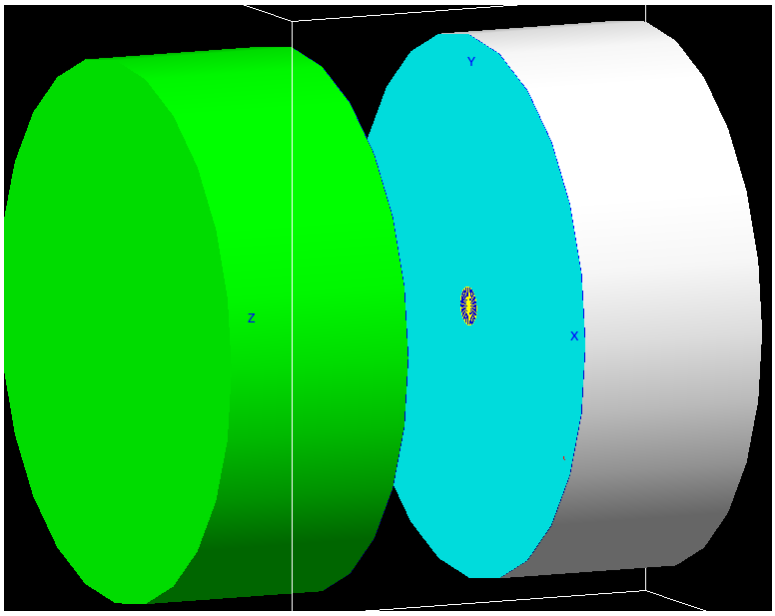

Figure 72: GATE model of two water-filled cylinders (green and white) each containing Y-90. A 4 mm disk of EBT-XD film is surrounded by an annulus of film. The two water cylinders were moved into contact with the film prior to starting the simulation. This models the submersion of the film into a water-filled phantom.

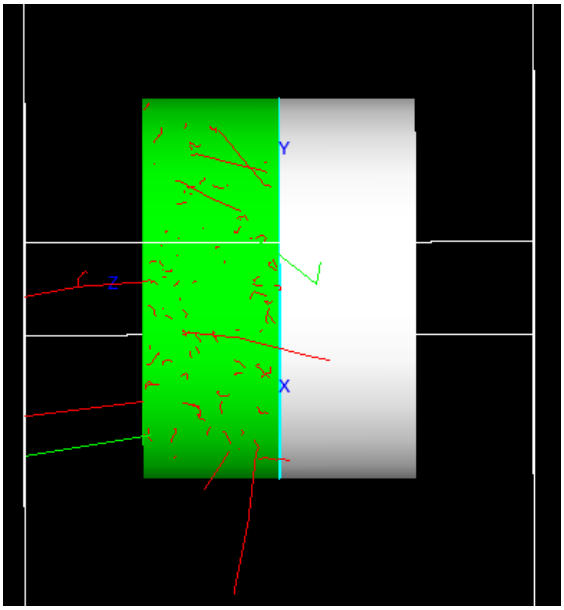

Figure 73: Gate simulation in which only one of the water cylinders (green) contains Y-90. This models the situation where the film is against the Y-90 water phantom and has a solid water backing.

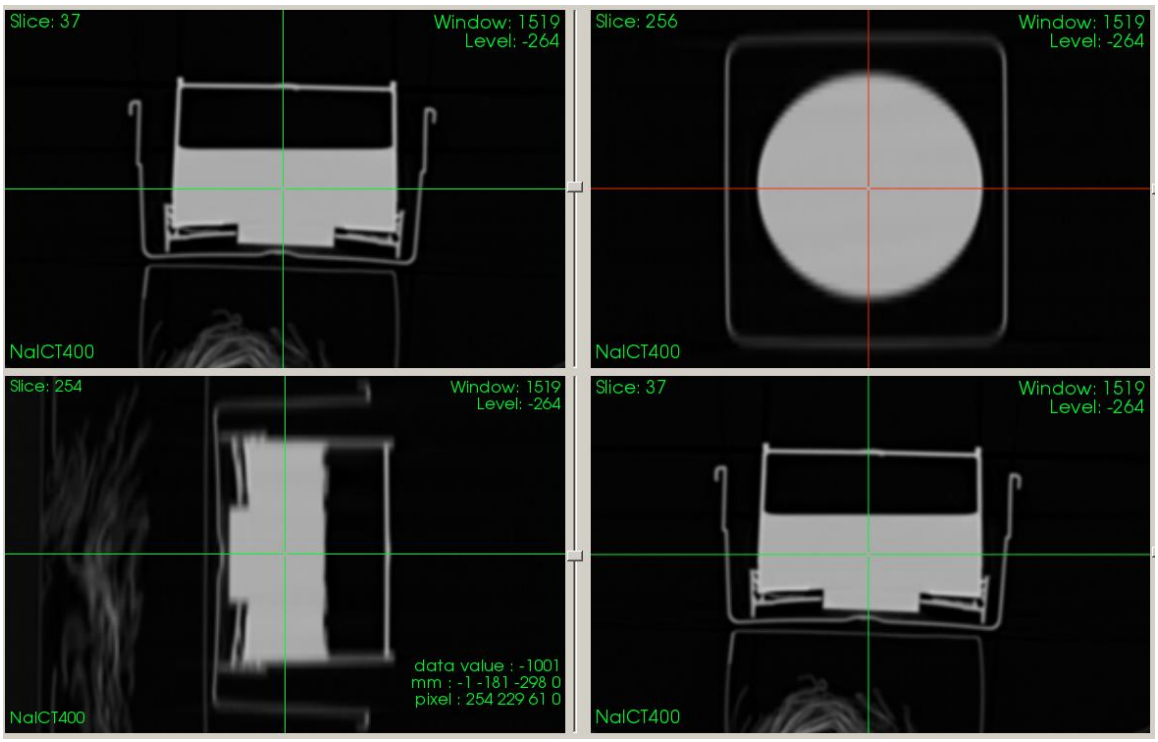

Figure 74: CT of the jar phantom in the inverted position. The solid water cylinder is seen at the bottom of phantom.

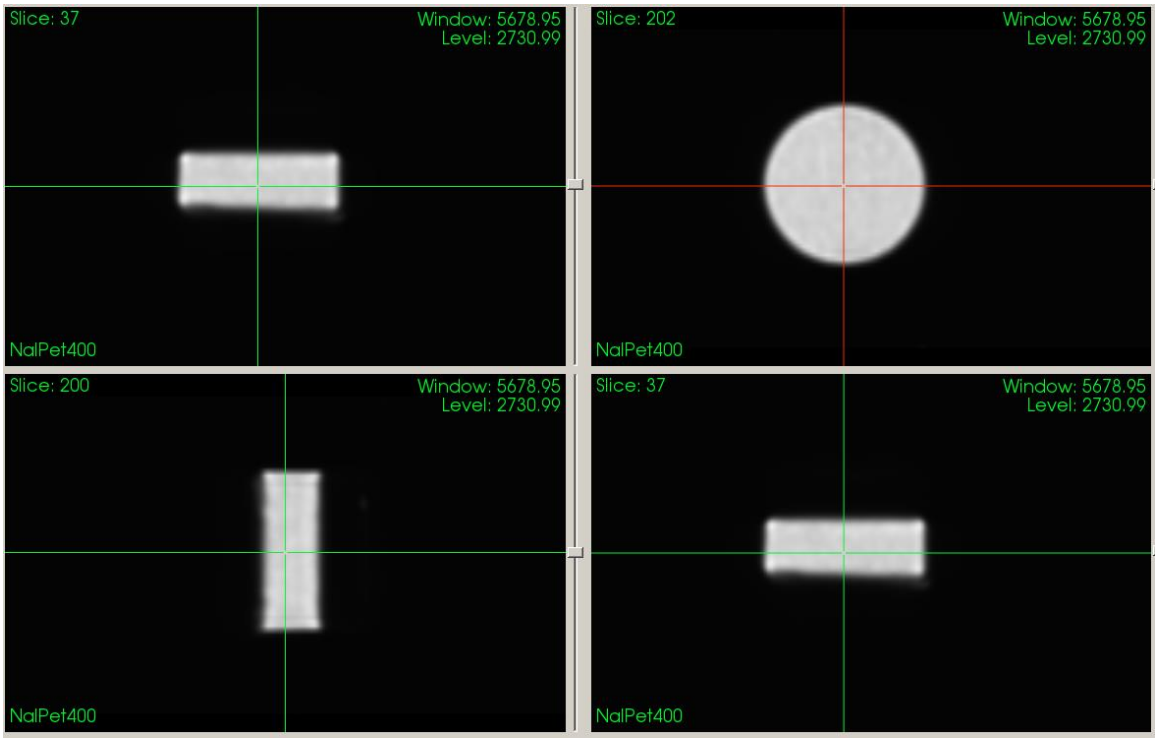

Figure 75: PET scan of fluid in jar phantom. Approximately 61 µCi of F-18 was added to the jar phantom.

As an example, the film disk D1 was deployed on the phantom 1.33 hours after the calibration time. The film remained on the phantom for 21.38 hours. Thus t_2 is 1.33 hours plus 21.38 hours. The calibration activity was 11.21 mCi or 4.15×10^8 Bq. The number of disintegrations that occurred during this time was 2.80×10^{13}. To calculate the he absorbed dose using the GATE results, the dose from 10^7 was scaled to the number of disintegrations occurring during the deployment of the film. The scaling factor was then multiplied by the absorbed dose read from the VOI placed in the GATE-generated tomographic dose map. This is shown in Figure 76. In this case the scaling factor was 2.80×10^6. The absorbed dose to water measured with the VOI from the GATE run was 3.80×10^{-6} Gy $\pm$ 0.23×10^{-6} Gy. The scaled dose to the bulk water was 10.64 Gy $\pm$ 0.64 Gy.

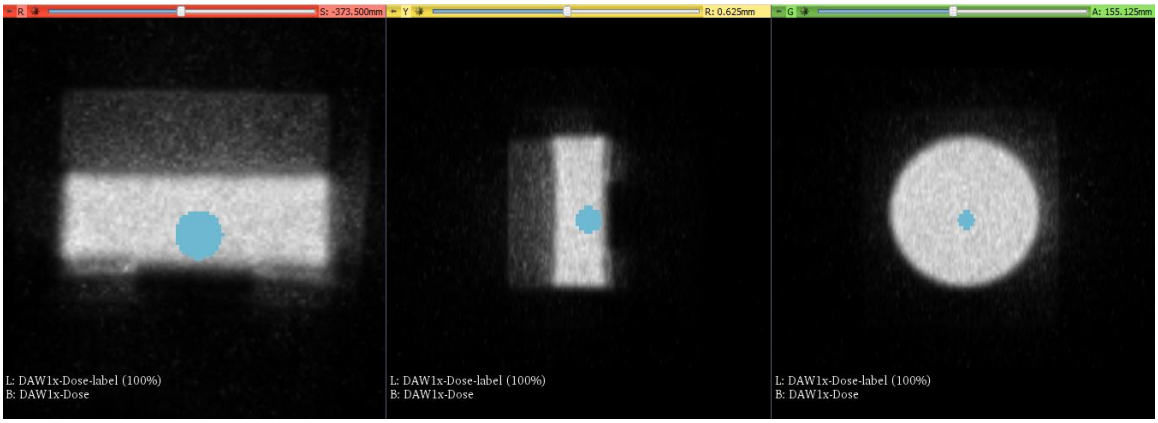

Figure 76: Tomographic absorbed dose map output from GATE run. A total of 10^7 primary Y-90 electrons were used. A VOI shown in blue was used to determine the absorbed dose to the water in the central region of the phantom.

The bulk dose measured with GATE was in agreement with the calculated value of 10.41 Gy ± 1.04 Gy calculated by integrating the activity over the irradiation time and multiplying by the mean energy per disintegration. The dose to film disk D1 was 50% of the absorbed dose to the bulk water. Using the scaled bulk dose calculated using GATE, the dose to disk D1 was:

Dose to D1= 0.5*(10.64 Gy ± 0.64 Gy) = 5.32 Gy ± 0.32 Gy.

Table 8: Comparison of GATE calculated results to analytically calculated results.

Film ID	**Time Post-Calibration When Film Deployed (hours)**	**Time Spent on Phantom 4 (hours)**	**Calculated dose delivered to film (Gy)**	**Calculated dose delivered to film using GATE results (Gy)**
D1	1.33	21.38	5.20 ± 0.52	5.32 ± 0.32
D3	22.75	27.15	5.09 ± 0.51	5.21 ± 0.31
D5	49.98	22.36	3.20 ± 0.32	3.29 ± 0.20
D6	73.82	67.20*	5.94 ± 0.59	6.16 ± 0.37
D8	142.10	47.70	2.21 ± 0.22	2.26 ± 0.14

*Daylight savings time, March 11, 2018 taken into account

The first film radiochromic disks were deployed on phantoms 4 and 2. The films were checked the next day. At that time, it was found that phantom 2 had leaked and the film disk was contaminated with Y-90. An attempt to clean the Y-90 from the film disk was unsuccessful. Phantom 2 was retired and not used for the remainder of the experiment. The first film disk that was removed from phantom 4 was disk D1. After removal, the film was placed in an envelope and placed in a dark area to stabilize. The next disk, D3, was taped to the solid water and deployed on phantom 4.

3. Results

After irradiation, the film was placed in a dark area to equilibrate. After at least 24 hours, the film was scanned on the Epson 11000XL. The same methods used to scan and measure the calibration films were used for the film disks. The TIFF image was imported into ImageJ. The ROI tool was used to draw circular ROIs in the center of the disk image. Each circular ROI was 18 mm in diameter. A total of 5 film disks were acquired. All were irradiated on phantom 4.

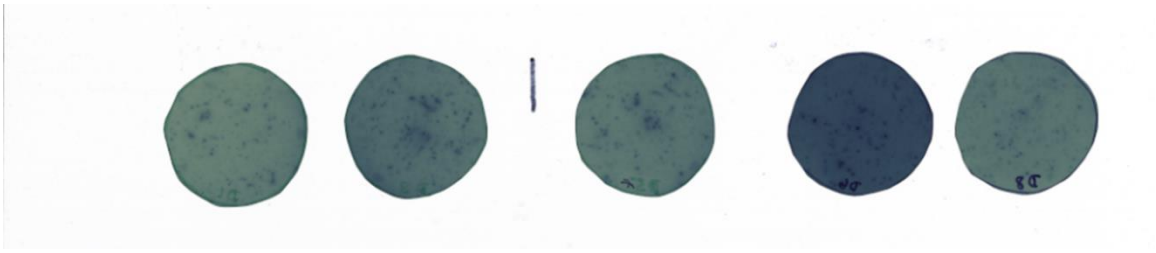

Figure 77: Five EBT-XD film disks that were irradiated on phantom 4. Going from left to right: D1, D3, D5, D6 and D8.

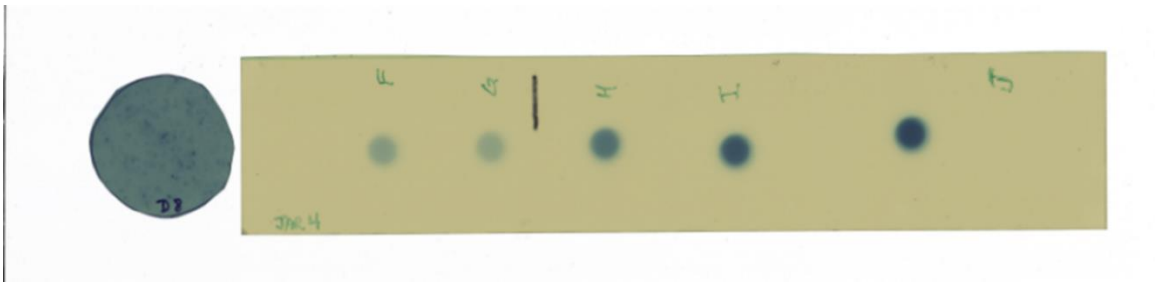

Figure 78: Film disk D8 next to one of the calibration films for phantom 4.

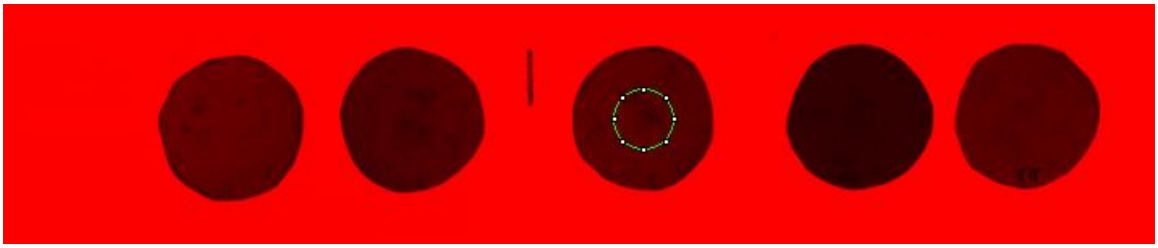

Figure 79: Red channel image of film disks with 18 mm x 18 mm circular ROI placed on disk D5.

Table 9: Comparison of dose measurements from radiochromic film and analytically calculated doses.

Film ID	Time Post-Calibration When Film Deployed (hours)	Time Spent on Phantom 4 (hours)	Calculated dose delivered to film (Gy)	Measured dose delivered to film (Gy)	Delta (Measured Dose – Calculated Dose) (Gy)
D1	1.33	21.38	5.20 ± 0.52	11.22 ± 1.32	6.02
D3	22.75	27.15	5.09 ± 0.51	20.63 ± 2.84	15.54
D5	49.98	22.36	3.20 ± 0.32	16.26 ± 2.28	13.07
D6	73.82	67.20*	5.94 ± 0.59	43.33 ± 5.26	37.39
D8	142.10	47.70	2.21 ± 0.22	15.87 ± 1.89	13.66

*Daylight savings time, March 11, 2018 taken into account

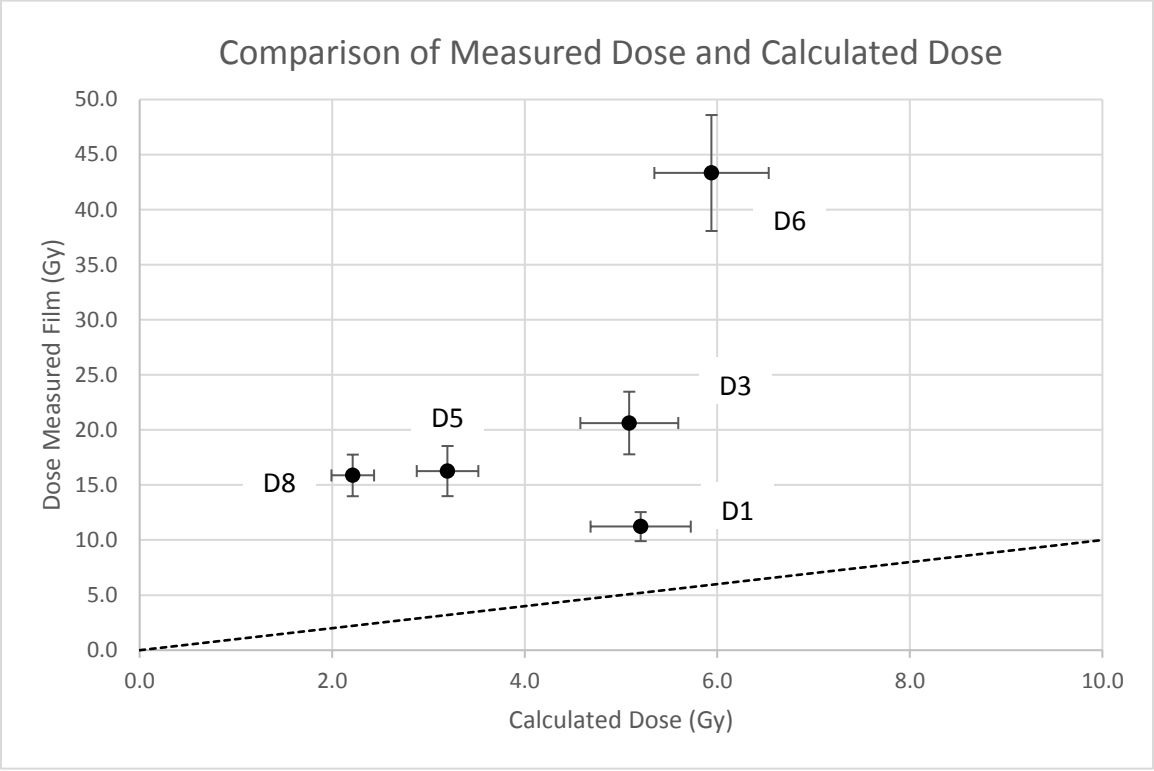

Figure 80: Results for radiochromic film experiment. Comparison of absorbed dose measured with film to calculated dose.

The calculated dose to the film and the measured dose to the film were not in agreement. In general, the absorbed dose measured by the EBT-XD film was much larger than the dose calculated by integrating the activity over the time in which the film was deployed on the phantom. A comparison of the dose measurements is shown in Figure 80. Measurements in perfect agreement would lie on the dotted line. There are several proposed reasons for the discrepancy in the dose measurements. The disagreement could be due to a single cause or could be due to a combination of causes.

1. The activity of Y-90 could have been outside the 10% uncertainty quoted by the supplier. This is unlikely. If this were the case, the overestimation of the absorbed dose by the film would have been consistent. In communication with the vendor, the manufacturing supervisor "was able to confirm that the dispensed activity was 97% of the expected activity".

2. Density differences in the aqueous solution of Y-90 chloride produced a higher concentration of Y-90 on the bottom of the container than on the top. There is evidence that this may have contributed to the discrepancies in dose. To check for settling of the Y-90, the phantoms were allowed to settle for 24 hours. An aliquot was drawn near the surface of the fluid and another aliquot was obtained at the bottom of the container. The aliquots were equal volume. The activity in the aliquots was measured with the Wizard^2 automated counting system. Each aliquot was counted for one minute with the energy window open to capture the diffuse bremsstrahlung spectrum. For phantom 4, the aliquot taken from the top liquid had a count rate of 681830 cpm. The aliquot taken from the bottom of the container had a count rate of 769221 cpm. The ratio of the bottom counts to the top counts is 1.13. The additional concentration of Y-90 at the bottom of the

container near the film was insufficient to account for the dramatic increase in the absorbed dose measured by the film.

3. Bremsstrahlung x-ray production in the fume hood could have led to additional energy deposition in the film. Measurements with a survey meter showed this to be an unlikely scenario. To shield the metal from Y-90 beta electrons, slabs of Lucite at least 1 cm thick were placed around the phantoms for the last film deployment. It did not solve the problem.

4. The film is perhaps being over sensitized by long exposures to radiation. There appears to be a correlation between deployment time and the degree to which the absorbed dose is being overestimated. This trend can be seen in Figure 81. A search of the literature did not find a mention of this effect. Similar types of radiochromic film to EBT-XD have been in use for decades. A dramatic effect such as this that has gone unnoticed seems unlikely.

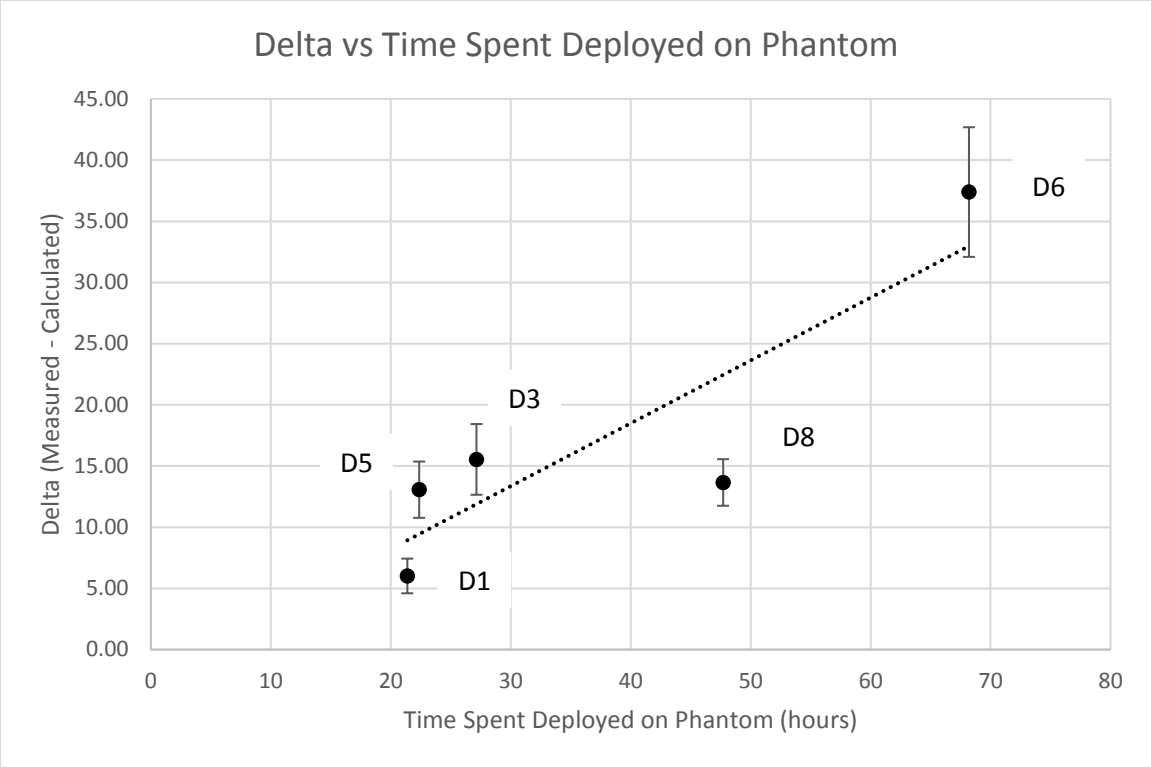

Figure 81: Delta is the difference between the dose measured with the radiochromic film and the calculated dose. Perfect agreement would have a delta of zero. There appears to be a correlation between the time spent irradiated on the phantom and the overestimation of the absorbed dose.

5. The Sr-90/Y-90 ophthalmic applicator source activity was possibly incorrect. The source was last calibrated in 2008. A possibility was that the source had been damaged or altered such that the dose rate at the surface of the applicator was less than the stated dose rate. An Elekta linear accelerator at the UNM Cancer Center was used to irradiate five EBT-XD films with a known beam of 6 MV x-rays. The dose to the film was determined to within a few percent. The film was allowed to stabilize for over 12 hours. A Victoreen model 07-433, Serial Number 108510 clam-shell densitometer was used to measure the optical density (OD) of the EBT-XD film exposed by the linear accelerator and the calibration films exposed with the Sr-90/Y-90 eye applicator. Prior to

measurements, the calibration of the densitometer was checked with test strip Serial Number A093364. Base plus fog measurements were also acquired of the films and subtracted from the OD values. The results of the densitometer measurements are shown in Figure 82. The results are in agreement. The calibration curve produced with the Sr-90/Y-90 eye applicator was not the cause of the large discrepancy in the dose measured with film.

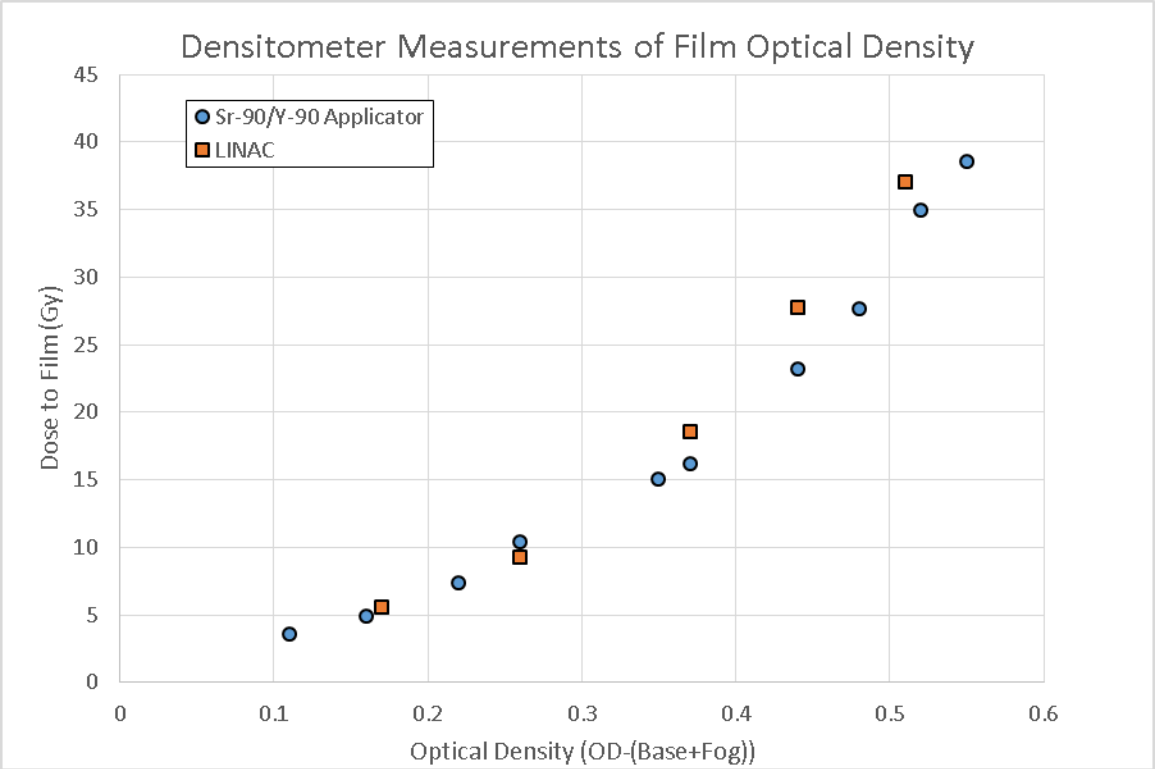

Figure 82: Dose as a function of optical density (OD). The doses delivered to the Sr-90/Y-90 calibration films and the films irradiated with the linear accelerator are plotted as a function of the measured optical density.

6. The possibility that the EBT-XD was responding to visible light was investigated. A disk of unexposed film was deployed in phantom A. This phantom had

been loaded with water but was never loaded with Y-90. The phantom has the same optical properties as phantom 4 and phantom 2. Prior to deploying phantom A, the other phantoms and sources of radiation were moved out of the fume hood were the previous film exposures had taken place. The fume hood was surveyed with a calibrated G-M survey meter and the exposure rate was at the typical background rate of approximately 0.02 mR/hr. Phantom A was placed in the fume hood at the same location that was occupied by phantom 4. After 24 hours, the film disk was removed from phantom A. The optical density of the film disk was measured with the clam-shell densitometer. It was determined that any film darkening, if present, was negligible.

7. The Y-90 yttrium chloride is bonding to the containers. The material is shipped in glass as YCl_3 in 0.04M HCl. When the acidic YCl_3 is added to water, the pH becomes more neutral and metal oxides form[83]. These metal oxides may precipitate and adsorb on to plastic container walls. This can result in an activity concentration at the walls and beta window several times greater than the activity concentration found in a homogeneous mixture.

The phantoms were 500 mL Nalgene jars. The body was polycarbonate and the lid was polypropylene. The beta window was made of Dura-lar, a commercial name for polyethylene terephthalate (PET) polyester. The paper by Park et al. states that the metal oxides are formed on a time scale consistent with the decay of the radionuclides [83]. Figure 84 appears to support the idea that Y-90 oxides are being created on a time scale consistent with the half-life of Y-90 and binding to the beta window. This would result in a measured dose greater than anticipated. In addition, all of the EBT-XD disks had dark points spread throughout the exposed area. This non-uniformity could be indicative

of Y-90 precipitates or localized concentrations on the beta window. Currently, the possibility that the Y-90 metal oxides bound to the polyester beta window seems the most likely explanation for the unexpected increase in the dose measured with the radiochromic film.

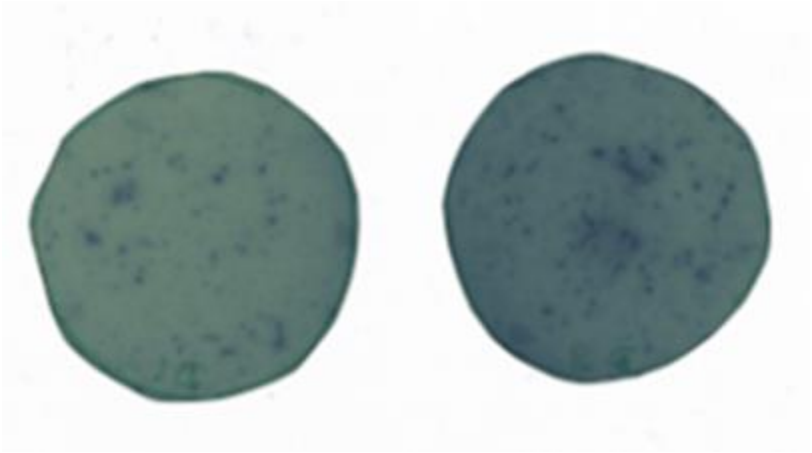

Figure 83: Film disks D1 and D3. Dark spots are present across the entire area of the film. This indicates the presence of localized spots of high activity on the beta window.

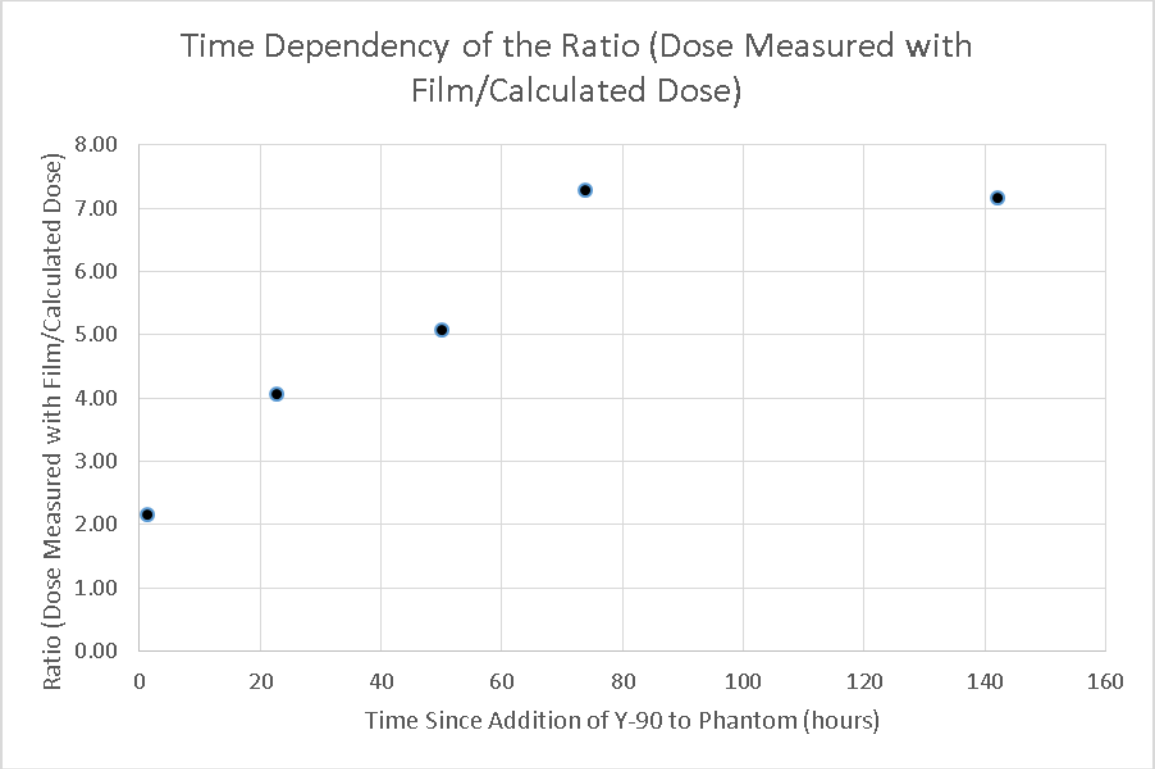

Figure 84: The ratio of dose measured with film to the calculated dose is plotted as a function of the time that elapsed since the Y-90 was added to phantom 4.

IV. Conclusions

It has been shown that the goals of this research have been met. A surrogate microsphere radiolabeled with F-18 has been developed that is stable in vivo. The radiolabeling process is straightforward. The F-18 PET images can be used to perform accurate dosimetry. If this is done prior to therapy, an improvement pre-treatment dosimetry can be expected

The development of a positron emitting surrogate microsphere and the means to use it in pre-treatment dosimetry can move treatment planning for Y-90

radioembolization towards a level of accuracy that is expected in other radiation therapy techniques such as brachytherapy and external beam therapy.

V. Further Work

A. Dual Energy Experiment

The clinical adoption of a surrogate particle will not happen immediately. The ability to perform simultaneous administration of F-18 microspheres and Tc-99m MAA may be worth investigating. Preliminary investigations have found that the relatively low-energy 140 keV gamma photons from the decay of Tc-99m do not affect the PET image. This is expected since the energy window for PET imaging is set much higher than 140 keV.

The question remains as to how much F-18 can be in the gamma camera FOV without perturbing the lung shunt measurements. The current strategy is to make a scatter window that will measure the amount of annihilation photons from F-18 that downscatter into the Tc-99m energy window. This scatter energy window is approximately the same size as the Tc-99m window and is set to a higher energy than the Tc-99m window. For SPECT imaging the default Tc-99m window used is 15%. The lung shunt fraction is a ratio of relative activities measured in the lungs and the liver. In the presence of F-18, it is not entirely clear how the downscatter may affect the counts in the Tc-99m energy window when the ROI are in two different anatomic positions.

B. Modify Beta Dosimetry System

It would be useful to perform the Y-90 dosimetry measurements again. Several options need to be examined prior to repetition of the experiment. These include modification of the phantom to reduce and replace materials likely to bond to Y-90 metal oxides. The addition of a chelator such as EDTA should be considered. Another possibility is to replace the 400 mL of water with an equal volume of 0.04 M HCl acid. This is the same acid concentration used for shipping of the [Y-90] YCl_3. Imaging of the phantom at the several time points could be very useful as well. Imaging can be used to confirm that the activity concentration in the Y-90 solution is remaining homogeneous or not.

C. In Vivo Testing in a Larger Animal

It would be worthwhile to perform in vivo testing in an animal larger than a rat. In this scenario, a catheter would be inserted into the femoral artery for injection of F-18 radiolabeled hydroxyapatite microspheres directly into the liver. This would enable the study of the interaction between macrophages of the liver and the radiolabeled microspheres.

VI. Beyond the Scope of This Work

Clinical trials with human subjects are beyond the scope of this work.

VII. List of References

[1] S. Sezai, S. Sakurabayashi, Y. Yamamoto, and T. Morita, "Hepatic arterial and portal venous oxygen content and extraction in liver cirrhosis," *Liver*, vol. 13, no. 1, pp. 31–35, 1993.

[2] M. Jiang, A. Fischman, and F. S. Nowakowski, "Segmental Perfusion Differences on Paired Tc-99m Macroaggregated Albumin (MAA) Hepatic Perfusion Imaging and Yttrium-90 (Y-90) Bremsstrahlung Imaging Studies in SIR-Sphere Radioembolization: Associations with Angiography," *J. Nucl. Med. Radiat. Ther.*, vol. 03, no. 01, 2012.

[3] L. A. Torre, F. Bray, R. L. Siegel, J. Ferlay, J. Lortet-Tieulent, and A. Jemal, "Global cancer statistics, 2012: Global Cancer Statistics, 2012," *CA. Cancer J. Clin.*, vol. 65, no. 2, pp. 87–108, Mar. 2015.

[4] M. Raval *et al.*, "Yttrium-90 Radioembolization of Hepatic Metastases from Colorectal Cancer," *Front. Oncol.*, vol. 4, Jul. 2014.

[5] W. Shady *et al.*, "Surrogate Imaging Biomarkers of Response of Colorectal Liver Metastases After Salvage Radioembolization Using 90Y-Loaded Resin Microspheres," *Am. J. Roentgenol.*, vol. 207, no. 3, pp. 661–670, Sep. 2016.

[6] M. L. J. Smits *et al.*, "Radioembolization Dosimetry: The Road Ahead," *Cardiovasc. Intervent. Radiol.*, vol. 38, no. 2, pp. 261–269, Apr. 2015.

[7] W.-Y. Lau *et al.*, "Patient Selection and Activity Planning Guide for Selective Internal Radiotherapy With Yttrium-90 Resin Microspheres," *Int. J. Radiat. Oncol.*, vol. 82, no. 1, pp. 401–407, Jan. 2012.

[8] W. A. Dezarn *et al.*, "Recommendations of the American Association of Physicists in Medicine on dosimetry, imaging, and quality assurance procedures for 90Y microsphere brachytherapy in the treatment of hepatic malignancies," *Med. Phys.*, vol. 38, no. 8, pp. 4824–4845, 2011.

[9] M. M. Bé *et al.*, "Table of Radionuclides (vol. 3–A= 3 to 244)," *Monogr. BIPM*, vol. 5, 2006.

[10] R. G. Selwyn, R. J. Nickles, B. R. Thomadsen, L. A. DeWerd, and J. A. Micka, "A new internal pair production branching ratio of 90Y: The development of a non-destructive assay for 90Y and 90Sr," *Appl. Radiat. Isot.*, vol. 65, no. 3, pp. 318–327, Mar. 2007.

[11] S. Gnesin *et al.*, "Partition model based 99mTc-MAA SPECT/CT predictive dosimetry compared to 90Y TOF PET/CT post-treatment dosimetry in

radioembolisation of hepatocellular carcinoma: A quantitative agreement comparison," *J. Nucl. Med.*, Jun. 2016.

[12] T. Carlier *et al.*, "Assessment of acquisition protocols for routine imaging of Y-90 using PET/CT," *EJNMMI Res*, vol. 3, no. 11, 2013.

[13] A. S. Pasciak *et al.*, "Radioembolization and the Dynamic Role of 90Y PET/CT," *Front. Oncol.*, vol. 4, 2014.

[14] M. Krishna, "Microscopic anatomy of the liver," *Clin. Liver Dis.*, vol. 2, no. S1, pp. S4–S7, Mar. 2013.

[15] M. J. Berger, J. S. Coursey, M. A. Zucker, and J. Chang, "ESTAR, PSTAR, and ASTAR: Computer Programs for Calculating Stopping-Power and Range Tables for Electrons, Protons, and Helium Ions (version 1.2.3)." National Institute of Standards and Technology, Gaithersburg, MD, 2005.

[16] "TheraSphere Package Insert USA Rev. 14." BTG International Ltd.

[17] J. O' Doherty, "A review of 3D image-based dosimetry, technical considerations and emerging perspectives in 90Y microsphere therapy," *J. Diagn. Imaging Ther.*, vol. 2, no. 2, pp. 1–34, Apr. 2015.

[18] "SIR-Spheres Package Insert." Sirtex Medical Inc., Feb-2017.

[19] R. G. Selwyn *et al.*, "^{18} F-labeled resin microspheres as surrogates for ^{90} Y resin microspheres used in the treatment of hepatic tumors: a radiolabeling and PET validation study," *Phys. Med. Biol.*, vol. 52, no. 24, pp. 7397–7408, Dec. 2007.

[20] "Technescan MAA Package Insert." Mallinkrodt, Inc., Jan-1997.

[21] O. S. Grosser *et al.*, "Pharmacokinetics of 99mTc-MAA- and 99mTc-HSA-Microspheres Used in Preradioembolization Dosimetry: Influence on the Liver-Lung Shunt," *J. Nucl. Med.*, vol. 57, no. 6, pp. 925–927, Jun. 2016.

[22] R. De Gersem *et al.*, "Influence of time delay on the estimated lung shunt fraction on 99mTc-labeled MAA scintigraphy for 90Y microsphere treatment planning," *Clin. Nucl. Med.*, vol. 38, no. 12, pp. 940–942, 2013.

[23] M. Wondergem *et al.*, "99mTc-Macroaggregated Albumin Poorly Predicts the Intrahepatic Distribution of 90Y Resin Microspheres in Hepatic Radioembolization," *J. Nucl. Med.*, vol. 54, no. 8, pp. 1294–1301, Aug. 2013.

[24] "SIR-Spheres Package Insert." Nov-2014.

[25] Y. H. Kao, E. H. Tan, C. E. Ng, and S. W. Goh, "Clinical implications of the body surface area method versus partition model dosimetry for yttrium-90

radioembolization using resin microspheres: a technical review," *Ann. Nucl. Med.*, vol. 25, no. 7, pp. 455–461, Aug. 2011.

[26] S. Ho *et al.*, "Partition model for estimating radiation doses from yttrium-90 microspheres in treating hepatic tumours," *Eur. J. Nucl. Med.*, vol. 23, no. 8, pp. 947–952, 1996.

[27] A. Kennedy, W. Dezarn, and A. Weiss, "Patient Specific 3D Image-Based Radiation Dose Estimates for 90Y Microsphere Hepatic Radioembolization in Metastatic Tumors," *J. Nucl. Med. Radiat. Ther.*, vol. 01, no. 01, 2011.

[28] Y. K. Dewaraja *et al.*, "MIRD Pamphlet No. 23: Quantitative SPECT for Patient-Specific 3-Dimensional Dosimetry in Internal Radionuclide Therapy," *J. Nucl. Med.*, vol. 53, no. 8, pp. 1310–1325, Aug. 2012.

[29] A. M. Campbell, I. H. Bailey, and M. A. Burton, "Analysis of the distribution of intra-arterial microspheres in human liver following hepatic yttrium-90 microsphere therapy," *Phys. Med. Biol.*, vol. 45, no. 4, p. 1023, 2000.

[30] H. Ilhan *et al.*, "Predictive Value of 99mTc-MAA SPECT for 90Y-Labeled Resin Microsphere Distribution in Radioembolization of Primary and Secondary Hepatic Tumors," *J. Nucl. Med.*, vol. 56, no. 11, pp. 1654–1660, Nov. 2015.

[31] M. L. Smits *et al.*, "Holmium-166 radioembolization for the treatment of patients with liver metastases: design of the phase I HEPAR trial," *J. Exp. Clin. Cancer Res.*, vol. 29, no. 1, p. 1, 2010.

[32] E. Verger *et al.*, "68 Ga and 188 Re Starch-Based Microparticles as Theranostic Tool for the Hepatocellular Carcinoma: Radiolabeling and Preliminary In Vivo Rat Studies," *PloS One*, vol. 11, no. 10, p. e0164626, 2016.

[33] M. Elschot, B. J. Vermolen, M. G. E. H. Lam, B. de Keizer, M. A. A. J. van den Bosch, and H. W. A. M. de Jong, "Quantitative Comparison of PET and Bremsstrahlung SPECT for Imaging the In Vivo Yttrium-90 Microsphere Distribution after Liver Radioembolization," *PLoS ONE*, vol. 8, no. 2, p. e55742, Feb. 2013.

[34] T. Carlier, K. P. Willowson, E. Fourkal, D. L. Bailey, M. Doss, and M. Conti, "90Y -PET imaging: Exploring limitations and accuracy under conditions of low counts and high random fraction," *Med. Phys.*, vol. 42, no. 7, pp. 4295–4309, Jul. 2015.

[35] "LiveChart of Nuclides." International Atomic Energy Agency, Nuclear Data Services.

[36] D. R. Tilley, H. R. Weller, C. M. Cheves, and R. M. Chasteler, "Energy Levels of Light Nuclei A = 18-19," *Nucl. Phys. A*, no. 1, 1995.

[37] J. Cal-González, J. L. Herraiz, S. España, M. Desco, J. J. Vaquero, and J. M. Udías, "Positron range effects in high resolution 3D PET imaging," in *Nuclear Science Symposium Conference Record (NSS/MIC), 2009 IEEE*, 2009, pp. 2788–2791.

[38] K. P. Zhernosekov *et al.*, "Processing of Generator-Produced 68Ga for Medical Application," *J. Nucl. Med.*, vol. 48, no. 10, pp. 1741–1748, Oct. 2007.

[39] B. Sandhöfer *et al.*, "Synthesis and Preliminary *in Vivo* Evaluation of Well-Dispersed Biomimetic Nanocrystalline Apatites Labeled with Positron Emission Tomographic Imaging Agents," *ACS Appl. Mater. Interfaces*, vol. 7, no. 19, pp. 10623–10633, May 2015.

[40] C. R. Chitambar, "Gallium and its competing roles with iron in biological systems," *Biochim. Biophys. Acta BBA - Mol. Cell Res.*, vol. 1863, no. 8, pp. 2044–2053, Aug. 2016.

[41] M. A. Avila-Rodriguez *et al.*, "Positron-emitting resin microspheres as surrogates of 90Y SIR-Spheres: a radiolabeling and stability study," *Nucl. Med. Biol.*, vol. 34, no. 5, pp. 585–590, Jul. 2007.

[42] "Guide to Ion Exchange Catalog Number 140-9997." Bio-Rad Laboratories, Inc., 1997.

[43] S. Kannan, F. Goetz-Neunhoeffer, J. Neubauer, and J. M. F. Ferreira, "Ionic Substitutions in Biphasic Hydroxyapatite and β-Tricalcium Phosphate Mixtures: Structural Analysis by Rietveld Refinement: Ionic Substitutions in Biphasic HAP and β-TCP Mixtures," *J. Am. Ceram. Soc.*, vol. 91, no. 1, pp. 1–12, Dec. 2007.

[44] V. Campana *et al.*, "Bone substitutes in orthopaedic surgery: from basic science to clinical practice," *J. Mater. Sci. Mater. Med.*, vol. 25, no. 10, pp. 2445–2461, Oct. 2014.

[45] X. Fan, "Adsorption kinetics of fluoride on low cost materials," *Water Res.*, vol. 37, no. 20, pp. 4929–4937, Dec. 2003.

[46] "CHT™ Ceramic Hydroxyapatite Instruction Manual, LIT611 Rev E." Bio-Rad Laboratories, Inc.

[47] S. Torquato, T. M. Truskett, and P. G. Debenedetti, "Is random close packing of spheres well defined?," *Phys. Rev. Lett.*, vol. 84, no. 10, p. 2064, 2000.

[48] V. Sternitzke, R. Kaegi, J.-N. Audinot, E. Lewin, J. G. Hering, and C. A. Johnson, "Uptake of Fluoride from Aqueous Solution on Nano-Sized Hydroxyapatite: Examination of a Fluoridated Surface Layer," *Environ. Sci. Technol.*, vol. 46, no. 2, pp. 802–809, Jan. 2012.

[49] N. H. de Leeuw, "Resisting the onset of hydroxyapatite dissolution through the incorporation of fluoride," *J. Phys. Chem. B*, vol. 108, no. 6, pp. 1809–1811, 2004.

[50] M. Jauregui-Osoro *et al.*, "Biocompatible inorganic nanoparticles for [18F]-fluoride binding with applications in PET imaging," *Dalton Trans.*, vol. 40, no. 23, p. 6226, 2011.

[51] J. A. Champion, A. Walker, and S. Mitragotri, "Role of Particle Size in Phagocytosis of Polymeric Microspheres," *Pharm. Res.*, vol. 25, no. 8, pp. 1815–1821, Aug. 2008.

[52] T. Das, S. Chakraborty, H. D. Sarma, M. Venkatesh, and S. Banerjee, "^{166} Ho-Labeled Hydroxyapatite Particles: A Possible Agent for Liver Cancer Therapy," *Cancer Biother. Radiopharm.*, vol. 24, no. 1, pp. 7–14, Feb. 2009.

[53] "Highlights of Prescribing Information Sodium Fluoride F 18 Injection." Siemens Molecular Imaging PETNET Solutions Inc.

[54] "Bulletin_5667 CHT Ceramic Hydroxyapatite Product Information Sheet." Bio-Rad Laboratories, Inc.

[55] "ACR PET Phantom Instructions." American College of Radiology, 23-Jun-2016.

[56] A. S. Pasciak, A. C. Bourgeois, and Y. C. Bradley, "A Comparison of Techniques for 90Y PET/CT Image-Based Dosimetry Following Radioembolization with Resin Microspheres," *Front. Oncol.*, vol. 4, May 2014.

[57] W. E. Bolch, L. G. Bouchet, J. S. Robertson, B. W. Wessels, and others, "MIRD pamphlet No, 17: The dosimetry of nonuniform activity distributions–radionuclide S values at the voxel level," *J. Nucl. Med.*, vol. 40, no. 1, p. S11, 1999.

[58] S. Jan *et al.*, "GATE: a simulation toolkit for PET and SPECT," *Phys. Med. Biol.*, vol. 49, no. 19, pp. 4543–4561, Oct. 2004.

[59] "OpenGATE Collaboration." [Online]. Available: www.opengatecollaboration.org. [Accessed: 01-Apr-2018].

[60] P. Seroul and D. Sarrut, "VV: a viewr for the evaluation of 4D image registration." Jul-2008.

[61] D. J. Simpkin and T. R. Mackie, "EGS4 Monte Carlo determination of the beta dose kernel in water," *Med. Phys.*, vol. 17, no. 2, pp. 179–186, 1990.

[62] L. Maigne, Y. Perrot, D. R. Schaart, D. Donnarieix, and V. Breton, "Comparison of GATE/GEANT4 with EGSnrc and MCNP for electron dose calculations at energies between 15 keV and 20 MeV," *Phys. Med. Biol.*, vol. 56, no. 3, pp. 811–827, Feb. 2011.

[63] H. Uusijärvi, N. Chouin, P. Bernhardt, L. Ferrer, M. Bardies, and E. Forssell-Aronsson, "Comparison of electron dose-point kernels in water generated by the

Monte Carlo codes, PENELOPE, GEANT4, MCNPX, and ETRAN," *Cancer Biother. Radiopharm.*, vol. 24, no. 4, pp. 461–467, 2009.

[64] P. Papadimitroulas, G. Loudos, G. C. Nikiforidis, and G. C. Kagadis, "A dose point kernel database using GATE Monte Carlo simulation toolkit for nuclear medicine applications: Comparison with other Monte Carlo codes," *Med. Phys.*, vol. 39, no. 8, pp. 5238–5247, 2012.

[65] F. Botta *et al.*, "Calculation of electron and isotopes dose point kernels with FLUKA Monte Carlo code for dosimetry in nuclear medicine therapy: FLUKA Monte Carlo code for nuclear medicine dosimetry," *Med. Phys.*, vol. 38, no. 7, pp. 3944–3954, Jun. 2011.

[66] S. Seltzer, "Electron-photon Monte Carlo calculations: The ETRAN code," *Int. J. Radiat. Appl.*, vol. 42, no. 10, pp. 917–941, 1991.

[67] "ICRU Report 56, Dosimetry of External Beta Rays for Radiation Protection." International Commission on Radiation Units and Measurements, 1997.

[68] "ESTAR Stopping Power and Range Tables for Electrons." National Institute of Standards and Technology, Gaithersburg, MD.

[69] I. J. Chetty *et al.*, "Reporting and analyzing statistical uncertainties in Monte Carlo?based treatment planning," *Int. J. Radiat. Oncol.*, vol. 65, no. 4, pp. 1249–1259, Jul. 2006.

[70] S. Jan *et al.*, "GATE V6: a major enhancement of the GATE simulation platform enabling modelling of CT and radiotherapy," *Phys. Med. Biol.*, vol. 56, no. 4, pp. 881–901, Feb. 2011.

[71] B. R. B. Walters, I. Kawrakow, and D. W. O. Rogers, "History by history statistical estimators in the BEAM code system," *Med. Phys.*, vol. 29, no. 12, pp. 2745–2752, Nov. 2002.

[72] K. F. Eckerman, R. Westfall, J. C. Ryman, and M. Cristy, "Availability of Nuclear Decay Data in Electronic Form, Including Beta Spectra Not Previously Published," *Health Phys.*, vol. 67, no. 4, pp. 338–345, 1994.

[73] M. Soret, S. L. Bacharach, and I. Buvat, "Partial-Volume Effect in PET Tumor Imaging," *J. Nucl. Med.*, vol. 48, no. 6, pp. 932–945, Jun. 2007.

[74] "Efficient Protocols for Calibration and Dosimetry.pdf." Ashland inc.

[75] D. Lewis and M. F. Chan, "Correcting lateral response artifacts from flatbed scanners for radiochromic film dosimetry," *Med. Phys.*, vol. 42, no. 1, pp. 416–429, 2015.

[76] C. G. Soares *et al.*, "Dosimetry of beta-ray ophthalmic applicators: Comparison of different measurement methods," *Med. Phys.*, vol. 28, no. 7, pp. 1373–1384, Jul. 2001.

[77] R. P. Kollaard *et al.*, "Recommendations on detectors and quality control procedures for brachytherapy beta sources," *Radiother. Oncol.*, vol. 78, no. 2, pp. 223–229, Feb. 2006.

[78] J. C. Gust, R. M. Graham, and M. A. Lombardi, *Stopwatch and timer calibrations*. US Department of Commerce, Technology Administration, National Institute of Standards and Technology, 2009.

[79] D. Lewis, A. Micke, X. Yu, and M. F. Chan, "An efficient protocol for radiochromic film dosimetry combining calibration and measurement in a single scan," *Med. Phys.*, vol. 39, no. 10, pp. 6339–6350, 2012.

[80] "EBTXD_Specifications_Final.pdf." Ashland inc.

[81] A. Micke, D. F. Lewis, and X. Yu, "Multichannel film dosimetry with nonuniformity correction," *Med. Phys.*, vol. 38, no. 5, pp. 2523–2534, 2011.

[82] J. A. Siegel, B. E. Zimmerman, K. Kodimer, M. A. Dell, and W. E. Simon, "Accurate Dose Calibrator Activity Measurement of 90Y-Ibritumomab Tiuxetan," p. 6.

[83] M.-A. Park, A. Mahmood, R. E. Zimmerman, N. Limpa-Amara, G. M. Makrigiorgos, and S. C. Moore, "Adsorption of metallic radionuclides on plastic phantom walls: Adsorption of metallic radionuclides on plastic," *Med. Phys.*, vol. 35, no. 4, pp. 1606–1610, Mar. 2008.

VIII. Appendices

Appendix A

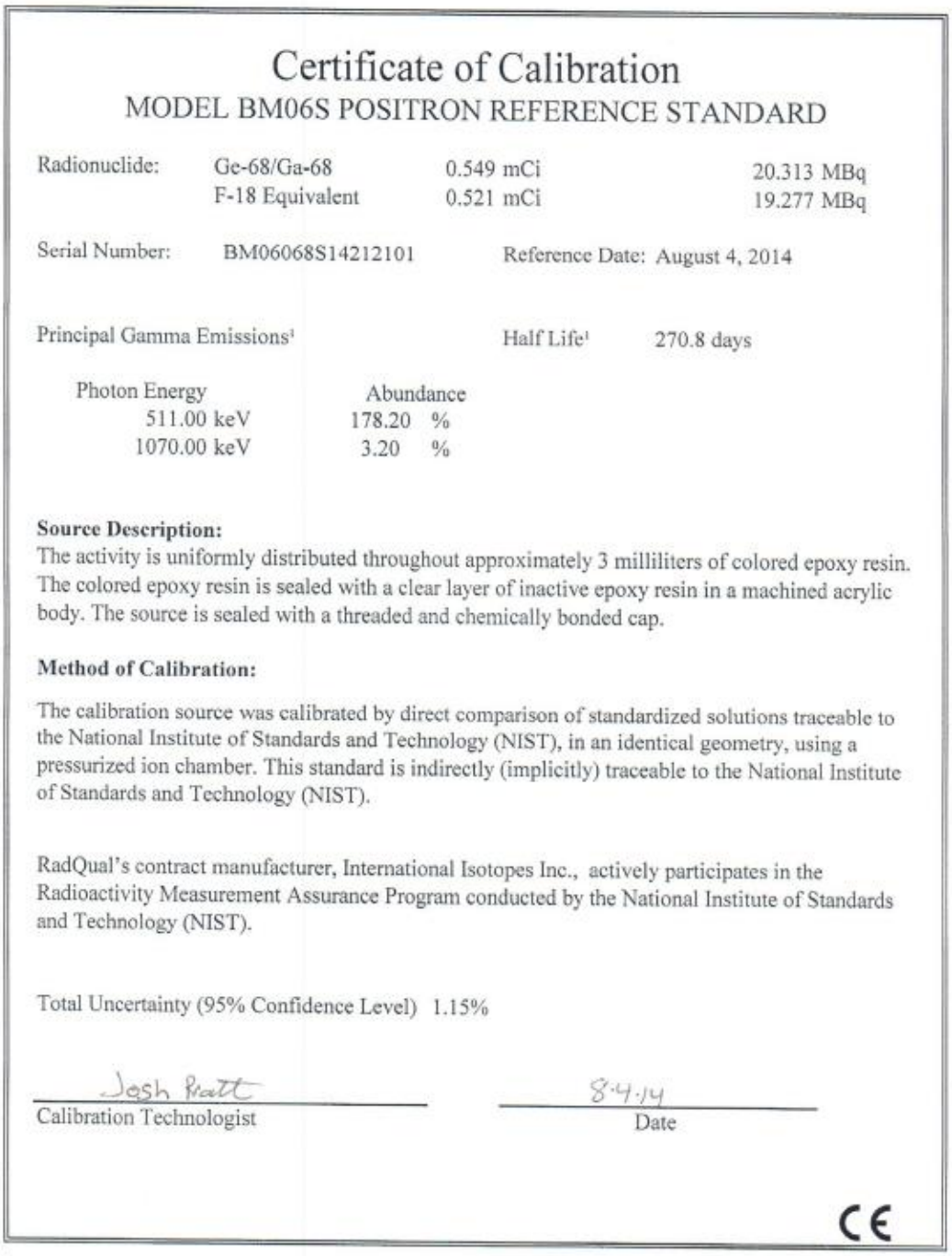

Certificate of Calibration

MODEL BM06S POSITRON REFERENCE STANDARD

Radionuclide:	Ge-68/Ga-68	0.549 mCi	20.313 MBq
	F-18 Equivalent	0.521 mCi	19.277 MBq

Serial Number: BM06068S14212101 Reference Date: August 4, 2014

Principal Gamma Emissions[1] Half Life[1] 270.8 days

Photon Energy	Abundance
511.00 keV	178.20 %
1070.00 keV	3.20 %

Source Description:
The activity is uniformly distributed throughout approximately 3 milliliters of colored epoxy resin. The colored epoxy resin is sealed with a clear layer of inactive epoxy resin in a machined acrylic body. The source is sealed with a threaded and chemically bonded cap.

Method of Calibration:

The calibration source was calibrated by direct comparison of standardized solutions traceable to the National Institute of Standards and Technology (NIST), in an identical geometry, using a pressurized ion chamber. This standard is indirectly (implicitly) traceable to the National Institute of Standards and Technology (NIST).

RadQual's contract manufacturer, International Isotopes Inc., actively participates in the Radioactivity Measurement Assurance Program conducted by the National Institute of Standards and Technology (NIST).

Total Uncertainty (95% Confidence Level) 1.15%

Josh Pratt
Calibration Technologist

8.4.14
Date

CE

[1] Table of Isotopes, Eighth Edition 1996
RadQual, LLC * 114 Barrington Town Square #124* Aurora, Ohio 44202 * (603) 513-1221 * (603) 415-0160 Fax

RadQual™

HOW TO USE YOUR NEW Ge-68/Ga-68 DOSE CALIBRATOR STANDARD

NOTE: Your new standard provides you with the first **direct** NIST traceable standard for dose calibrators, for positron emitting isotopes. The standard uses Ge-68/Ga-68 as the nuclide in secular equilibrium and decays using the Ge-68 half-life of 270.8 days. The F-18 cross calibration value is provided by NIST and is only applicable in the syringe position and to the physical properties of this standard.

1. Insert the standard in the "syringe" position in your dose calibrator
2. If equipped - push your preset button for Ga-68
3. Adjust your ion chamber setting according to the operations manual until the readout on the dose calibrator matches the value stated on the certificate for Ge-68/Ga-68 (ensure you adjust for decay if any) value as indicated on the enclosed decay calendar for today's date.
4. Your dose calibrator is now calibrated for Ga-68
5. If equipped – push your button for F-18
6. Adjust your ion chamber setting according to the operations manual until the readout on the dose calibrator matches the value stated on the certificate for F-18 (ensure you adjust for decay if any, decay is based on the Ge-68) or the value as indicated on the enclosed decay calendar.

Regulatory & Manufacturing· P.O. Box 82 • Weare NH 03281 • Phone: 603.513.1221· Fax: 603.415.0160
info@radqual.com ·www.radqual.com

RadQual™

Decay Reference Calender for Ge-68/Ga-68 (F-18 cross referenced)
Dual Geometry Source

Source Serial No. **BM06068S14212101**

Source Reference Date **4-Aug-14**

Labeled Activity **0.549** mCi
20.31 MBq

Date	Ge-68/Ga-68 mCi	Ge-68/Ga-68 MBq	F-18 mCi	F-18 MBq
4-Aug-14	0.549	20.31	0.521	19.27
5-Aug-14	0.548	20.26	0.520	19.22
6-Aug-14	0.546	20.21	0.518	19.17
7-Aug-14	0.545	20.16	0.517	19.12
8-Aug-14	0.543	20.11	0.516	19.08
9-Aug-14	0.542	20.05	0.514	19.03
10-Aug-14	0.541	20.00	0.513	18.98
11-Aug-14	0.539	19.95	0.512	18.93
12-Aug-14	0.538	19.90	0.510	18.88
13-Aug-14	0.537	19.85	0.509	18.83
14-Aug-14	0.535	19.80	0.508	18.79
15-Aug-14	0.534	19.75	0.506	18.74
16-Aug-14	0.532	19.70	0.505	18.69
17-Aug-14	0.531	19.65	0.504	18.64
18-Aug-14	0.530	19.60	0.503	18.59
19-Aug-14	0.528	19.55	0.501	18.55
20-Aug-14	0.527	19.50	0.500	18.50
21-Aug-14	0.526	19.45	0.499	18.45
22-Aug-14	0.524	19.40	0.497	18.40
23-Aug-14	0.523	19.35	0.496	18.36
24-Aug-14	0.522	19.30	0.495	18.31
25-Aug-14	0.520	19.25	0.494	18.26
26-Aug-14	0.519	19.20	0.492	18.22
27-Aug-14	0.518	19.15	0.491	18.17
28-Aug-14	0.516	19.10	0.490	18.12
29-Aug-14	0.515	19.05	0.489	18.08
30-Aug-14	0.514	19.01	0.487	18.03
31-Aug-14	0.512	18.96	0.486	17.99
1-Sep-14	0.511	18.91	0.485	17.94
2-Sep-14	0.510	18.86	0.484	17.89
3-Sep-14	0.508	18.81	0.482	17.85
4-Sep-14	0.507	18.76	0.481	17.80
5-Sep-14	0.506	18.72	0.480	17.76
6-Sep-14	0.505	18.67	0.479	17.71
7-Sep-14	0.503	18.62	0.477	17.67
8-Sep-14	0.502	18.57	0.476	17.62
9-Sep-14	0.501	18.53	0.475	17.58
10-Sep-14	0.499	18.48	0.474	17.53
11-Sep-14	0.498	18.43	0.473	17.49
12-Sep-14	0.497	18.38	0.471	17.44
13-Sep-14	0.496	18.34	0.470	17.40
14-Sep-14	0.494	18.29	0.469	17.35
15-Sep-14	0.493	18.24	0.468	17.31
16-Sep-14	0.492	18.20	0.467	17.26
17-Sep-14	0.491	18.15	0.465	17.22
18-Sep-14	0.489	18.10	0.464	17.18
19-Sep-14	0.488	18.06	0.463	17.13
20-Sep-14	0.487	18.01	0.462	17.09
21-Sep-14	0.486	17.96	0.461	17.04
22-Sep-14	0.484	17.92	0.459	17.00
23-Sep-14	0.483	17.87	0.458	16.96
24-Sep-14	0.482	17.83	0.457	16.91
25-Sep-14	0.481	17.78	0.456	16.87
26-Sep-14	0.479	17.74	0.455	16.83
27-Sep-14	0.478	17.69	0.454	16.78
28-Sep-14	0.477	17.65	0.452	16.74
29-Sep-14	0.476	17.60	0.451	16.70
30-Sep-14	0.474	17.56	0.450	16.66
1-Oct-14	0.473	17.51	0.449	16.61
2-Oct-14	0.472	17.47	0.448	16.57
3-Oct-14	0.471	17.42	0.447	16.53
4-Oct-14	0.470	17.38	0.446	16.49
5-Oct-14	0.468	17.33	0.444	16.44
6-Oct-14	0.467	17.29	0.443	16.40
7-Oct-14	0.466	17.24	0.442	16.36
8-Oct-14	0.465	17.20	0.441	16.32
9-Oct-14	0.464	17.16	0.440	16.28
10-Oct-14	0.462	17.11	0.439	16.24
11-Oct-14	0.461	17.07	0.438	16.19
12-Oct-14	0.460	17.03	0.437	16.15
13-Oct-14	0.459	16.98	0.435	16.11
14-Oct-14	0.458	16.94	0.434	16.07
15-Oct-14	0.457	16.89	0.433	16.03
16-Oct-14	0.456	16.85	0.432	15.99
17-Oct-14	0.454	16.81	0.431	15.95
18-Oct-14	0.453	16.77	0.430	15.91
19-Oct-14	0.452	16.72	0.429	15.87
20-Oct-14	0.451	16.68	0.428	15.83
21-Oct-14	0.450	16.64	0.427	15.78
22-Oct-14	0.449	16.59	0.426	15.74
23-Oct-14	0.447	16.55	0.424	15.70
24-Oct-14	0.446	16.51	0.423	15.66
25-Oct-14	0.445	16.47	0.422	15.62
26-Oct-14	0.444	16.43	0.421	15.58
27-Oct-14	0.443	16.38	0.420	15.54
28-Oct-14	0.442	16.34	0.419	15.50
29-Oct-14	0.441	16.30	0.418	15.47
30-Oct-14	0.439	16.26	0.417	15.43
31-Oct-14	0.438	16.22	0.416	15.39
1-Nov-14	0.437	16.18	0.415	15.35
2-Nov-14	0.436	16.13	0.414	15.31
3-Nov-14	0.435	16.09	0.413	15.27
4-Nov-14	0.434	16.05	0.412	15.23
5-Nov-14	0.433	16.01	0.411	15.19
6-Nov-14	0.432	15.97	0.410	15.15
7-Nov-14	0.431	15.93	0.408	15.11
8-Nov-14	0.429	15.89	0.407	15.07
9-Nov-14	0.428	15.86	0.406	15.04
10-Nov-14	0.427	15.81	0.405	15.00
11-Nov-14	0.426	15.77	0.404	14.96
12-Nov-14	0.425	15.73	0.403	14.92
13-Nov-14	0.424	15.69	0.402	14.88
14-Nov-14	0.423	15.65	0.401	14.84
15-Nov-14	0.422	15.61	0.400	14.81
16-Nov-14	0.421	15.57	0.399	14.77
17-Nov-14	0.420	15.53	0.398	14.73
18-Nov-14	0.419	15.49	0.397	14.69
19-Nov-14	0.417	15.45	0.396	14.66
20-Nov-14	0.416	15.41	0.395	14.62
21-Nov-14	0.415	15.37	0.394	14.58
22-Nov-14	0.414	15.33	0.393	14.54
23-Nov-14	0.413	15.29	0.392	14.51
24-Nov-14	0.412	15.25	0.391	14.47
25-Nov-14	0.411	15.21	0.390	14.43
26-Nov-14	0.410	15.17	0.389	14.40
27-Nov-14	0.409	15.13	0.388	14.36
28-Nov-14	0.408	15.10	0.387	14.32
29-Nov-14	0.407	15.06	0.386	14.29
30-Nov-14	0.406	15.02	0.385	14.25
1-Dec-14	0.405	14.98	0.384	14.21
2-Dec-14	0.404	14.94	0.383	14.18
3-Dec-14	0.403	14.90	0.382	14.14
4-Dec-14	0.402	14.87	0.381	14.10
5-Dec-14	0.401	14.83	0.380	14.07

Appendix B

MEDICAL RADIATION RESEARCH CENTER
1300 UNIVERSITY AVENUE 1530 MSC MADISON, WI 53706
TEL: 608.262.6320 FAX: 608.262.5012 uwmrrc.wisc.edu

University of Wisconsin
Accredited Dosimetry Calibration Laboratory

Certificate of Calibration

Accredited® Dosimetry Calibration Laboratory

ACCREDITED
Certificate No: 1664.01

The enclosed calibration reports are traceable to the National Institute of Standards and Technology (NIST), and accredited by the American Association of Physicists in Medicine (AAPM) and the American Association of Laboratory Accreditation (A2LA) to ISO/IEC 17025-1999 and ANSI/NCSL Z540-1-1994 standards.

Accredited Dosimetry Calibration Laboratory

UNIVERSITY OF WISCONSIN
ACCREDITED DOSIMETRY CALIBRATION LABORATORY
1300 University Avenue, Room 1530, Madison, Wisconsin 53706-1532
Phone: (608) 262-6320 Fax: (608) 262-5012

Report of Calibration

for

Sr-90 Ophthalmic Applicator

Submitted by:	Rafael Acosta, D.Sc. South Texas Cancer Center-McAllen 1901 S. 2nd St. McAllen TX 78503
Ophthalmic Applicator:	Amersham International Model SIA.20 Serial Number 0547ML

Date Received: 22/JAN/08 Calibration Completed: 5/FEB/08

This calibration is directly traceable to the National Institute of Standards and Technology (NIST), is compliant with ISO/IEC 17025-1999 and ANSI/NNCSL Z540-1-1994, and is accredited by the AAPM and the American Association of Laboratory Accreditation. The expanded uncertainty of measurement as stated in the data page of this report is the standard uncertainty of measurement multiplied by the coverage factor k=2, which for a normal distribution corresponds to a coverage probability of approximately 95%. This report shall not be reproduced except in full, without the written permission of the UW RCL.

Form Revised 31/MAR/97

University of Wisconsin - Madison
Department of Medical Physics
Accredited Dosimetry Calibration Laboratory

Sr-90 Ophthalmic Applicator Measurement Data

Calibration Date: February 5, 2008 Report Date: February 8, 2008

Submitted Sr-90 Source

Manufacturer: Amersham International
Model: SIA.20
Serial Number: 0547ML

Surface Geometry : Plane
Stated Activity : 55 mCi
Stated Date : 18/SEP/85
Decayed Activity : 32.1 mCi

Instruments used in Calibration

NIST Calibrated Transfer Standard:
Manufacturer: Tracerlab
Model: RA1
Serial Number: 541

International Specialty Products
Model HD-810 GaF Chromic Film
Molecular Dynamics Model PD-DI Laser Scanner
#251-1/4 White Diffusion Filter
NIH Image v1.60 Image Analysis Software

MEASUREMENT CONDITIONS

Temperature: 20.8°C
Calibration Classification: IV
Backscatter Material: RMI Solid Water Plate
Exposure Durations: 5, 8, 11, 14, 17 minutes
Source Orientation: Serial number on source stem OUT (toward the bottom of the film image)
Calibration Uncertainty: +/-11%

MEASUREMENT RESULTS

FWHM Active Source Diameter:	**8.1 mm**
Average Surface Absorbed Dose Rate to Water:	**0.39 Gy/sec**
Maximum Surface Absorbed Dose Rate to Water:	**0.41 Gy/sec**

Comments: The reported Average Surface Absorbed Dose Rate to Water refers to the central 4 mm region of the source relative to the reference standard source. The reported Maximum Surface Absorbed Dose Rate to Water is the maximum value over the entire area of the source (source outer diameter = 12.0 mm). All dose rate decay calculations were determined using a half-life of 28.78 yr (NNDC, Brookhaven). A surface contour plot and orthogonal dose rate profile curves are attached following this page. Please refer to the Appendix for a description of reported calibration factors.

Recorded in data book: UW ADCL SR-02 Pages: 240-241

Calibrated by: John A. Micka, B.S.
Physicist, Accredited Dosimetry
Calibration Laboratory

Reviewed by: Larry A. DeWerd, Ph.D.
Member,
UW-ADCL Advisory Committee

University of Wisconsin - Madison
Department of Medical Physics
Accredited Dosimetry Calibration Laboratory

Absorbed Dose Contour Plot for Amersham Model SIA.20 s/n 0547ML
(percent of Maximum Dose)

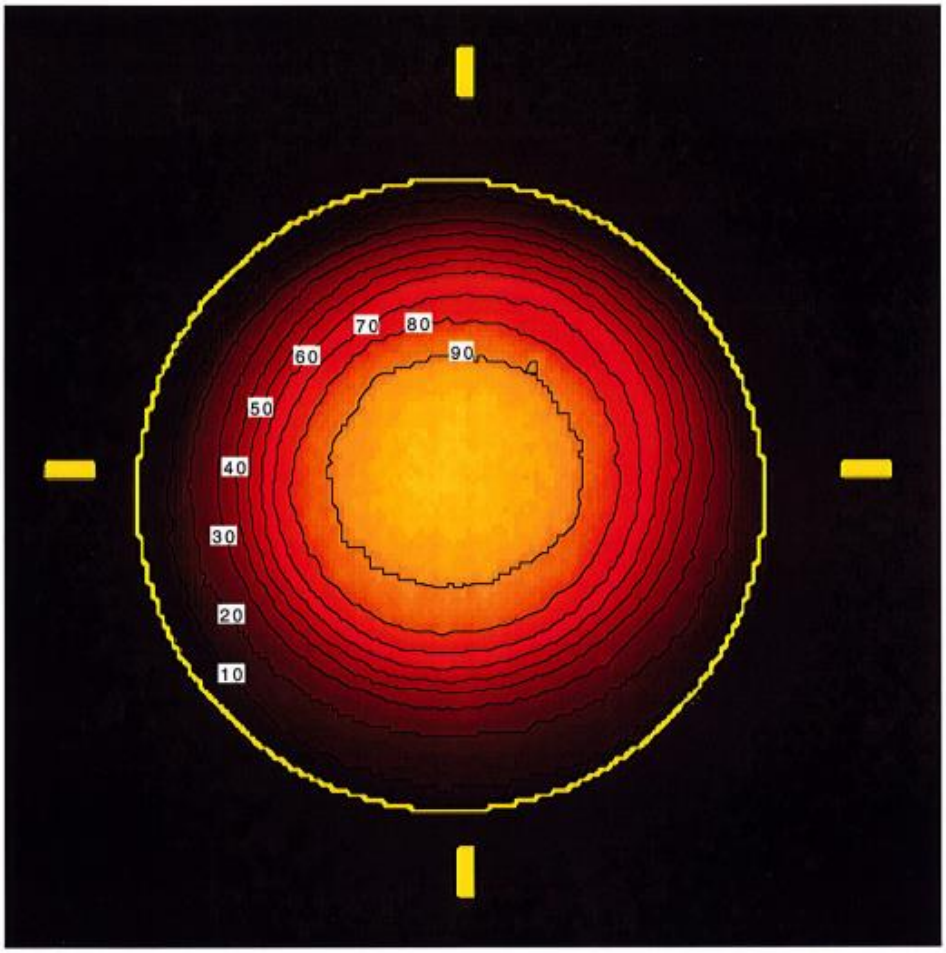

The yellow hashmarks on the image correspond to the horizontal and vertical (top-down) dose rate profiles as displayed on page 4 of this report. The bottom yellow hashmark corresponds to the reference location of the source (serial number toward bottom of image). The yellow circle corresponds to the outer physical diameter of the source. The inside edge of each hashmark is equidistant to the radiation center of the source.

University of Wisconsin - Madison
Department of Medical Physics
Accredited Dosimetry Calibration Laboratory

Absorbed Dose Rate to Water Profiles, Amersham Model SIA.20 s/n 0547ML
(The zero position in each profile corresponds to the radiation center of the source)

Horizontal Profile

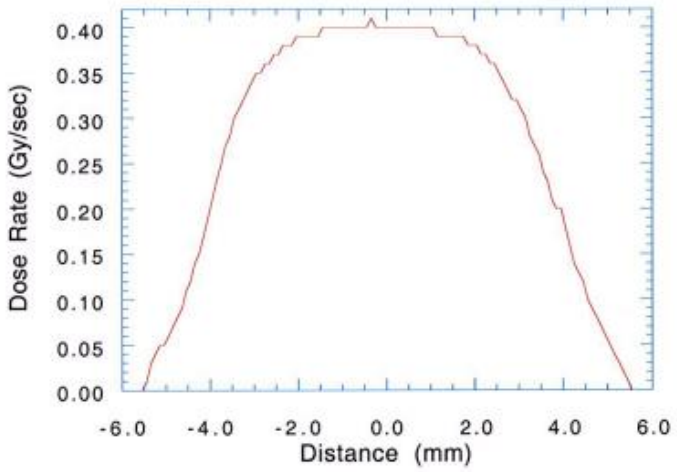

Vertical Profile

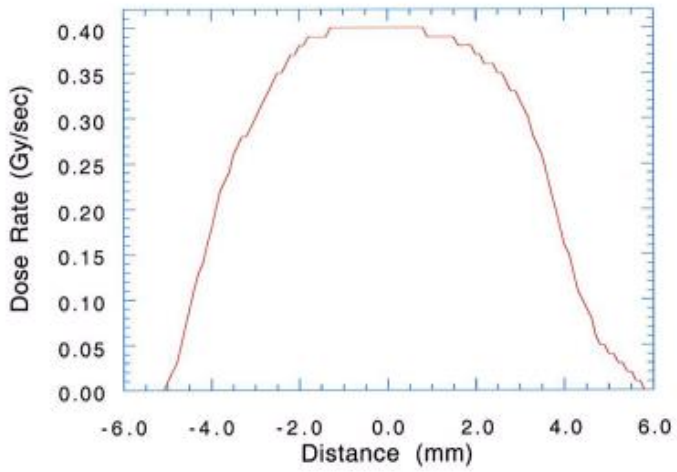

APPENDIX 5

DESCRIPTION OF REPORTED UW-ADCL CALIBRATION RESULTS FOR Sr-90/Y-90 OPHTHALMIC APPLICATORS

University of Wisconsin – Madison
Medical Radiation Research Center
Accredited Dosimetry Calibration Laboratory

Proper application and use of the radiation therapy device described in this document is dependent upon correct use by trained medical personnel. Therefore, the duration of responsibility of the University of Wisconsin, Medical Radiation Research Center, Accredited Dosimetry Calibration Laboratory and its employees for the calibration extends only to the time the device leaves the premises of the University of Wisconsin. It is recommended that the device user establish an appropriate protocol for monitoring the source output before and after its submission to the University of Wisconsin and on a regular basis thereafter. In addition, it is the express responsibility of the device user to assure (by personal communication if necessary), that interpretation of the information in this document is consistent with the interpretation intended by the Accredited Dosimetry Calibration Laboratory.

Important Notice

Effective January 1, 2003, the National Institute of Standards and Technology (NIST) has revised the primary surface absorbed dose to water rate standard for Sr-90 ophthalmic applicators. The net effect of this change is an increase in the surface dose rate of approximately 5.3% with respect to values reported prior to 2003. This change was implemented at the UW-ADCL on October 1, 2003. In addition, the reported calibration uncertainty was also reduced by NIST, which is now reflected in the UW-ADCL reported uncertainty. Please contact us for further clarification if necessary.

This calibration is based upon a transfer of absorbed dose to water from a NIST calibrated source to the source of this report using model HD810 radiochromic film (International Specialty Products, Wayne, NJ). The **Full Width-Half Maximum (FWHM) Active Source Diameter** in mm is the average diameter of the source where the dose is 50% of the maximum value over the entire source active area. The **Average Surface Absorbed Dose Rate** reported by this laboratory is the dose rate in water averaged over the central 4 mm region of the source. The **Maximum Surface Absorbed Dose Rate** is the maximum dose rate (in water) over the entire active area of the source. All measurements of absorbed dose to water are at the bare surface of the source (all masks removed) and have units of Gy/sec. The FWHM Active Source Diameter measurement is performed by setting the threshold on the film images at the 50% level and determining the average diameter at this level. The Horizontal and Vertical Absorbed Dose Rate profiles are obtained using 1.5 mm lines in each direction through the center of the image. The Contour Plot is obtained by normalizing the calibrated two-dimensional dose distribution to 100%. Contour lines from 10 to 90 in 10% increments are selected and printed on page 3 of the report.